CONTROLLING THE DYNAMICS OF ELECTRONS AND NUCLEI IN ULTRAFAST STRONG LASER FIELDS

by

NORA G. KLING

B.A., Augustana College, USA, 2005
M.S., Kansas State University, USA, 2010

AN ABSTRACT OF A DISSERTATION

submitted in partial fulfillment of the
requirements for the degree

DOCTOR OF PHILOSOPHY

Department of Physics
College of Arts and Sciences

KANSAS STATE UNIVERSITY
Manhattan, Kansas
2013

Abstract

One ultimate goal of ultrafast, strong-field laser science is to coherently control chemical reactions. Present laser technology allows for the production of intense ($>10^{13}\,\mathrm{W/cm^2}$), ultrashort ($\leq 5\,\mathrm{fs}$), carrier-envelope phase-stabilized pulses. By knowing the electric field waveform, sub-cycle resolution on the order of 100's of attoseconds ($1\,\mathrm{as} = 10^{-18}\,\mathrm{s}$) can be reached — the timescale for electron motion. Meanwhile, the laser field strengths are comparable to that which binds electrons to atoms or molecules. In this intense-field ultrashort-pulse regime one can both measure and manipulate dynamics of strong-field, quantum-mechanical processes in atoms and molecules.

Despite much progress in the technology, typical durations for which lasers can be reliably locked to a specific carrier-envelope phase ranges from a few minutes to a few hours. Experiments investigating carrier-envelope phase effects that have necessarily long data acquisition times, such as those requiring coincidence between fragments originating from the same atom or molecule, are thus challenging and uncommon. Therefore, we combined the new technology for measuring the carrier-envelope phase of each and every laser shot with other single-shot coincidence three-dimensional momentum imaging techniques to alleviate the need for carrier-envelope phase stabilized laser pulses.

Using phase-tagged coincidence techniques, several targets and laser-induced processes were studied. One particular highlight uses this method to study the recollision process of non-sequential double ionization of argon. By measuring the momentum of the two electrons emitted in the process, we could study their energy sharing. Furthermore, by selecting certain carrier-envelope phase values, and therefore laser pulses with a particular waveform, events with single recollision could be isolated and further analyzed. Another highlight is our studies of carrier-envelope phase effects in the dissociation of the benchmark

H_2^+ ion beam. Aided by near-exact quantum mechanical calculations, we could identify interfering pathways which lead to the observed spatial asymmetry. These and other similar experiments are described in this thesis as significant steps toward their ultimate control.

CONTROLLING THE DYNAMICS OF ELECTRONS AND NUCLEI IN ULTRAFAST STRONG LASER FIELDS

by

NORA G. KLING

B.A., Augustana College, USA, 2005
M.S., Kansas State University, USA, 2010

A DISSERTATION

submitted in partial fulfillment of the
requirements for the degree

DOCTOR OF PHILOSOPHY

Department of Physics
College of Arts and Sciences

KANSAS STATE UNIVERSITY
Manhattan, Kansas
2013

Approved by:

Major Professor
Itzik Ben-Itzhak

Copyright

Abstract

One ultimate goal of ultrafast, strong-field laser science is to coherently control chemical reactions. Present laser technology allows for the production of intense ($>10^{13}\,\mathrm{W/cm^2}$), ultrashort ($\leq 5\,\mathrm{fs}$), carrier-envelope phase-stabilized pulses. By knowing the electric field waveform, sub-cycle resolution on the order of 100's of attoseconds ($1\,\mathrm{as} = 10^{-18}\,\mathrm{s}$) can be reached — the timescale for electron motion. Meanwhile, the laser field strengths are comparable to that which binds electrons to atoms or molecules. In this intense-field ultrashort-pulse regime one can both measure and manipulate dynamics of strong-field, quantum-mechanical processes in atoms and molecules.

Despite much progress in the technology, typical durations for which lasers can be reliably locked to a specific carrier-envelope phase ranges from a few minutes to a few hours. Experiments investigating carrier-envelope phase effects that have necessarily long data acquisition times, such as those requiring coincidence between fragments originating from the same atom or molecule, are thus challenging and uncommon. Therefore, we combined the new technology for measuring the carrier-envelope phase of each and every laser shot with other single-shot coincidence three-dimensional momentum imaging techniques to alleviate the need for carrier-envelope phase stabilized laser pulses.

Using phase-tagged coincidence techniques, several targets and laser-induced processes were studied. One particular highlight uses this method to study the recollision process of non-sequential double ionization of argon. By measuring the momentum of the two electrons emitted in the process, we could study their energy sharing. Furthermore, by selecting certain carrier-envelope phase values, and therefore laser pulses with a particular waveform, events with single recollision could be isolated and further analyzed. Another highlight is our studies of carrier-envelope phase effects in the dissociation of the benchmark

H_2^+ ion beam. Aided by near-exact quantum mechanical calculations, we could identify interfering pathways which lead to the observed spatial asymmetry. These and other similar experiments are described in this thesis as significant steps toward their ultimate control.

Table of Contents

List of Figures

List of Tables

Acknowledgments

They say it takes a village to raise a child. I think the same must be true for a graduate student. I have many people to thank for their support, help, encouragement, and patience that, after many years of education, made it possible for me to earn a Ph.D. Itzik Ben-Itzhak taught me to be thorough, skeptical, optimistic, and how to think about experimental design. Kevin Carnes helped to see projects through the twists and turns that were unaccounted for from the beginning, and perhaps indirectly I learned much about coding and data analysis from him. Brett Esry has held the level of physics to a high standard, which I greatly appreciate, including in the classroom, through the weekly joint experiment and theory meeting, and working on projects together. My knowledge and understanding of AMO physics has benefited from these experiences.

Itzik's prolific group has also given me inspiration, motivation, and merriment. Working with wonderfully knowledgable post-docs such as Penquian Wang, Jarlath McKenna, and Kelsie Betsch, who really loved their work in the lab, made it an enjoyable place to be. Their dedication to the experiments and the long nights in the lab taught me the perseverance needed to succeed. I also got to work with Zhenhua Wang in JRM, in the last year and a half. We measured a phase potato with the KLS beam with about 5.5 fs duration with a window that was rotating the polarization (it was made out of sapphire). I will never forget the moment we saw that potato, after so much frustration. Thanks for struggling through that with me Zhenhua — that is one of my favorite things in the lab: when things start working and we understand why.

Much inspiration, motivation, and merriment in Itzik's group would not have been without the many excellent graduate students. Learning with you and in many cases, from you, has been a blessing. So a substantial piece of my gratitude is for A. Max Sayler, Bishwanath Gaire, Mohammad Zohrabi, Utuq Ablikim, Ben Berry, Bethany Jochim, and Travis Severt.

It is so great to remember what it was like being an undergraduate as a graduate student,

and to feed off of the constant source of positive energy that undergraduates seem to radiate. Thus I appreciate the REU and KSU undergrads whom I worked with, namely Mat Leonard, Eli Parke, Adam Summers, and Anya Gura.

Of course if I spent all my time in the lab, I would never learn any "real physics." Through our weekly joint meeting with Brett Esry's theory group, I have, slowly but surely, come to understand many concepts of strong field physics. It was these discussions where experimentalist and theorist had to communicate with each other, and therefore helped me learn how to discuss physics. And so I am grateful to the theory participants Christian Madsen, Shuo Zeng, Fatima Anis, Janjun Hua, and Brandon Rigsbee.

As about 2.5 years of my PhD was spent at MPQ, I am lucky to have been surrounded by kind and smart people who accepted me into their group including Boris Bergues, Matthias Kübel, Oliver Herrwerth, Sergey Zherebtsov, Frederik Süßmann, Sarah Stebbings, Irina Znakovskaya, Adrian Wirth, Simon Watson, Waldemar Schneider, Lauryna Lötscher, Johannes Stierle, Ferenc Krausz, and, probably most importantly, Ms. Monika Wild.

Through collaborations, including my stay in Germany, I also had the great pleasure of having many mentors, including Eric Wells, Matthias Lezius, Artem Rudenko, Lew Cocke, Matthias Kling, Ali Alnaser, Gerhard Paulus, Bob Jones and Wania Wolff.

I like to share my gratitude for the support staff at KSU: Peggy Matthews, Jane Peterson, Lindsay Thompson, Deanna Selby, Mike Wells, Al Rankin, Calvin Hodges, Scott Chainey, Kim Elliot, Brian Merritt, Vince Needham, Russ Reynolds. And at MPQ: Harald Haas, Anton Horn, Tobias Kleinhenz, Alois Böswald, Karl Bauer. For the community of KSU physics: Adrian Madsen, Dipanwita Ray, Irina Bocharova, Sankar De, Predrag Ranitovic, Amy Rouinfar, Fran Mateycik, Jackie Chini, Mike Chini, Dyan Jones, Varun Makhija, Xioaming Ren, Neda Dadashzadeh, Maia Magrakvelidze, Sean McBride and the other "village" members of Cardwell Hall.

Of course, I am also thankful for my wonderful, loving, and supportive family: Lawrence, Diane, Toby, Holly, Logan, Makenna, Alex, Susan, Kevin, Michael, Lily, Cassie, Sean,

Declan and Owen. And my "German" family Wolgang, Ursula, Carsten, Linus. And same for my dearest friends: Stacia, Bethany, and Kelli.

Then there is one person who has shared my ups and downs, my happiness and my frustration, and has encouraged me through it all, sometimes from 5000 miles away, my wonderful, amazing husband, Matthias Kling.

Special thanks goes to the Fulbright commission for supporting my studies and the first 10 months of my stay in Germany. During this time I grew as a person, as well as a physicist. And special thanks also goes to the DOE support which made it possible for my participation in the 62nd Lindau Nobel Laureates Meeting. This was truly a special event, where I met people who have changed and who currently are changing the face of science.

Funding agencies which supported my research are the Chemical Sciences, Geosciences, and Biosciences Division, Office of Basic Energy Sciences of the Department of Energy, the National Science Foundation Grant No. CHE-0822646, and the Max Planck Society.

Dedication

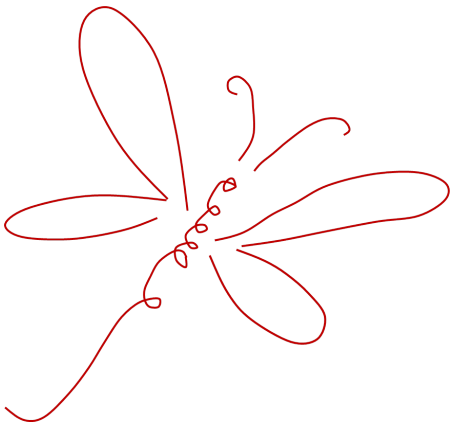

Chapter 1

Introduction

1.1 Background and Motivations

In the second half of the 19th century, an incoherent source of light, the commercially available light bulb, was invented by Thomas Edison [1]. Nearly a century later, in the 1960s, a coherent light source was demonstrated by Theodore H. Maiman, namely the ruby laser [2]. Several lasing media have been discovered since then. The first light-wave manipulation of the translational motion of atoms was demonstrated in 1985 by Chu *et al.* [3, 4] who confined and cooled sodium atoms. In fact, Chu *et al.*'s work was made possible with mode-locking technology, from 2 decades prior to their work [5]. This mode-locking technology played a crucial step in the development of the Ti:Sapphire laser [3]. In the 1980s Ti:Sapphire based laser systems with 100's of femtoseconds[1] pulse durations were realized, and chirped-pulse amplification (CPA) technology allowed for increasing laser power output [6]. The high laser power confined to such short timescales, when focused in space, produced "strong" fields comparable to the fields which bind electrons to atoms[2] or molecules. Such lasers are thus capable of removing electrons from atoms or molecules.

In the last decades, it was found that electron motion can be coherently controlled through interactions with laser pulses (see Refs. [7, 8], and references therein), leaving

[1] A femtosecond is 10^{-15} s.

[2] At an intensity of 3.51×10^{16} W/cm^2, the field strength is equal to the field binding a $1s$ electron in the first Bohr orbit of the hydrogen atom.

physicists with several questions, such as: what are the mechanisms behind the control, and to what degree can electron (and nuclear) motion be controlled? These questions have stimulated experimentalists and theorists to strive for understanding laser-matter interaction on a fundamental level. By building a framework of understanding for the basic processes that occur on atomic and molecular scales and for the underlying mechanisms, the extension to larger systems becomes natural. Therefore, applications of strong laser fields are relevant to the areas of medicine, energy, defense systems, etc. [9–16].

1.2 Laser Matter Interactions

Intense, ultrafast laser-matter interactions have led to the discovery of several physical phenomena (see, for example, Refs. [8, 17, 18], and references therein). Three regimes of strong-field processes have emerged: multiphoton [19–21], tunneling [22–24], and over-the-barrier [25, 26]. The classification depends on the ratio of the energies of a bound electron and of a free electron in the oscillating electric field of the laser [27]. In 1965 Keldysh introduced a parameter, γ, to describe which regime is most important for a given set of parameters [28]. The Keldysh parameter is commonly defined as $\gamma = \sqrt{I_p/2\,U_p}$, where I_p is the ionization potential of the target, and $U_p = E^2/4\,\omega^2$ is the ponderomotive potential in atomic units [29]. Here E is the electric field strength of the laser, and ω is the carrier angular frequency. To be in the multiphoton regime $\gamma \gg 1$, and the laser field is only slightly distorting the potential as shown schematically in Fig. 1.1(a). To be in the tunneling regime, $\gamma \leq 1$. In the tunneling regime, the laser field causes the potential to bend over significantly such that a barrier is formed, as shown in Fig. 1.1(b). When $\gamma \ll 1$, the potential is suppressed enough that electrons can "escape" over-the-barrier, as shown in Fig. 1.1(c).

In order to have a clear picture of the processes, simple systems, such as atoms or small molecules, are studied, such that many competing processes do not hamper their interpretation. A brief summary of select processes, relevant to strong field laser interactions with atoms or molecules and this thesis, is given in the remainder of this Section.

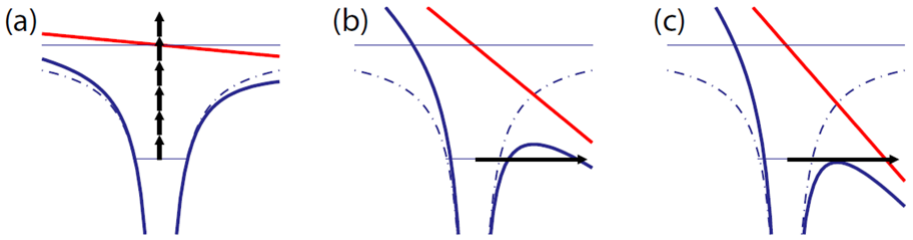

Figure 1.1: Schematic of the three strong-field regimes: (a) multiphoton, (b) tunneling, and (c) over-the-barrier. The Coulomb potential without a laser field present is shown as purple dashed-dotted lines, and the potentials with a laser field (red solid line) present are shown as purple solid lines. Adapted from Ref. [30].

1.2.1 Recollision

The process by which electron recollision occurs was introduced by Corkum [31, 32] and Kulander [33]. Electron recollision is summarized in three steps, as illustrated in Fig. 1.2. First, an electron tunnels through the barrier created by the combined potential of the atom (or molecule) and the laser field. Next, the electron oscillates with the laser field. The oscillating laser field is defined as $E(t) = E_0(t)\cos(\omega t + \phi)$, where $E_0(t)$ is an envelope function and ϕ is the carrier-envelope phase (CEP). For some laser-driven electron trajectories, the electron recollides with its parent ion. Upon collision, several things can happen, depending on the energy of the returning electron, including the following:

HHG — The electron can recombine with its parent ion and emit a photon with frequencies related to harmonics of the original laser light [35]. This is called high harmonic generation (HHG), which has been observed for atoms and molecules.

HATI — If the electron is elastically scattered, high-order above threshold ionization (HATI), where more photons than necessary to ionize the target are absorbed, can occur [36, 37]. The signature of ATI is several peaks, separated by the photon energy, in a photoelectron spectrum [38].

NSDI — If the electron is inelastically scattered off the parent ion, further ionization can occur via a process called nonsequential double ionization (NSDI) [18, 39]. This process

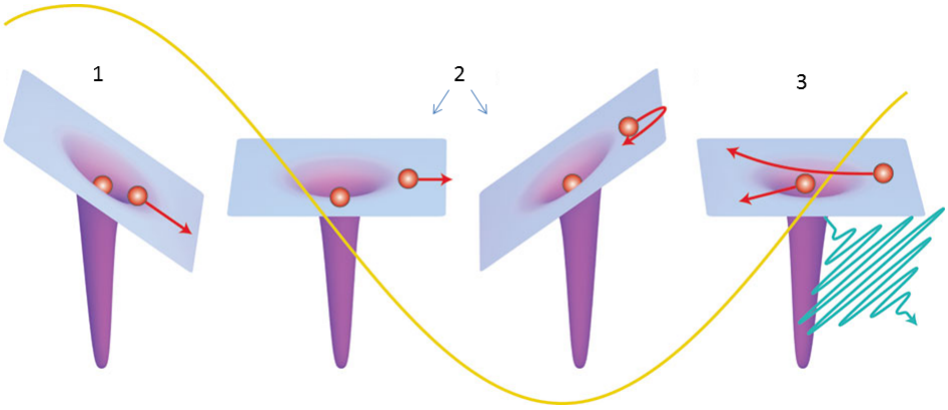

Figure 1.2: Cartoon of the three-step model for recollision (see text). Adapted from [34].

manifests as an enhancement in the double to single ionization yield ratio, as the intensity is scanned from high to low, producing a "knee" in such a spectrum [40, 41]. The two electrons removed in the NSDI process have been shown to be correlated [42–44].

RCE — Another possibility if the electron scatters in-elastically, is to excite the parent ion upon recollision, called recollision excitation (RCE) [45, 46]. This process played a particularly important role in the interpretation of the first observation of CEP control of dissociating D_2^+ molecules from D_2 [45].

1.3 H_2^+

Molecules are inherently more complex than atoms, due to the wide range of time and energy scales due to the vibrational and rotational degrees of freedom. The simplest neutral molecule, H_2, is already beyond the scope of near-exact theoretical calculations due to the difficulty in treating both electrons. Therefore, the simplest molecule, H_2^+, which can be described fairly accurately by theory, serves as a prototype for studying molecular processes in a strong laser field (see, for example, Refs. [47–50]). The dressed potential, or Floquet picture, shown for H_2^+ in Fig. 1.3, is one of the most intuitive pictures for describing the phenomena. For a detailed description of Floquet formalism, see Refs. [47, 51, 52]. The

prevalent dissociation processes occurring for H_2^+ are outlined here.

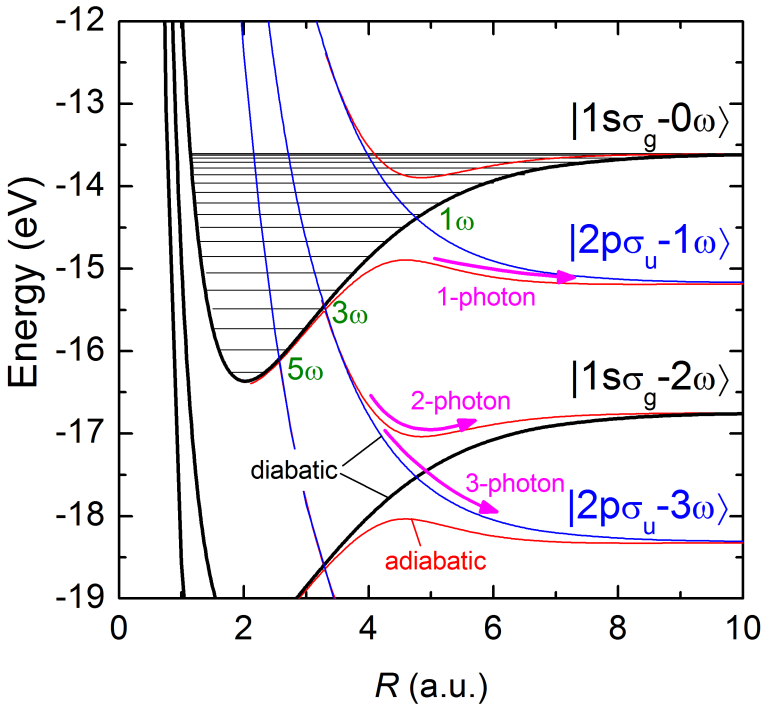

Figure 1.3: Floquet picture for H_2^+ with 790 nm photons. Adapted from [53].

BS — Bond softening (BS) occurs by the net absorption of a single photon. The pathway for BS, labeled 1-photon, is shown in Fig. 1.3. At the diabatic crossing of the curves labeled $|1s\sigma_g - 0\omega\rangle$ and $|2p\sigma_u - 1\omega\rangle$, a molecule can transition from the $1s\sigma_g$ to the $2p\sigma_u$ state, following the dipole selection rules, and dissociate. For the adiabatic curves, a gap opens up depending on the laser field strength, "softening" the molecular bond [54, 55].

ATD — Above threshold dissociation (ATD) is analogous to ATI. The number of photons absorbed exceeds that needed to dissociate [55–57]. In H_2^+, the absorption of two photons already falls under this category. Both the 2-photon and 3-photon ATD pathways are marked in Fig. 1.3, ending on $|1s\sigma_g - 2\omega\rangle$ and $|2p\sigma_u - 3\omega\rangle$, respectively.

ZPD — Zero-photon dissociation (ZPD) is at least a two-photon process [58, 59]. Exactly like in Raman scattering, a photon is absorbed from the laser field, and another photon is emitted through stimulated emission [60]. To gain the needed energy for dissociation, the

second photon has a longer wavelength, within the laser bandwidth, leading to a zero net gain of photons. The signature of ZPD for H_2^+ is a kinetic energy release near 0 eV [58, 59].

Ionization phenomena of H_2^+ in a strong laser field include Coulomb explosion and enhanced ionization. In Coulomb explosion, the H_2^+ is ionized at or close to its equilibrium internuclear distance, leaving behind two protons, which repel each other [61–63]. Coulomb explosion leads to a high kinetic energy release. Enhanced ionization requires that the internuclear distance between the two protons of the H_2^+ molecule expands first, reaching a point where it becomes more favorable for ionization [64, 65]. Thus, enhanced ionization leads to a lower kinetic energy release.

The understanding gained through studying H_2^+ has been successfully applied to multielectron molecules. Hatten *et al.* have observed ATD of CO^{2+} [66], Natan *et al.* have used chirped pulses to manipulate bond softening [67], and current work shows signatures of ZPD in CS^{2+} [68]. More phenomena — that cannot occur in H_2^+ — have been observed in multi-electron molecules. For instance, charge asymmetric dissociation (CAD), where molecules dissociate with unequal charge states of the fragments, has been observed for many molecules [66, 69–80]. Another example is the migration of protons in hydrocarbons [81, 82]. These studies of more complex systems require modeling, as (near-) exact theory is impractical. Yet, with the intuition gained over the years of studying the most basic systems, modeling of even complex targets can reach satisfactory insight into the physical processes.

1.4 Theoretical Approaches

When possible, solutions of the time-dependent Schrödinger equation (TDSE) are the most desirable for obtaining accurate representations of physical observables. The TDSE, even for H_2^+ is usually accompanied by some approximations, such as the Born-Oppenheimer approximation, where the nuclear and electronic degrees of freedom are separated [83]. In addition, the H_2^+ is often treated as an aligned, non-rotating molecule [84–88]. Care must

be taken when interpreting the results of such calculations, as artifacts can arise due to the reduced dimensionality. This is the case for the so-called vibrational trapping, which disappears when rotation and vibration are included in the calculations [89, 90].

Models help further our understanding when the problem is too complex for solving the TDSE. The models tend to be more case specific and therefore cannot be applied universally. An example is the single active electron (SAE) approximation, which assumes that only one electron strongly interacts with the laser field at a time [91]. The SAE thus works best for atoms with a single valence electron, such as the alkali series or certain negative ions. For the nobel gases, further constraints are needed for the model to apply, namely the photon energy is smaller than the binding energy of an electron, where sequential processes tend to dominate [91]. An obvious case for which the SAE is not a good model is the NSDI process. Here two electrons are removed whose dynamics depend on each other. Such a process necessarily goes beyond the SAE approximation, as the interaction of the electrons must be considered, commonly referred to as correlated electron dynamics.

1.4.1 Non-sequential double ionization

The first observation of electron-electron correlation in NSDI was in 1983 by L'Huillier *et al.* [40]. Since then theories to explain the NSDI phenomenon have been developed, ranging from purely classical to quantum mechanical in nature. A full quantum mechanical TDSE description is currently very challenging. However, qualitatively, the essence of the physics can be captured even with the classical description. Eberly and co-workers have focused on following ensembles of classical electron trajectories to study the NSDI process [92, 93]. They found that for certain trajectories the recollision occurs when the laser field goes through zero, and the second ionization occurs just before the next field maximum. From their analysis, they determined that the electrons will travel out from the atom in the same hemisphere if the final ionization occurs before the laser field peaks. In contrast, the electrons were more likely to travel out from the atom in opposite hemispheres when the second

electron ionizes after the laser field peaks [93]. Classical calculations by Emmanouilidou and Staudte [94] have allowed for several classifications of NSDI mechanisms, including simultaneous ejection, also known as (e,2e), where a second electron is directly ionized upon recollision, and recollision induced excitation with subsequent field ionization (RESI), where a second electron is field ionized sometime after the recollision occurs. Furthermore, recent classical calculations by Uzer and co-workers have shown general trends for the conditions necessary to have NSDI with circularly polarized laser fields for NO targets [95].

Lin and co-workers developed the quantitative rescattering theory (QRS) in order to describe rescattering phenomena in strong fields. Briefly, QRS expresses the yields for HHG, high-order ATI, or NSDI as the product of a returning electron wavepacket with the relevant field-free electron-ion scattering cross section. For instance, HHG uses the photo-recombination cross section, while NSDI uses the electron-impact ionization cross section [96]. Recently they applied QRS to model the electron correlations of NSDI of argon and neon [97]. For argon, the calculations reproduced the experimental Ar^{2+} recoil ion momentum well, however, the calculated correlations in momenta of the two electrons failed to resemble that of a similar experiment [97–99].

Using the strong field approximation (SFA), Faria and co-workers [18, 100–102] have also investigated NSDI. The SFA is a quantum mechanical, nonperturbative analytical method which assumes that the initial bound state of the atom or molecule is unaffected by the laser field and that the continuum final state does not feel the binding potential [103]. Their calculations agree with recent experimental results for argon, including the behavior in sub-5 fs laser pulses, where the correlated electron momenta change dramatically with the CEP [100]. In fact, many theoretical approaches have been developed to describe CEP effects in atomic and molecular processes.

1.4.2 Carrier-Envelope Phase Effects

Atoms

Carrier-envelope phase effects have been observed in atomic processes such as ATI [37, 104], NSDI [98, 99], and angular streaking of electrons [105]. Understanding the origin of CEP effects has been largely facilitated by theory. For ATI in hydrogen atoms, for instance, solving the TDSE in three dimensions yields highly accurate results which can be quantitatively compared to experimental data [106]. Going beyond the simplest atom, to more complex, multi-electron atoms is a big leap for theory. For example, hydrogen-like atoms, such as the alkali series can still be treated with TDSE [107], but then the SAE approximation must be invoked in order to reduce the problem to a single electron response to the strong field.

Theoretical models have also proven to provide insight, although more limited, into CEP effects. Kling *et al.* used SFA and TDSE to describe CEP effects in nobel gases [104]. For the SFA calculations, the long-range Coulomb interaction between the ionized electron and the ion left behind was neglected. The TDSE calculations were carried out within the SAE approximation. The applicability of these methods to atoms with a full valence shell with light at 800 nm wavelengths can be questioned. Nevertheless for both models, the phase shift could be reproduced for the high energy portion of the spectra, which is where the models were expected to have the best agreement. Abel *et al.* experimentally explored the low energy ATI of xenon, and used the multiphoton model based on interference between indistinguishable quantum paths proposed by Esry and co-workers [108] to decipher the CEP effects seen there. They also explored the effects caused by a small chirp of the broadband laser pulses [109]. Quantitative rescattering theory has been shown to agree well with TDSE calculations, but has the advantage of consuming far less computer time [36]. For example, QRS theory has also been successful in computing the high-order ATI energy spectrum of Xenon [36].

Molecules

Carrier-envelope phase effects in molecular processes offers an exciting prospect to control reaction pathways. The prototype for a simple dissociation reaction is breaking the H_2^+ bond. Given only one electron and no ionization, the hydrogen molecular ion (and its isotopologues) can be solved, nearly exactly, using the TDSE [89, 110, 111].

Studying the same dissociation process, but starting from laser populated H_2^+ targets, already complicates matters due to the intrinsic coherence imprinted on the wavefunctions of the H_2^+ and the need to treat ionization. The theoretical description of the H_2^+ formation relies heavily on models. However, the remaining interaction between the H_2^+ and laser is often carried out using TDSE [50, 86–88]. Semi-classical approaches have also been undertaken [50, 112–114]. In both cases, an initial Franck-Condon vibrational wavepacket created by the ionization of H_2 within the laser pulse was assumed. This "initial" H_2^+ population has been questioned by Urbain *et al.* [115]. Despite these theoretical complications, studies on H_2 targets are more accessible and therefore not only were the first molecules for CEP effects to be observed [45], but they continue to be an experimental work-horse [88].

Carrier-envelope phase effects in multi-electron molecules beyond hydrogen have also been investigated. Some notable examples are the dissociative ionization of CO [116–118], and the fragmentation of small hydrocarbons [119, 120]. Quantum-chemical-based model calculations were used to investigate the origins of the CEP effects observed for the C^+ fragments from the laser-induced dissociative single ionization of CO in Ref. [116]. Three possible contributions to the observed spatial asymmetry were discussed, including (i) the ionization step, (ii) the recollision step , and (iii) laser-induced population transfer between excited electronic states during the dissociation step. The theoretical results suggested that both the dynamics of the ionization and dissociation step played a role. Since then, Liu *et al.* [117] and Betsch *et al.* [118] have studied higher ionization channels, further exploring the possible contributions of recollision and ionization to the observed spatial asymmetries, but without theoretical support. One-dimensional semiclassical calculations were used to

simulate the CEP effects in the dissociative ionization of acetylene in Ref. [119]. The authors suggest that the main mechanism contributing to the observed spatial asymmetry is due to recollision. While each of these works provides some grounds for understanding specific cases of CEP effects in molecular dynamics, none have tried to develop a general theory. A general theory does exist however. It was developed by Esry and co-workers and explains any CEP effect in terms of pathway interference [108]. This theory has been invoked to describe several CEP phenomena, including, CEP effects in the photoelectron emission of Xe [109], the dissociative ionization of H_2 [121, 122], and recently, in the dissociation of H_2^+ [110, 111].

1.5 Document Organization

The goal of this body of work was to gain understanding of electron and nuclear dynamics induced by laser interactions with atoms and molecules. Exploitation of $\leq$5 fs pulses has led to experiments where the CEP of the laser pulse plays an important role. It was also demonstrated for several atomic and molecular targets that coherent control is possible. The experiments, data, and interpretations to reach this goal are organized in the following way:

Most of the experimental methods used throughout the thesis appear in Chapter 2. As the work described in this thesis was conducted in several laboratories, including JRML at Kansas State University, MPQ, and LMU in Germany, there are many experimental approaches that were used. A summary of the associated electronics used is given in Appendix A, the software processing of the recorded raw data is presented in Appendix B, and the design of the phase meter is discussed in Appendix C.

In Chapter 3, the laser induced molecular dissociation imaging (LIMDI) method was employed to measure laser-induced breakup channels of CO^+. In particular, the charge asymmetric dissociation channel, $C^{2+} + O$, was studied with pulse durations ranging from 7 to 40 fs and intensities in the low-mid 10^{15} W/cm^2. Nuclear dynamics for the formation of

this channel could be inferred from the pulse duration dependence.

With the advent of sub-5 fs pulses, the importance of the CEP of the laser pulses becomes relevant. Previous CEP studies have relied on the stabilization of the CEP of the laser. In Chapter 4, an alternative approach to studying CEP dependent processes is presented, namely "phase tagging." Here the CEP for each and every laser pulse is measured in a single-shot stereo-ATI phase meter [123]. The application of phase tagging to COLTRIMS measurements is used to study correlated electron motion for NSDI of several targets, including argon, N_2, and NO, in Chapter 5. Dissociative ionization of CO and C_2H_2 targets was also studied using the phase-tagged COLTRIMS method and is also discussed in Chapter 5.

In Chapter 6, the development of the phase-tagged LIMDI method is described and utilized for novel experiments on a beam of H_2^+. Theory by Esry and co-workers predicted CEP effects in the dissociation of the simplest molecule nearly a decade ago [85]. In fact, in 2006, our group made several attempts to measure such CEP effects on H_2^+ ion beam targets with CEP-stabilized laser pulses. Due to the extremely high demands of the experiment: the need of an extremely short laser pulse (at the time only 7 fs was possible), long-term stabilization of the CEP (the longest locked duration was typically less than an hour), and the low density of the ion beam, the early experiments never produced any meaningful results. The combination of having access to a higher repetition rate laser, achieving shorter pulses, and phase-tagging opposed to phase-locking has provided the necessary ingredients for successful experiments. This work is described in Chapter 6.

Single-shot VMI provides the means to carry out the phase-tagging concept with higher particle detection rates, when coincidence is not important. However, the "standard" VMI design by Eppink and Parker [124] is limited in the highest electron energies, to about 100 eV. A VMI was designed with a "thick" electrostatic lens to extend the energy up to 1 keV. This design is discussed in Chapter 7. Finally, a summary of the topics covered and the future directions of the projects are given in Chapter 8.

Chapter 2

Experimental Methods Used

A summary of the experimental three-dimensional momentum imaging methods used in this dissertation are given in this Chapter. As detailed descriptions of much of the equipment and analysis procedures can be found elsewhere [52, 58, 125], only the main points are emphasized in Sections 2.1 and 2.2. The phase-tagging and thick-lens velocity map imaging (VMI) methods were developed in order to reach the technological advancement necessary to investigate certain physical processes of interest in this dissertation, and are therefore detailed in their own Chapters (4 and 7, respectively). The lasers used for the various experiments discussed in this dissertation are summarized in Section 2.3 of this Chapter.

2.1 COLTRIMS

Cold target recoil ion momentum spectroscopy (COLTRIMS), also known as reaction microscopy (REMI), is a coincident three-dimensional (3D) momentum imaging technique [126–128]. The capability of measuring ions and electrons originating from a single target atom or molecule in coincidence makes COLTRIMS a powerful technique for studying topics such as correlated electron dynamics (see Chapter 5). The limitation of such a coincidence technique is that count rates must be kept to below one per laser shot, such that false coincidences do not hamper the real coincidences. For conventional COLTRIMS studies, this requires a thin target and extremely good vacuum conditions in the apparatus. High repetition rate lasers (several kHz, or even higher) are therefore highly desired for COLTRIMS

measurements to keep data acquisition times within a reasonable time frame.

The COLTRIMS setup is shown schematically in Fig. 2.1. The main components are the ultra-high vacuum (UHV) chamber, the supersonic gas jet target, the spectrometer, the laser optics, the coils for producing a magnetic field, and the ion and electron detectors. Two COLTRIMS apparatuses were used in this dissertation. One was located at the Max Planck Institute for Quantum Optics (MPQ), which was moved to the Ludwig Maximilian University (LMU), and the other COLTRIMS is located in the James R. Macdonald (JRM) lab at Kansas State University (KSU). The description here is for the JRM COLTRIMS[1], and the few differences for the MPQ-LMU COLTRIMS are summarized towards the end of this Section.

Ultra-high vacuum is crucial for COLTRIMS experiments, as the overall rate of ions and electrons must be kept to well below one per laser shot. Therefore, ions and electrons generated from the background gas in the chamber effectively reduce the rate of fragments from the target that could otherwise be achieved. A base pressure on the order of 10^{-11} Torr is reached by having several turbo-molecular pumps and a getter pump attached to the apparatus and by baking for several days.

The gas is introduced into the vacuum chamber through a small nozzle, with 30 μm diameter, where the gas expands. A skimmer with a 0.5 mm diameter selects the atoms or molecules that have velocity in the direction of the interaction region, therefore reducing the transverse velocity components — as depicted in Fig. 2.1. A one dimensional piezo-controlled slit, perpendicular to the spectrometer axis, is used to limit the size of the target (adjustable from 45 μm to 2 mm) to help ensure detection rates are optimal (see Section 3.5.1.2 in Ref. [125] for details). High momentum resolution requires that the gas target is cold. Using high enough backing pressure on the gas regulator, supersonic conditions, and therefore a cold target, can be met. The jet exits the vacuum chamber through the catcher. The catcher has a small hole with about 1 cm diameter to reduce back streaming.

[1]This COLTRIMS is described in depth in Ref. [125].

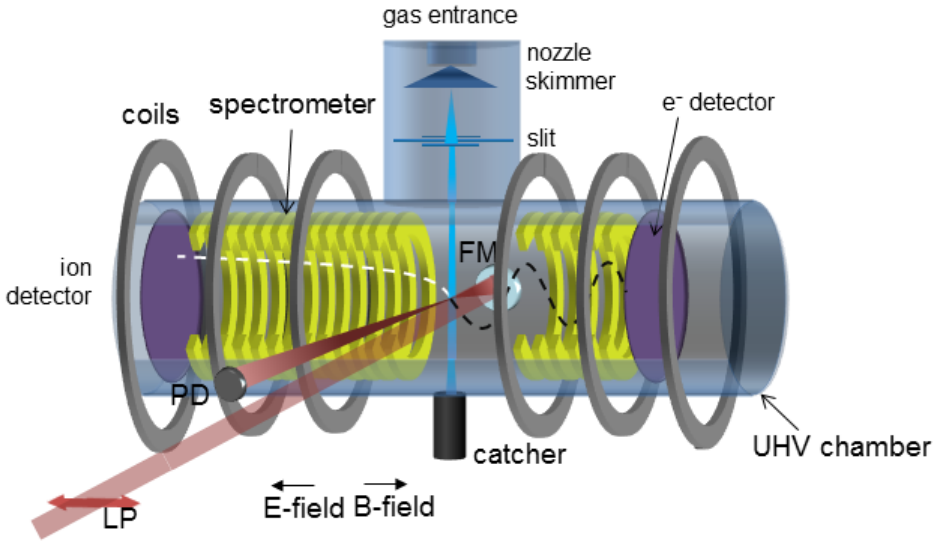

Figure 2.1: Schematic for the COLTRIMS apparatus housed within an ultra high vacuum (UHV) chamber. The thin supersonic jet enters the interaction region from the top, after going though one skimmer and piezo-controlled slits, and is expelled from the system through the catcher. An electrostatic field is provided by voltage on the spectrometer which directs ions toward the ion detector and electrons to the electron detector. Note that the rings are equally spaced throughout, and that a few rings have artificially been removed to show the laser path. Current driven through the coils around the chamber generates a magnetic field along the spectrometer axis. Typically the laser polarization (LP) is linear, and is along the spectrometer axis. The laser is back-focused by a 7.5 cm focusing mirror (FM) and the divergent light after the focus is used to initiate a photodiode (PD) signal which triggers the readout of the electronics. See text for more details.

The COLTRIMS has a back-focusing geometry, where the collimated laser beam enters the chamber through a 1 mm thick ultraviolet (UV)-grade fused silica window and is reflected off a spherical focusing mirror with f=7.5 cm. The focusing mirror is attached to a 3D-positioning manipulator, allowing alignment of the laser focus onto the gas jet target.

Ions and electrons generated by the laser are directed to their respective detectors by a weak electric field produced by an imaging spectrometer. The spectrometer consists of 8 rings on the electron side and 42 rings on the ion side, all connected by a chain of resistors. At both ends of the spectrometer there is a flat, high-transmission mesh on which voltage is applied. The ions generated in the interaction will feel a force leading to their acceleration,

$F = q\,E = m\,a$, where q is the charge, E is the electric field strength from the spectrometer, m is the mass of the ion, and a is the acceleration. Consequently, particles with different charge and different mass will arrive at the detector separated by their m/q ratio. In fact, the TOF will be proportional to $\sqrt{m/q}$, and the t_0 offset can be extrapolated from a linear fit to a plot of the measured TOF versus the $\sqrt{m/q}$ for a few identifiable ion species (although, this value is better determined by the measured electrons [129]).

The light electrons move much faster than the ions. If the electrons are not already going towards the electron detector, they are easily lost upon collision with the spectrometer rings or the wall of the vacuum chamber. In order to measure the full 4π distribution of electrons, a magnetic field is applied through pairs of coils co-axial with the spectrometer. Now the particles feel a Lorentz force $F = q\,[E + (v \times B)] = m\,a$. This has little bearing on the ions, but the electrons will spiral towards the electron detector, making it possible to collect electrons with all emission angles, up to a certain energy. The configuration of the coils is discussed in more detail in Ref. [125].

The detectors are chevron stacked microchannel plate (MCP) detectors with delay line anodes [130]. Descriptions of how MCPs and delay lines work can be found, for example, in Refs. [52, 125, 129]. Basically, the TOF is derived from the signal decoupled through a resistor-capacitor (RC) circuit from the MCP, while the position is derived from the signal decoupled from the ends of the delay line wires. Example position and TOF spectra are shown in Fig. 2.2(a) and (b) for strong field laser ionization of an argon target. A schematic of the electronic-signal processing is presented in Appendix A. In Appendix B, the concept of our 3D imaging method, which allows for reconstruction of the momentum from the position and TOF, is described.

The MPQ-LMU COLTRIMS was overall very similar to the JRML COLTRIMS. The differences are: (1) there is no piezo slit for trimming the jet, and thus no easily controllable knob for keeping the count rate low besides adjusting the backing pressure of the gas bottle. (2) The base pressure reached in the experiment chamber is on the order of 10^{-10} Torr,

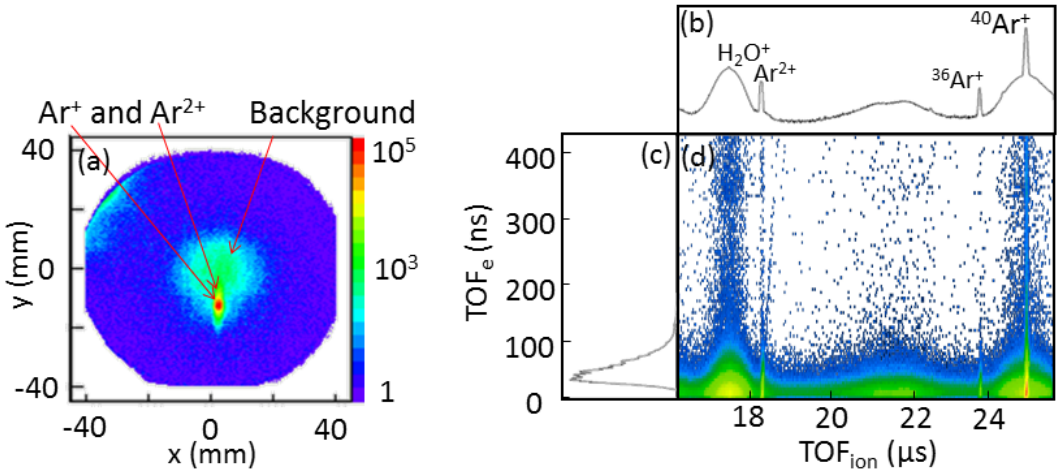

Figure 2.2: (a) Position, (b) ion TOF, and (c) electron TOF spectra for a typical COLTRIMS measurement of an argon target exposed to a strong laser field. Note that the argon species are offset from the background in the position spectra due to the jet velocity. Furthermore, the Ar^+ and Ar^{2+} are separated spatially as the longer TOF for the Ar^+ also means it will be further offset in the direction of the jet (-y). (d) Yield as a function of the electron TOF and the ion TOF, showing the coincidence lines.

giving rise to a more significant background signal. (3) The focusing mirror is $f = 25\,\text{cm}$, which does not allow for as tight of focus as the $f = 7.5\,\text{cm}$ mirror. (4) There are two meshes on each end of the spectrometer, which keep the electrostatic potentials flat. And, (5) the ion and electron sides of the spectrometer have equal length, which allows for achieving much higher electron resolution.

This COLTRIMS imaging technique was used to demonstrate the implementation of phase-tagging as discussed in Section 4.1 and in studies on correlated electron motion and double ionization addressed in Chapter 5.

2.2 LIMDI

The laser-induced molecular dissociation imaging (LIMDI) method for studying ion beams was developed by Ben-Itzhak's group [131, 132]. This technique utilizes a crossed laser-ion beam for studying molecular-ion beam targets via coincidence 3D momentum imaging.

Besides the obvious difference in charge, molecular ion beam targets differ from neutral targets in many ways. One major difference is that the neutral fragments, generated in dissociative processes of the molecular ion, carry a fraction of the beam energy and can thus be detected. This is particularly important for kinematically complete measurements of dissociation channels such as $H^+ + H$ from H_2^+, as is the case in Chapter 6. Another example is for certain charge asymmetric dissociation (CAD) channels, where one of the fragments is neutral, as is the case for $C^{2+} + O$ breakup from a CO^+ beam discussed in Chapter 3. Furthermore, molecular ion beams also have a Franck-Condon-like distribution of incoherent, stationary vibrational states, making them fundamentally different from studies on the ground state of a neutral gas target.

The experimental apparatuses for the molecular ion studies are shown schematically in Fig. 2.3(a) and (b). The main components of the beamlines are the ultra-high vacuum chamber, the ion source, ion beam optics, the laser beam optics, the spectrometer, and the detector. As is the case for COLTRIMS (see Section 2.1), the base gas pressure in the interaction region must be very good. A typical base pressure is on the order of 10^{-10} Torr.

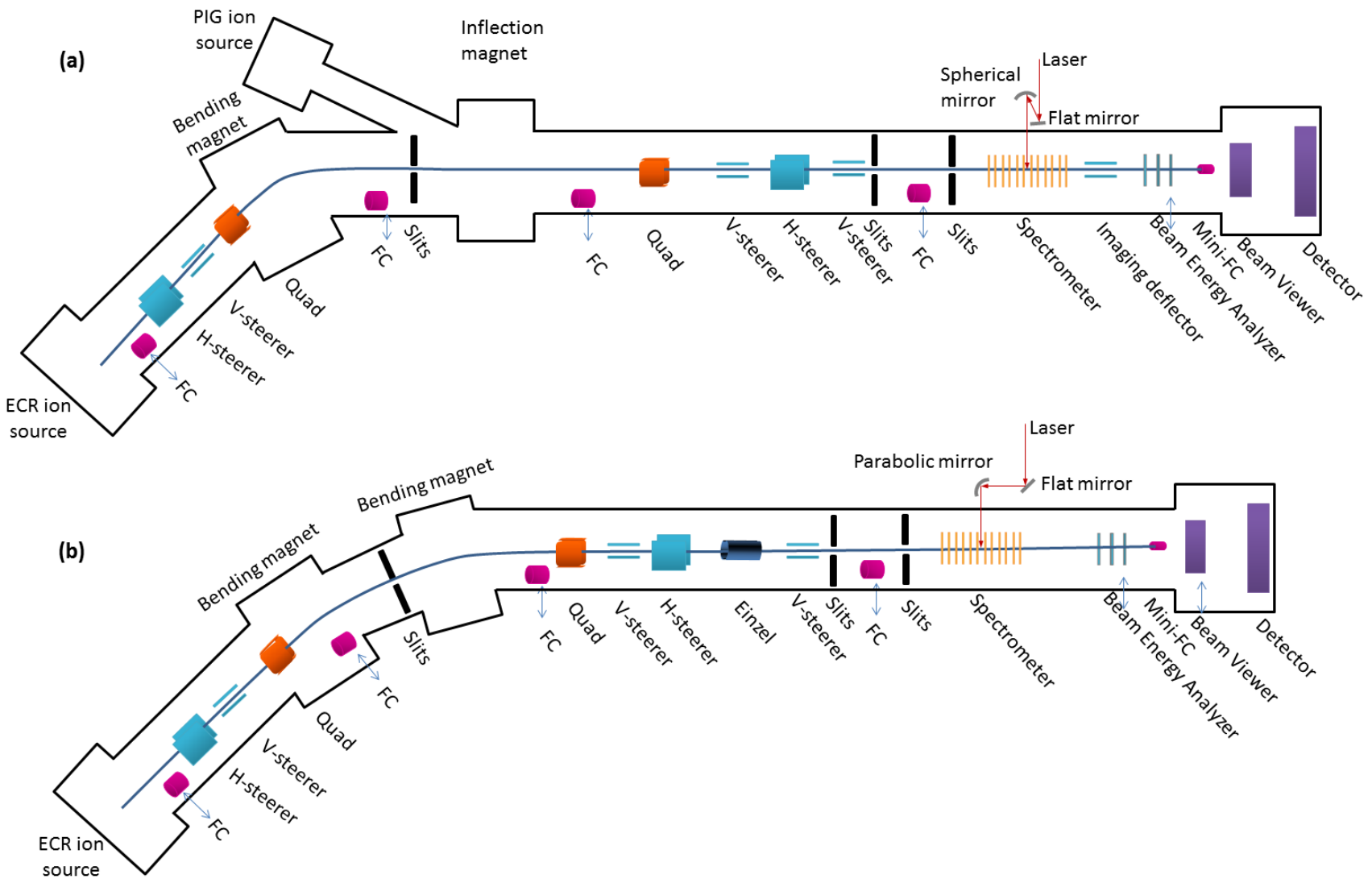

Figure 2.3: Top-view schematic of the ECR setup for experiments on (a) H_2^+ (see Chapter 6) and (b) CO^+ (see Chapter 3). H- and V-steerers move the ion beam horizontally and vertically through the beam path. Electrostatic quadrupoles (quad) and/or an einzel lens are used to focus the beam. Adjustable 4-jaw slits collimate the beam and reduce beam scatter. Removable Faraday cups (FC) are used to measure the current at different stages to aid in beam tuning. The laser crosses the ion beam path inside the spectrometer. In (a) a secondary Penning ion gauge (PIG) source is available, but was not used.

For brevity, only the setup used in the H_2^+ experiments is described here — see Fig. 2.3(a). An electron cyclotron resonance (ECR) ion source generates ions through electron impact ionization of a gas leaked into the source. As many ion species are generated in the ion source, a bending magnet selects the ion beam of interest. The current for each stage of beam tuning is measured in a retractable Faraday cup along the path. Four-jaw slits serve to collimate the beam and reduce scatter. A series of x- and y-steerers and quadrupoles are used to direct the beam through the small entrance hole (1 mm×1 mm) of the imaging spectrometer, where the interaction with the laser takes place, and ultimately to the last Faraday cup. The last Faraday cup is 2 mm in diameter and is mounted on an x-y manipulator stage, such that the cup can be aligned with the beam. A retractable beam viewer situated after the Faraday cup is used to visualize the ion beam to aid with the cup placement. Typical ion beam currents range from 0.5 to a few nA and the beam size is slightly less than 1 mm×1 mm.

A few other features of the apparatus are the beam energy analyzer, used to measure the beam energy distribution [133], and the imaging deflector, used to measure processes with low KER and undissociated molecular ions that have been further ionized by the laser [58].

The laser is focused onto the ion-beam target either by an off axis $f = 20.3$ cm parabolic mirror or by an $f = 25$ cm spherical mirror with a folded geometry. The parabolic mirror, with its shorter focal length, allows focusing to the highest intensities. However, it is difficult for manufacturing companies to make parabolic mirrors with high surface quality (our parabolic mirrors have a surface accuracy of $\lambda/4$). Spherical mirrors can easily be made with surface accuracies of $\lambda/10$, which makes them a better choice for experiments utilizing broad bandwidth laser pulses or when the carrier envelope phase of the laser pulse is important.

The laser-ion interaction takes place within the spectrometer. The spectrometer provides an electrostatic field which causes ionic fragments to accelerate according to their charge to energy ratio. In this way, neutral and ionic fragments resulting from laser-induced frag-

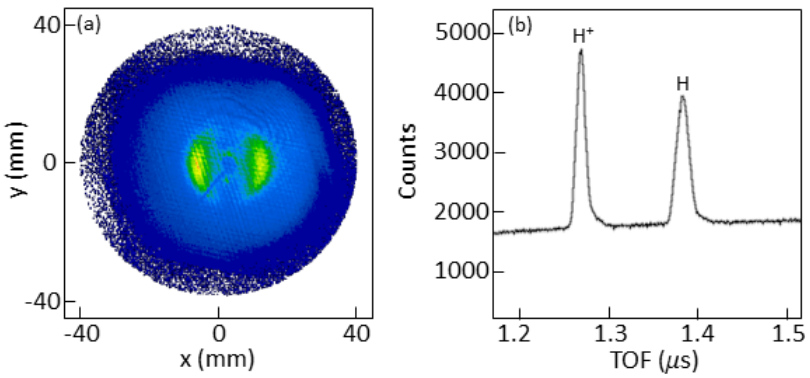

Figure 2.4: (a) Position and (b) TOF spectra for a H_2^+ molecular ion beam target exposed to a strong field laser, polarized along the x-axis.

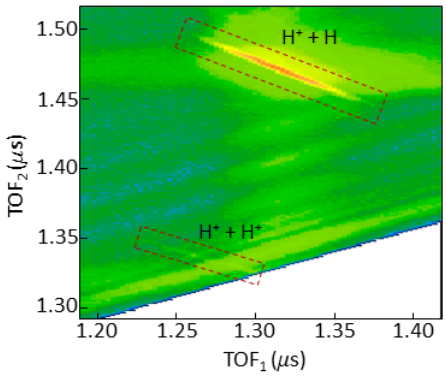

Figure 2.5: Yield as a function of TOF_1 and TOF_2 (raw data) for H_2^+ molecular ion beam target exposed to a strong field laser, where both dissociation ($H^+ + H$) and ionization ($H^+ + H^+$) channels are present.

mentation are separated by their arrival time to the detector. Similar to the COLTRIMS measurements, the fragments are detected on a time- and position-sensitive detector comprised of a chevron stack of MCPs and a delay line anode [130]. The position is evaluated from the signals picked off of both ends of each delay-line wire. The TOF is measured from the time difference between the laser incident on a photodiode detector and the signal picked off the MCP. By shining the laser on a spectrometer ring, some of the scattered light can be detected — called the "photon peak." This photon peak is used to determine "time zero," the time that the laser pulse interacts with the ion beam, with an accuracy on the

order of 100 picoseconds. More details on the signal processing electronics are summarized in Appendix A.

An example of the position and TOF spectra for laser-induced dissociation and ionization of an H_2^+ molecular ion beam target are shown in Figs. 2.4(a) and (b), respectively. A coincidence map can be used to separate the dissociation ($H^+ + H$) from ionization ($H^+ + H^+$) channels, as shown in Fig. 2.5 where the coincidence events are plotted versus the TOF of the first and second hits. Signal processing and the reconstruction of the 3D momentum is outlined in Appendix B and Refs. [52, 58, 134].

This coincidence 3D momentum imaging technique is applied to the charge asymmetric dissociation studies on CO^+ molecular ion targets in Chapter 3 and on pathway interference studies on a H_2^+ beam in Chapter 6.

2.3 Ultrafast Lasers

Four lasers were used in the work discussed in this dissertation. The Kansas Light Source (KLS) and the PULSAR lasers reside in the James R. Macdonald Laboratory at Kansas State University. The attosecond-1 (AS-1) laser is located at the Max Planck Institute for Quantum Optics (MPQ), and the Ludwig Maximilian University (LMU) laser is located at the LMU research campus, both in Garching, Germany. All four lasers have Ti:Sapphire based oscillators and amplifiers and thus have the same basic components. Therefore, in this Section I will give a brief general description of Ti:Sapphire lasers and tabulate the specific operation parameters for each laser in Table 2.1.

2.3.1 Ti:Sapphire Lasers

Titanium-doped sapphire based amplified laser systems easily generate intense ultrashort (fs timescale) laser pulses, making them the laser of choice for ultrafast strong-field studies. The Ti:Sapphire laser is a four-level vibronic laser, where the four levels involved are the low and high vibrational state of two electronic states of the medium, with a fluorescence

lifetime of 3.2 – 3.6 μs. The absorption band peaks around 490 – 500 nm making it suitable for pumping with frequency doubled neodymium-doped yttrium lithium fluoride (Nd:YLF) or neodymium-doped yttrium aluminum garnet (Nd:YAG) pump lasers.

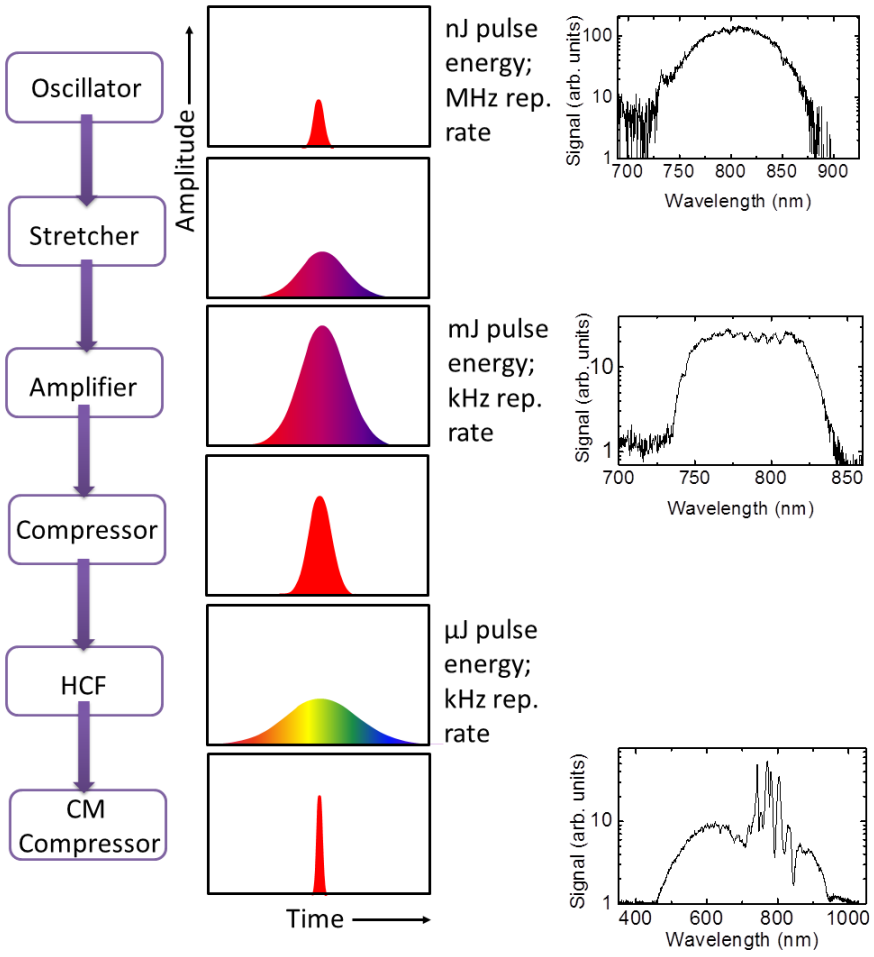

Figure 2.6: General scheme for Ti:Sapphire laser systems. Note that the spectra for the oscillator, amplifier, and Ne-filled hollow core fiber output are for the PULSAR laser.

The main components of the Ti:Sapphire laser are the oscillator, stretcher, amplifier, and compressor, as outlined schematically in Fig. 2.6. At the output of the compressor, the pulses have 20 – 40 fs duration. The pulse can be further temporally compressed to 4 – 7 fs by generating a super continuum in wavelength by spectral broadening in a rare-gas filled hollow-core fiber followed by a chirped mirror compressor (see Table 2.1 for specific

parameters regarding the lasers used).

The oscillator houses the mode-locked cavity which facilitates the broad bandwidth (typically around 100 nm, centered around 790 nm) and short temporal duration (typically 10 – 15 fs) of the laser pulses. The oscillator operates at around a repetition rate of 80 MHz and the typical pulse energy is a few nJ. In order to retain the bandwidth provided by the oscillator, yet decrease the peak power such that the amplifier optics do not reach their damage thresholds, a stretcher is used to chirp the pulse — the first step of the chirped pulse amplification scheme [135]. The stretcher for all four lasers discussed here is a grating pair. It is common to put the pulse picker or Pockels cell after the stretcher to select the pulse to be amplified in the amplifier crystal, and this is the case for the KLS, PULSAR, and LMU lasers. The Pockels cell for the AS-1 is after the fourth pass through the amplifier crystal, which helps to reduce amplified spontaneous emission contributions. The repetition rate is determined by the Pockels cell, and for the lasers discussed here, this is in the 1 – 10 kHz range.

The selected chirped pulse out of the stretcher provides the seed pulse for the amplifier. The amplifier contains another optically pumped Ti:Sapphire crystal. The beam passes through the amplifier many times, gaining energy each trip through a stimulated emission process. At the exit of the amplifier, pulses have energies on the mJ scale. By amplifying pulses at a lower repetition rate, higher energies of the ultrashort pulses can be achieved. This is why the LMU laser, which has a rate of 10 kHz has lower pulse energy (see Table 2.1). The PULSAR also has a 10 kHz rate, but a second amplification stage boosts the pulse energy up to 2 mJ.

As the pulses out of the amplifier are still chirped from the stretcher, they must be temporally re-compressed to generate the desired short pulse duration. The compressor stage consists of either another pair of gratings or a prism pair followed by chirped mirrors.

2.3.2 Ultrashort Pulse Generation with Hollow Core Fibers

The output of the Ti:Sapphire laser can be further spectrally broadened in a neon- or argon-filled hollow core fiber (HCF), as depicted in Fig. 2.7. The spectral broadening occurs via self-phase modulation (SPM), a nonlinear process caused by the Kerr effect [136]. Along with an increase in optical bandwidth, there is a large amount of positive dispersion acquired in the HCF. Negative dispersion is provided by a set of multi-layer chirped mirrors (CM) at the exit of the HCF. As the dispersion from a CM is finite, usually the beam is made slightly negative overall by the CM and a set of fused silica wedges are introduced to fine tune the chirp such that transform limited pulses are delivered at the interaction region of the experiment.

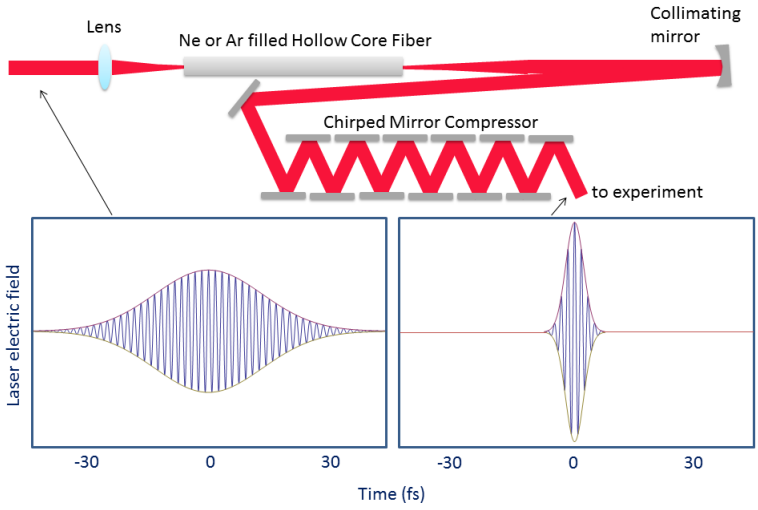

Figure 2.7: Schematic of the HCF setup for generating sub-10 fs pulses.

There are two competing quantities to consider when choosing the core diameter of a HCF, namely the amount of broadening and power throughput. Small diameter fibers are better for broadening, while large diameter fibers give higher throughput. A compromise must be made to satisfy both, and according to Ref. [137] it turns out that the beam diameter should be about 64% of the fiber opening at the entrance of the fiber. For example,

the HCF for the PULSAR laser has a diameter of 250 μm, and at the fiber entrance the beam size is focused to about 160 μm by a 1.5 m focusing lens.

The HCF was operated with two gases, namely argon and neon. To obtain the maximum spectral broadening, the gas pressure and the laser pulse energy are adjusted. One must be careful to avoid ionization of the gas, which would form an unwanted filament[2]. For our argon-filled HCF, the typical gas pressure is around 0.7 bar and the pulse energy into the fiber is about 450 μJ. In contrast, neon has a much higher ionization potential than argon. Thus, for our neon-filled fiber, a higher pressure of about 2 bar is optimal, and the pulse energy into the fiber is 850 μJ. Both gas-filled fibers produce a spectrum with the bandwidth ranging from about 450 – 1000 nm, with a power throughput of about 35 – 40 %. Thus, applications where higher pulse energies are desired, a neon-filled fiber should be used.

A high degree of laser stability is imperative for experiments where, for example, the CEP is important. One major source of instability through a HCF is the beam pointing fluctuations, which affects the coupling of the fundamental mode to the fiber entrance. Beam pointing fluctuations can be minimized by commercially available beam-pointing stabilization units. The AS-1, LMU, and PULSAR lasers are all equipped with beam-pointing stabilization units from TEM Messtechnik [139]. The KLS laser has a home-built stabilization system, called the automatic laser pointing stabilizer (ALPS) [140]. For the beam pointing stability system to work, a small portion of the beam must be picked off by a beamsplitter. This light (typically about 4%) is directed onto a four-quadrant detector placed the same distance away as the entrance of the HCF, the point where the beam pointing is to be locked. The detector signal is fed to a motorized mirror in the beam path prior to the beamsplitter. The mirror alignment is adjusted by the motor such that each quadrant of the detector has equal signal strength. The TEM Messtechnik design has a second four-quadrant detector which is fed back to a second motorized mirror in the beam path. The second feedback loop locks the beam pointing to a location about 0.3 m downstream

[2]Filamentation can provide spectral broadening too, but is undesired for the HCF method due to the the additional spatial chirp that it produces [138].

from the HCF entrance such that the angular deviations through the HCF entrance are also accounted for.

2.3.3 Diagnostics

For laser experiments, it is necessary to know the pulse duration, intensity, and spectrum at the interaction region with the target. Diagnostic tools vary from lab to lab. At the KLS, a home-built frequency-resolved optical gating (FROG) apparatus is used to measure the pulse duration, capable of measuring down to about 6 fs. In the AS-1, LMU, and PULSAR labs, an autocorrelator from Femtolasers is used, capable of measuring 5 to 150 fs [141]. When phase-tagging is employed, the pulse duration can be fairly well determined by the phase measurement (see Section 4 and Ref. [142] for more details). The spectrum for all lasers is measured with a fiber optic spectrometer from Ocean Optics [143], from which the bandwidth and central wavelength are determined. The intensity measurement varies with each experimental setup. The ion beam experiments (see Section 2.2), for instance, use a focusing element outside of the vacuum chamber, making it easy to insert a beamsplitter and image the focus with a charge coupled device (CCD) camera. From the spot size of the focus A, the power P, and the repetition rate f_{rep} of the laser, the intensity I is calculated as $I = P/(f_{rep}\,\tau\,A)$, where τ is the pulse duration. The COLTRIMS and VMI measurements have a back-focusing geometry and the focusing mirror is inside the vacuum chamber. For these experiments, the intensity is either determined from the ponderomotive energy, U_p, cutoff of a singly ionized target species [99, 144–146] or through an *in situ* comparison of the width of the longitudinal momentum peaks to theoretical calculations, such as Ammosov-Delone-Krainov (ADK) theory [22, 98, 147], as in Fig. 2.8.

In summary, this Chapter has outlined the experimental methods that were used in the studies covered in this dissertation. Phase tagging and thick-lens VMI are discussed in Chapters 4 and 7, respectively.

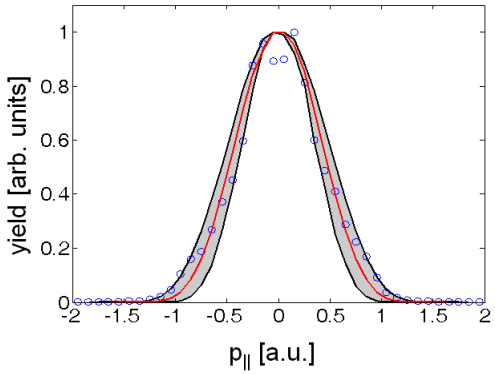

Figure 2.8: *In situ* determination of the peak intensity from the Ar^+ longitudinal momentum spectrum. The measured Ar^+ spectrum (open circles) and the ADK calculations (with a correction factor for over-the-barrier ionization [25]) for the best fit intensity of 3×10^{14} W/cm^2 (red line) as well as the lower intensity limit, 2.4×10^{14} W/cm^2 (inner black line), and the upper intensity limit, 3.6×10^{14} W/cm^2 (outer black line), indicating an error of 20%.

	KLS	PULSAR	AS-1	LMU
Osc. bandwidth (nm)	80	65	>100	>300
FTL Pulse Duration (fs)	30	21	21	23
Ctr. wavelength (nm)	795	790	780	795
Pulse energy (mJ)	2 (at 1 kHz)	2	1	0.5
Rep Rate (kHz)	1-2	10	3	10
Compressor	grating	grating	prism and CM	prism and CM
HCF gas	Ne or Ar	Ne or Ar	Ne	Ar
HCF pulse duration (fs)	5.5	sub-5	4	4
HCF pulse energy (mJ)	1.2	0.38 (Ne); 0.2 (Ar)	0.4	0.2
HCF ctr. wavelength (nm)	800	730 (Ne)	750	740

Table 2.1: Typical operation parameters for the KLS, PULSAR, AS-1, and LMU lasers. Acronym key: FTL = Fourier transform limited, CM = chirped mirrors. More details for the KLS can be found in Refs. [148–154] and for the AS-1 in Ref. [155].

Chapter 3

Charge Asymmetric Dissociation

This Chapter is based on Ref. [156], which reports our studies on the charge asymmetric dissociation (CAD) channel $C^{2+} + O$ from a CO^+ molecular-ion beam using a coincidence three-dimensional momentum imaging method. For these studies, the pulse duration was varied between 7 and 40 fs in order to assess the timescale of the dynamics leading to this CAD channel. Furthermore, the intensity was varied between 1.3×10^{15} and 6.0×10^{15} W/cm^2 to help shed light on the process by which the CAD channel is generated. These studies indicate that the probability of the CAD channel is higher for longer pulses at the lower end of the intensity range used here. In Ref. [156] we proposed a mechanism to explain these findings: first the CO^+ is excited to a dissociative state where it stretches, then it ionizes beyond critical potential energy curve crossings between the curves leading to CAD and the curves of the competing charge symmetric dissociation (CSD) channel. While we retain this as the basis for our interpretation in this Chapter, we also critically examine each step of the proposed mechanism in Section 3.3.

3.1 Previous Work

Charge asymmetric dissociation (CAD) is the fragmentation into two (or more) products where the charge is unevenly shared among the fragments. For example, for a diatomic molecule AB^{2+}, the charge asymmetric dissociation channels are $A^{2+} + B$ and $A + B^{2+}$ while the charge symmetric channel (CSD) is $A^+ + B^+$. Throughout this Chapter, the channels

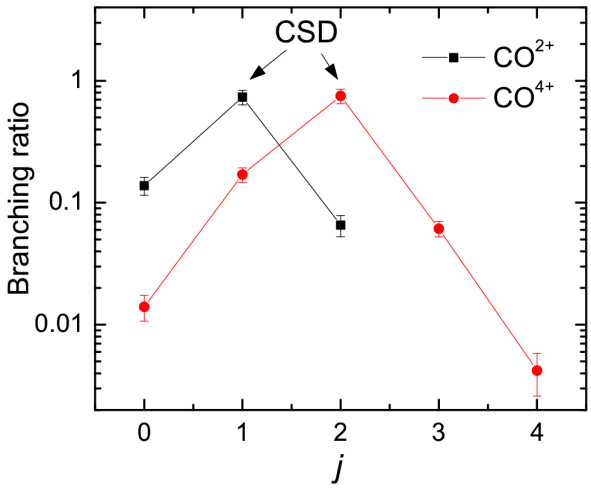

Figure 3.1: Branching ratio of the dissociation channels of transient CO^{q+} produced by 1 MeV/amu F^{q+} ion impact on CO, specifically for $CO^{q+} \rightarrow C^{i+} + O^{j+}$ for $q = 2$ and 4 and $i = q - j$, with lines added for visualization. The branching ratio is defined as the fraction of a specific breakup channel $C^{i+} + O^{j+}$ from the total of all channels associated with the same transient ion CO^{q+}. Both distributions indicate that symmetric charge breakup is strongly preferred. Note that the contribution shown for $q = 2$ does not add up to 1 as there is also a fraction of long-lived CO^{2+} ions, which is unaccounted for here. Adapted from Refs. [156, 157].

will be referred to as (i,j) where i is the charge of the lighter fragment and j is the charge of the heavier fragment.

Previously, it has been shown that highly charged molecular ions tend to dissociate into fragments with equal charge [157–159]. For example, in the "sudden ionization" of CO into CO^{q+} by 1 MeV/amu F^{4+} ions, the highly charged transient ion preferentially breaks into equally charged carbon and oxygen fragments, as depicted in Fig. 3.1. Furthermore, as the charge sharing becomes more asymmetric, the less likely the channel is to occur [157]. This distribution is consistent with the order the CO^{q+} charge states appear in energy. States leading to (1,1) — such as $X^3\Pi$ and $^3\Sigma^-$ — appear at much lower energies than the states leading to (2,0) or (0,2). Heuristically, charge symmetric dissociation ought to be the favorable channel from the simple argument that fast electrons have ample time to rearrange themselves on the nuclear centers during the course of dissociation.

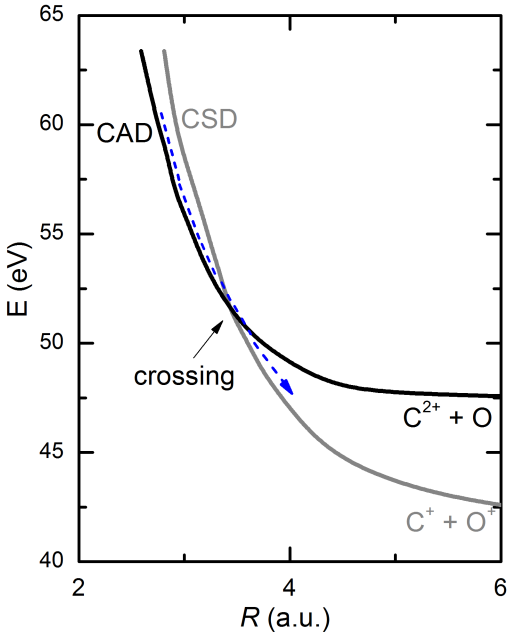

Figure 3.2: Schematically drawn potential-energy curves showing a crossing between curves that lead to CSD or CAD products. The pathway depicted by the arrows shows that, although the (2,0) channel can initially be populated, there is some propensity to dissociate onto the (1,1) channel, facilitated by charge transfer at the curve crossing between the (2,0) and the (1,1) states (see text).

A few potential energy curves for the low charge states of CO^+ are shown schematically in Fig. 3.2, suggesting another reason why the CSD channel is favored over the CAD channel. At small internuclear distance, R, the potential curve leading to the CAD products is lower in energy than the curve leading to CSD, which is highly repulsive at small R. Note that, in order for the curves to cross in the adiabatic picture, they must be of different symmetry, otherwise they will have an avoided crossing according to the Neumann-Wigner non-crossing rule [83]. The diabatic curves help illustrate where the strong coupling will occur, but the adiabatic curves contain more physics. It is important to note that for strong coupling, the adiabatic curves can look very different from the diabatic curves. At $R \simeq 3.5$ a.u., the potentials curves for (1,1) and (2,0) cross (see, for example Ref. [160]). Therefore at

$R > \sim 3.5$ a.u., the potential curves leading to CSD are lower in energy. Let us consider two scenarios involving the states in Fig. 3.2: (i) the ionization step promoting CO^+ to CO^{2+} occurs before the crossing and (ii) the ionization step occurs after the crossing. For (i), as the (2,0) curve is lower in energy, it is more accessible than the (1,1) curve. However, as the molecular ion starts to dissociate, it reaches the crossing, allowing population originally on the (2,0) curve to transfer to and dissociate via the (1,1) path, as indicated by the arrow on Fig. 3.2. Thus, even if the states leading to CAD are significantly populated, this channel can be dramatically reduced via transfer of the population to the (1,1) states through the crossing. For (ii) — assuming the CO^+ can stretch beyond the curve crossing before it is ionized — a simple energy argument shows that the symmetric charge state $C^+ + O^+$ will be preferred.

Despite the unfavorable conditions for CAD, this weak channel has been observed for many molecules in both weak and strong laser fields [66, 69–80]. A wide range of possible mechanisms for how the CAD channels are populated were suggested in these references. One example is that the states leading to CAD are populated by a vertical transition from the neutral ground state, as suggested in Ref. [69] for $N_2 \rightarrow N_2^{2+} \rightarrow N^{2+} + N$ with $50-110$ eV photons. Another explanation is derived theoretically by Mulliken [161], who proposed that CAD states can be reached from CSD states by means of a charge transfer transition, *i.e.*, $A^+ + B^+ \rightarrow A^{2+} + B$ [78, 162]. Gibson *et al.* experimentally studied CAD and CSD of I_2, suggesting that CAD of multiply charged states of I^{q+} (up to $q = 10$) is likely to occur via such charge transfer states [76]. However, more recent studies by Guo *et al.* indicate that charge transfer does not explain the appearance of CAD state population in smaller molecules, such as N_2 and O_2, as the dipole interaction energy is insufficient to populate the CAD states from the CSD states [74].

A large range of pulse durations (6 fs $-$ 10 ps) has been used to study CAD in the strong-field regime [66, 70, 74–77, 79, 80]. In all of these studies, the CSD channel is dominant. Longer laser pulses allow for excited molecules to stretch before they are ionized. If the

pulses are long enough, the molecule can stretch to the critical internuclear distance, where enhanced ionization is known to occur [163]. In contrast, CAD channels, such as the (2,0) channels for O_2 and N_2 [74] and for CO [75], are more visible for shorter pulse durations (30 and 6 fs, respectively). Nevertheless, a systematic study of the dependence of CAD on pulse duration has not yet been undertaken. Therefore, we asked the question: What happens to the likelihood of the CAD channel as a function of pulse duration?

In all previous work, a neutral target was studied, and only ionic fragments could be detected. The channels involving a neutral fragment, such as (2,0) CAD channels, had to be inferred from the data either by a process of elimination to identify which ions go with the undetectable neutral fragment or by taking advantage of the different kinetic-energy release (KER) range expected for the CAD channel (typically, one assumes that the doubly charged ion from a (2,0) channel is much less energetic than the one from the (2,1) channel). This may leave some doubts about the validity of the assignment of the CAD channel. The unambiguous measurement of the (2,0) channel requires measuring a charged fragment in coincidence with a neutral fragment as we have done in our studies.

3.2 Experiment and Results

In our studies on CAD, we generate a CO^+ ion beam at 9 keV energy in an ECR ion source. This beam is directed to the interaction region via steering and focusing elements along the ion beam path (for more details, see Section 2.2). We utilize a coincidence 3D momentum imaging technique, depicted in Fig. 3.3(a) and described in Section 2.2 and Refs. [131, 132], in which the C^{2+} and O beam fragments are measured in coincidence leaving no doubt about their channel assignment. When studying a 9 keV molecular-ion beam target, the neutral fragments are measurable, as they carry a large fraction of the beam energy. A typical coincidence map, where the yield is plotted as a function of the TOF of the first and second fragments, is shown in Fig. 3.3(b). The lines emerge due to fragmentation events that conserve momentum.

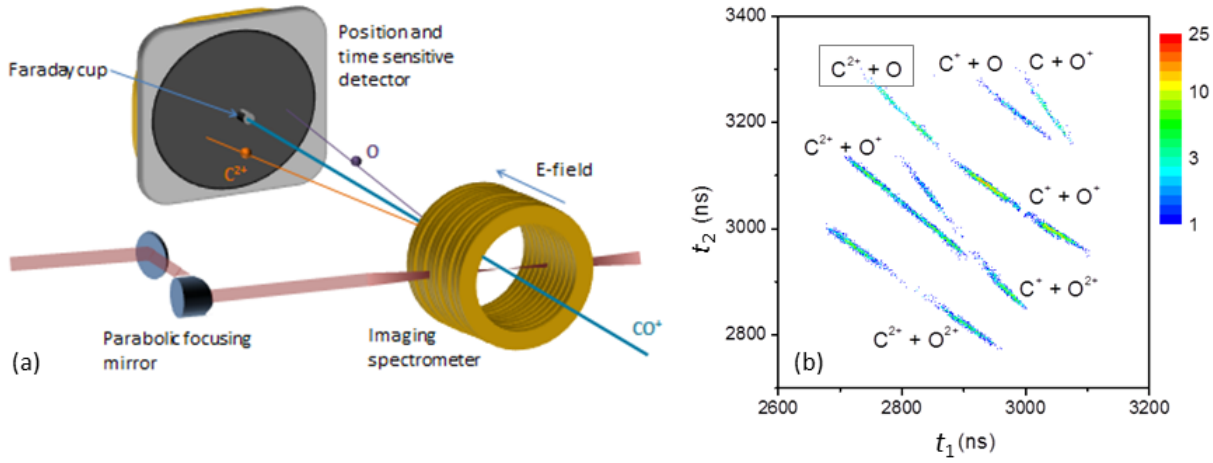

Figure 3.3: (a) Schematic of the experimental setup and (b) coincidence time-of-flight map of the various channels of CO^+ fragmentation from interaction with 40 fs 7×10^{15} W/cm^2 pulses with the CAD channel highlighted. Adapted from Ref. [156].

Our CAD studies were performed with the KLS laser, which is described in Section 2.3. The transform-limited pulses from the KLS vary between 28 and 40 fs, providing an upper limit for our pulse duration study. In order to achieve the 7 fs pulse, the spectrum was broadened in a neon-filled hollow core fiber (HCF) and negatively chirped by a set of chirped mirrors (see Section 2.3.2). All pulse durations were (near-) transform limited at the interaction region, achieved by adjusting a pair of thin fused silica wedges to minimize the second order dispersion. The 15 fs pulses were achieved by lowering the gas pressure in the HCF. All pulse durations were characterized by frequency resolved optical gating (FROG) [164].

The resulting KER spectra of the (2,0) channel for laser pulses with 7, 15, 30, and 40 fs duration and intensities 7.0, 5.0, 6.0, and 7.2×10^{15} W/cm^2, respectively, are shown in Fig. 3.4(a). For all pulse durations, the KER distributions peak at about 2.5 eV and have similar shapes. The KER distributions for linear- and circular-polarized 40 fs pulses are compared in Fig. 3.4(b). These spectra are normalized to each other by accounting for the differences in the ion-beam current and the laser spot size for each data set (for more

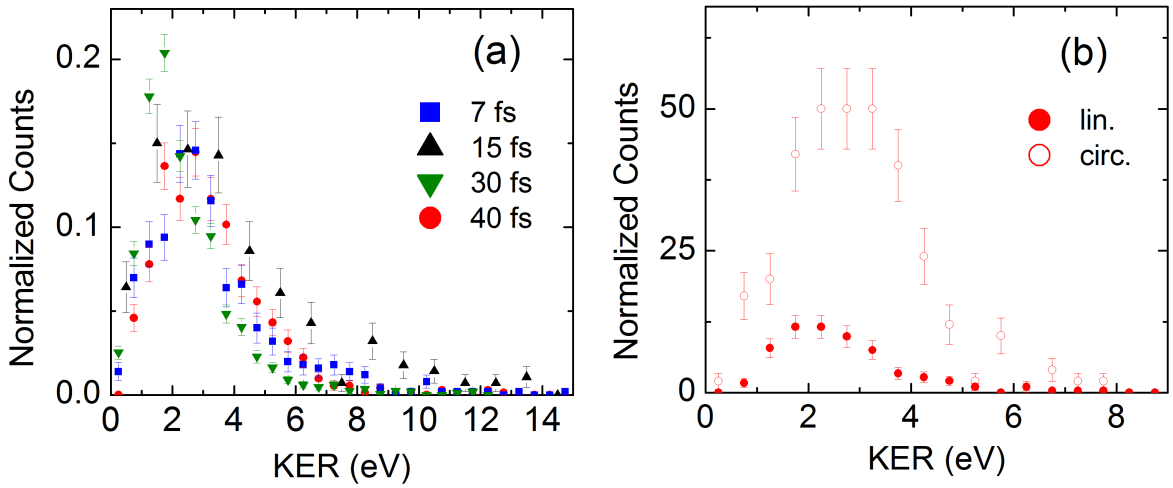

Figure 3.4: (a) KER distributions for the (2,0) fragmentation channel from CO^+ in 7, 15, 30, and 40 fs laser pulses with intensities of 7.0, 5.0, 6.0, and 7.2×10^{15} W/cm^2, respectively. Each distribution has been normalized such that the integrated number of counts is one. (b) KER distributions for the (2,0) fragmentation channel from CO^+ in 40 fs pulses with 3.6×10^{15} W/cm^2 for linear polarization and 7.2×10^{15} W/cm^2 for circular polarization (*i.e.* the same field strength). The linear and circular polarization pulses are normalized to each other as outlined in the text. The higher rate of $C^{2+} + O$ events for circular polarization suggests that electron recollision does not play an important role in this CAD process. Adapted from Ref. [156].

details, see Appendix D in Ref. [58]). The yield is not suppressed with circular polarization with the same laser field strength, suggesting that the driving mechanism, for this set of laser parameters, does not involve an electron recollision. If a recollision step were to play an important role, one would expect the signal strength to decrease significantly for circular polarization [165].

The CAD branching ratio, $N(2,0)/[N(2,0)+N(1,1)]$, where $N(i,j)$ is the number of observed counts for channel (i,j), is plotted in Fig. 3.5 as a function of pulse duration, where the intensity is approximately constant at $(5.0-7.2)\times10^{15}$ W/cm^2. This branching ratio increases with increasing pulse duration over the range of our measurements. In Fig. 3.5(b), the pulse duration is fixed at 30 fs and the intensity is varied from 1.3×10^{15} to 6.0×10^{15} W/cm^2. Here the branching ratio tends to decrease slowly with increasing intensity. Although detection efficiencies are not included in the CAD branching ratio evaluation, they

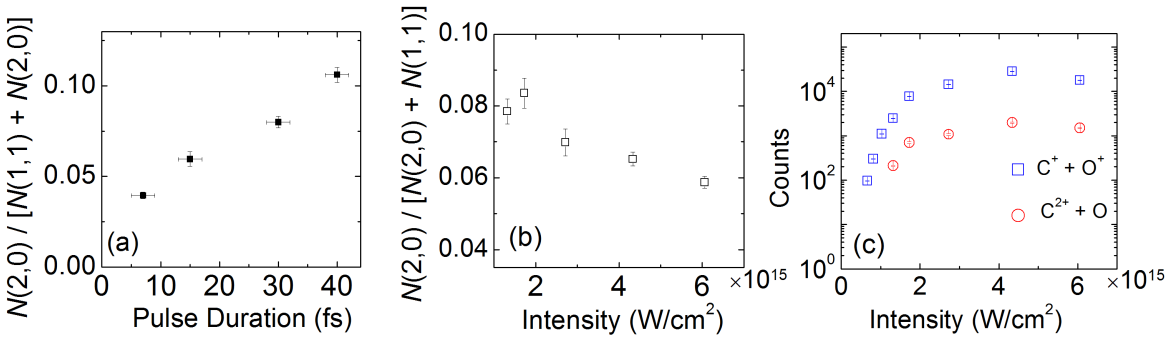

Figure 3.5: The CAD branching ratio $N(2,0)/[N(2,0)+N(1,1)]$ versus (a) pulse duration for an approximately constant intensity of $(5.0\text{-}7.2)\times10^{15}\,\mathrm{W/cm^2}$ and (b) peak intensity with constant pulse duration of 30 fs. (c) The number of counts versus intensity for the individual channels, as indicated. Vertical error bars denote statistical error. Note that the pulse duration measurement resolution is ±2 fs. Adapted from Ref. [156].

are expected to approximately cancel each other as the (2,0) channel suffers from the lower efficiency of the neutral oxygen but benefits from the higher efficiency of the doubly charged carbon. Meanwhile, the C^+ and O^+ fragments will have similar efficiencies in between the efficiencies of the C^{2+} and O fragments [166].

3.3 Interpretation

Although it is a great challenge to calculate potential-energy curves for CAD states as they are highly excited states of a molecular dication, Polák and Čížek [167] and Levasseur *et al.* [160] have evaluated the PECs leading to CAD for CO^{2+}. Therefore, our interpretation of the results presented here, and published in Ref. [156], relies on these available potential-energy curves for the CO dication. The $^1\Pi$ (2,0) state of CO^{2+} from Ref. [167] was chosen for illustration purposes (see Fig. 3.6 and the updated PECs in Fig. 3.9), as the PECs extend to larger R and include the dissociation limit, thus facilitating the evaluation of the KER via the reflection method. According to the valence bond theory carried out by Polák and Čížek [167], the (2,0) curves are strongly repulsive (*i.e.* steep at very small internuclear distance R. Meanwhile, the (2,0) curves and are weakly attractive at large R due to the

attraction between the doubly charged fragment and the polarized neutral fragment (which is proportional to $-1/R^4$). On the other hand, the PECs associated with the (1,1) channel are still strongly repulsive at large R due to the Coulomb repulsion between the C^+ and the O^+ fragments (which is proportional to $1/R$). This, combined with the fact that the dissociation limit of the (1,1) channel is lower than the (2,0) channel, is what leads to curve crossings in the diabatic representation between the states leading to the (2,0) and (1,1) channels for all state symmetries considered by Polák and Čížek [167] and Levasseur *et al.* [160].

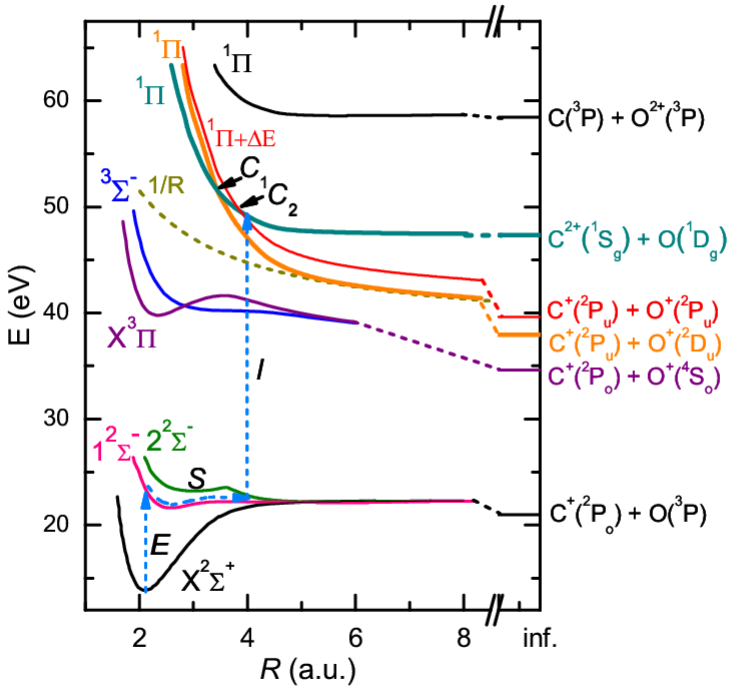

Figure 3.6: Potential-energy curves of select states of CO^+ and CO^{2+} from Refs. [167–169]. The dashed arrow sequence [excite (E), stretch (S), and ionize (I)] indicates a proposed pathway for reaching the (2,0) CAD channel (see text). Also shown schematically is the $^1\Pi$ CO^{2+} curve linked to the $C^+(^2P_u) + O^+(^2P_u)$ dissociation limit to indicate the sequence of crossings. The red curve, labeled $^1\Pi + \Delta E$, is constructed by adding the energy difference, $\Delta E = O^+(^2P_u) - O^+(^2D_u)$, to the $^1\Pi$ CO^{2+} curve shown with the limit $C^+(^2P_u) + O^+(^2D_u)$. Adapted from Ref. [156].

These PECs are coupled at the crossings (marked C_n in Fig. 3.6) where population can be transferred from the (2,0) channel to the (1,1) channel either through a crossing or an avoided crossing if the states involved have symmetries that allow for such a transition. It is important to note that there are a multitude of crossings between the lowest (2,0) state and the manifold of (1,1) states dissociating into excited C^+ or O^+ fragments. The transition rates at these crossings can be evaluated approximately, for example, by using the Landau-Zener theory [170, 171]. It is expected that the coupling between these states leading to CAD and CSD becomes weaker with increasing R [160]. Therefore, we hypothesize that efficient population of the (2,0) channel proceeds via a two-step process. First, the CO^+ ion is excited to a dissociating state of CO^+ thus initiating a stretch of the internuclear distance. Then, ionization occurs, and the fraction ending on the (2,0) state has a higher chance of avoiding transitions to CSD states if R has already stretched beyond the critical crossings responsible for depleting the CAD states. This scenario is depicted schematically in Fig. 3.6 by a sequence of arrows.

To summarize, the main points of the interpretation offered in Ref. [156] are (i) demonstrating experimentally that the CAD channel is reduced relative to the CSD with increasing pulse duration, although previous work suggests this should not be the case. (ii) We suggest that the CAD channel follows such a trend because it can be "depleted" through transitions with the CSD states. Regarding (ii), the interpretation presented in Ref. [156] has many weaknesses that have become apparent upon further careful consideration, and the continuation of experimental studies on this CAD channel and CO^+ dissociation in general. The following discussion thus serves to point out these weaknesses. We believe the gist of the interpretation of Ref. [156] to be a valid suggestion, however, for each step, exciting, stretching, and ionizing, some of the details have been overlooked. These problems, and their remedy, are addressed in the remainder of this Chapter.

3.3.1 Excitation

In Ref. [156], an example of a pathway was presented to show how the excitation and subsequent stretching might occur such that the ionization step takes place beyond the internuclear distance where there is a crossing between the states leading to the CAD and CSD channels. This pathway assumed that the initial population of the CO^+ ion beam was in the ground $X^2\Sigma^+$ state. The stretching was suggested to occur via excitation from the CO^+ ground state to an excited $^2\Sigma^-$ state. Unfortunately, for Σ symmetry, a transition from $\Sigma^+ \rightarrow \Sigma^-$ does not follow the dipole selection rules [83].

Recently our group has upgraded the experimental setup to allow efficient frequency doubling of the laser. This gave us access to explore the same dissociation and ionization processes in CO^+ with a wavelength of about 400 nm. These experiments, lead by my colleague, Utuq Ablikim, provided new information suggesting that the $a^4\Sigma^+$ state of CO^+ is present in the ion beam, and that dissociation mainly occurs from this state [172].

3.3.2 Stretching

Having realized that the transition $\Sigma^+ \rightarrow \Sigma^-$ is not allowed, and given the strong experimental evidence for the dissociation from the $a^4\Sigma^+$ state, another pathway for the stretching step is presented here. Note that the exact pathway as to how the molecule stretches is not a critical factor for this story. Furthermore, the availability of potential energy curves is quite limited, so nailing down the exact pathway remains a challenge. However, using the PECs that are available, a plausible pathway for the CO^+ stretching step, which is consistent with the present data, is presented below.

One possible way to stretch the CO^+ bond is to excite to a dissociative state of CO^+. In the experiment, all of the channels that dissociate upon interaction with the laser are measured. Therefore, we have collected the (1,0) channel under the same experimental conditions as the (2,0) channel. The KER and angular distributions of the (1,0) channel (shown in Fig. 3.7) provide some evidence for which potential energy curves may be involved

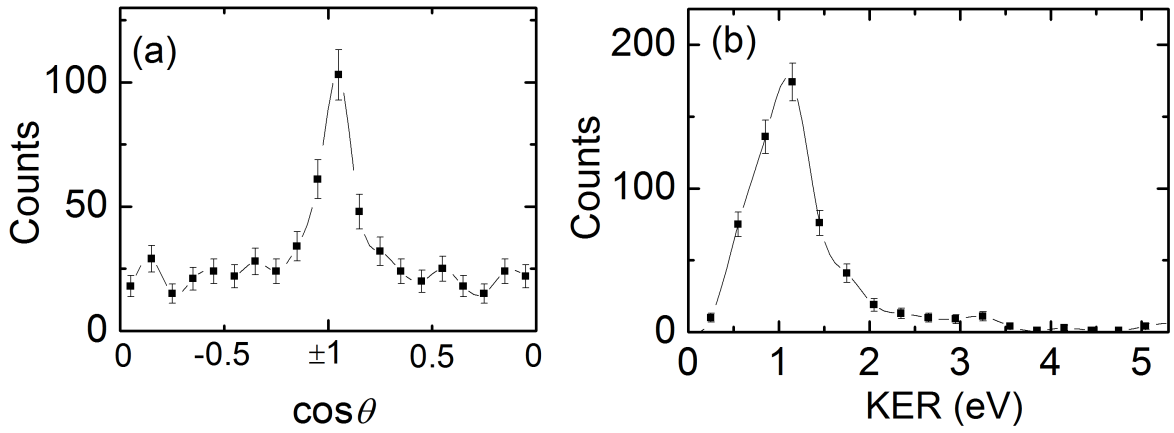

Figure 3.7: The (a) angular distribution and (b) KER spectra for the $C^+ + O$ dissociation channel with linearly polarized 40 fs 3.6×10^{15} W/cm^2 pulses. Adapted from Ref. [156].

in such a pathway. The angular distribution seems to have a strong component at $\cos\theta = \pm 1$ suggesting that $\Delta\Lambda = 0$ [83]. However, there is also an equally significant contribution which appears as an isotropic distribution. In order to observe an isotropic distribution, a transition where $\Delta\Lambda = 1$ must be involved. The transition $a^4\Sigma^+ \rightarrow 1^4\Pi$ is thus consistent with the observed angular distribution and is available in literature [169].

Using the reflection method [173, 174], we estimate that, if the excitation occurs from the bottom of the $a^4\Sigma^+$ well, a KER of about 1 eV is obtained. This is in good agreement with the KER data for the (1,0) channel[Fig. 3.7(b)]. We refer to this transition as bound-free (BF), as the energy on the $1^4\Pi$ state is above the dissociation limit. However, according to the Franck-Condon principle [83], the ionization from the ground vibrational state of CO to the $a^4\Sigma^+$ state of CO^+ indicates that most of the population is in the middle of the $a^4\Sigma^+$ well. Starting from the vibrational states in the middle of the well, the CO^+ can be excited via a bound-bound (BB) transition to the $1^4\Pi$ state, and also stretch significantly. This process would not contribute to the (1,0) signal, but could also play a role in the dissociative ionization process.

For the BF excitation, classical propagation on the $1^4\Pi$ state was used to estimate the time needed for the CO^+ to stretch to a given R. The result is shown in the inset of Fig.

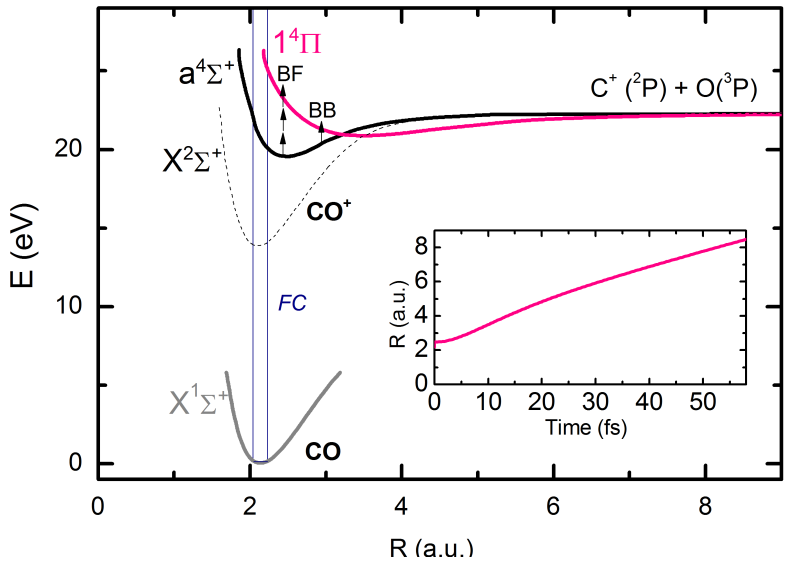

Figure 3.8: Potential-energy curves for CO [175] and CO^+ [169], with the approximate Franck-Condon (FC) region indicated. The arrows — whose length represents the photon energy — labeled BF and BB indicate bound-free and bound-bound transitions, respectively. The inset shows the classical propagation time for the dissociation along $1^4\Pi$ starting from $R = 2.47$ a.u., the equilibrium distance for the $a^4\Sigma^+$ state (see text).

3.8. The time needed for reaching an R of about 5 a.u. is just over 20 fs.

3.3.3 Ionization

In order to determine the approximate internuclear distance where the ionization step takes place, the reflection method was used to the (2,0) channel, which exhibits a KER peaked at about 2.5 eV. Given an energy of about 1 eV from the stretching step, the reflection method suggests that the ionization step is around $R \simeq 4$ a.u., such that the remaining 1.5 eV is gained via dissociation along a (2,0) curve.

With the $1^4\Pi$ CO^+ curve being a viable PEC identified for the stretching step, calculating the time for classical propagation along the curve leads to an estimated time needed to reach a given R when starting from the R_0 of the $a^4\Sigma^+$ state of CO^+. The classical propagation calculation, shown in the inset of Fig. 3.8, suggests it takes approximately 13 fs to stretch to an R of 4 a.u. on the $1^4\Pi$ state of CO^+. Similar to the interpretation of Ref. [156], if the

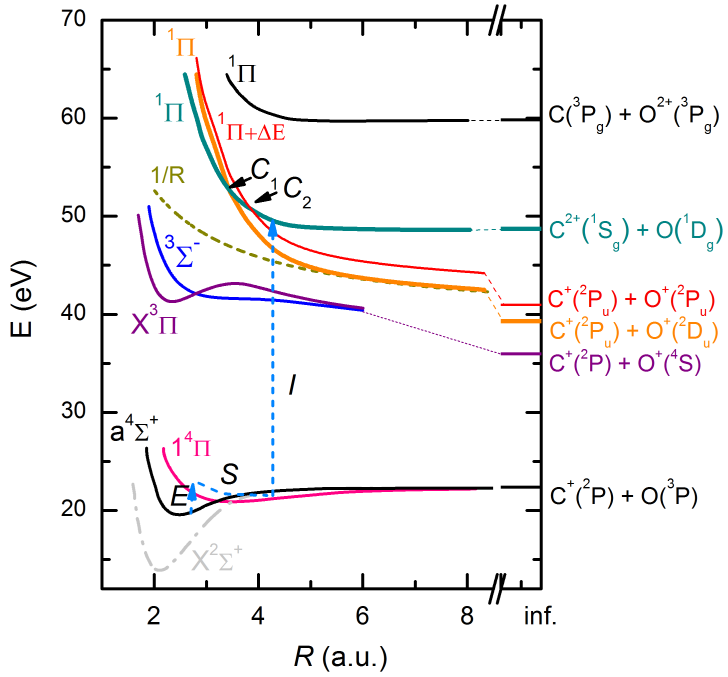

Figure 3.9: Potential-energy curves of select states of CO^+ and CO^{2+} from Refs. [167–169]. The link between the energy scales at small R and the dissociation limit was determined by D_0 for CO, quoted in Bransden and Joachain [83] to be 9.6 eV, which was the value used in Ref. [156]. However, $D_0 = 11.092$ eV, taken from Huber and Herzberg [176], which seems to be more correct, was used here. Also the $D_0 = 8.338$ eV for CO^+ was taken from the same source, Ref. [176]. The dashed arrow sequence [excite (E), stretch (S), and ionize (I)] indicates a proposed pathway for reaching the (2,0) CAD channel (see text). Also shown schematically is the $^1\Pi$ CO^{2+} curve linked to the $C^+(^2P_u) + O^+(^2P_u)$ dissociation limit to indicate the sequence of crossings. The red curve, labeled $^1\Pi + \Delta E$, is constructed by adding the energy difference, $\Delta E = O^+(^2P_u) - O^+(^2D_u)$, to the $^1\Pi$ CO^{2+} curve shown with the limit $C^+(^2P_u) + O^+(^2D_u)$. Note that the $^1\Pi$ states of CO^{2+} are in the diabatic representation, while the others are in the adiabatic representation.

laser pulse is still intense enough to ionize this excited state of CO^+ to CO^{2+}, there is some probability of ionizing to CO^{2+} states that lead to the (2,0) channel (see Fig. 3.9 for the updated curves). Note that the main crossings with the CSD curves are believed to be at a slightly smaller R of about 3.5 a.u.. According to this, longer pulses (with a "slow" rise of intensity) should result in better chances for populating the CAD states. This is consistent

with the results plotted in Fig. 3.5(a) showing the branching ratio as a function of pulse duration. The increased survival rate of the CAD channel is attributed to the reduced depletion of the CAD population due to charge transfer. However, if the pulse duration is too long, the enhanced ionization pathway opens up, which again prefers the CSD products indicating that there is a window of pulse durations where CAD can occur with higher probability. Therefore, it is expected that the CAD branching ratio will decrease for pulse durations longer than 65 fs, the pulse duration needed to open the enhanced ionization process according to Ref. [177], which is beyond the extent of our data.

The trend for the branching ratio as a function of intensity [see Fig. 3.5(b)] is also consistent with the proposed mechanism and for similar reasons. For a fixed pulse shape (duration), the time difference between the CO^+ excitation step, which requires a high intensity, and the ionization step becomes shorter with increasing intensity. This is due to the typical shift in ionization to smaller R with increasing laser intensity as the stronger field can bridge the increasing energy gap at smaller R [178].

While the diabatic potential-energy curves are useful for visualizing where the crossover from the CAD to the CSD states might occur, their calculation includes less physics. For instance, curves with the same symmetry cross in the diabatic representation, but do not cross in the adiabatic representation (according to the Neumann-Wigner non-crossing rule [83]). The diabatic and adiabatic curves from Ref. [167] are shown in Figs. 3.10(a) and Figs. 3.10(b), respectively. Note that the diabatic states are clearly labeled, but the adiabatic curves are not. The fact that the two sets of curves look very different from each other makes identification of each curve difficult. For example, the lowest curve exhibits a repulsive character in the diabatic representation, and is metastable in the adiabatic representation. This suggests that there is a strong coupling between these states — such significant structure modifications are expected to affect the physical processes, such as the charge transfer depletion described above. Meanwhile, it is difficult to discuss depletion within the adiabatic representation, since in the region of R that we are interested in, the

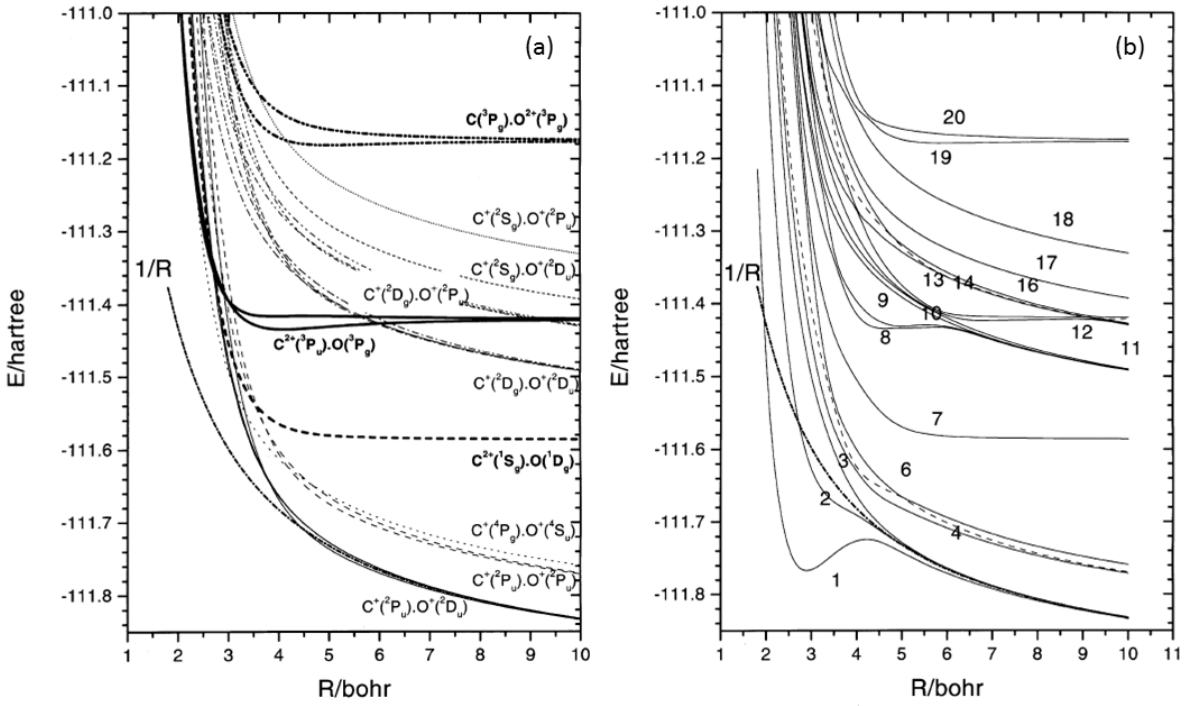

Figure 3.10: (a) Diabatic and (b) adiabatic potential-energy curves, adapted from Ref. [167]. All states have $^1\Pi$ symmetry.

states leading to CSD and CAD are mixed. This means that it is not the CAD states specifically which are getting depleted, but rather the mixed states leading to the (2,0) dissociation limit.

To arrive at a proper interpretation, one would need to either use the adiabatic potentials, use the full solution of the diabatic problem including the strong diabatic coupling, or have crossings be located outside the range of the strong diabatic coupling. With the current level of PEC calculations, though, these options are not available to us. The Polák reference does calculate the adiabatic curves and gives the coupling between a few selected curves, but it only considers states with one symmetry, namely $^1\Pi$ [167]. Furthermore, the labeling of the adiabatic states is unclear to a non-specialist [see Fig. 3.10(b)]. Meanwhile, in the Levasseur reference, there are many symmetries considered, but all of the states leading to (2,0) are non-adiabatic and the dissociation limit is unspecified, making the curves unsuited

for describing physical pathways.

3.3.4 $C + O^{2+}$

One may wonder why the other CAD channel, namely, dissociative ionization into $C + O^{2+}$, is not observed in our data and how this is consistent with our interpretation of the CAD mechanism. The main reason for the lower (0,2) rate is the fact that the PEC leading to this CAD channel is much higher in energy due to the higher ionization potential of oxygen relative to carbon (by more than 11 eV). Therefore, a larger number of photons is needed to ionize to this CAD state, making it much less likely (see Fig. 3.9). However, that cannot be the whole story as we observe even higher ionization levels in our data, *i.e.* the (2,1), (1,2), and (2,2) channels [see Fig. 3(b)], and further work is needed to explain the dominance of multiple ionization over this charge asymmetric dissociative ionization.

3.4 Summary

In summary, using a coincidence 3D momentum-imaging technique, we unambiguously studied the (2,0) CAD channel of CO^{2+} using a CO^{+} ion-beam target. We find that the CAD branching ratio, namely, $N(2,0)/[N(2,0) + N(1,1)]$ decreases with decreasing pulse duration below 40 fs. This is in contrast to previous reports of CAD of CO with ∼800 nm wavelengths, which suggested shorter pulses should lead to more CAD. Furthermore, this CAD branching ratio decreases slightly with increasing intensity. The present measurements suggest that the CO^{+} stretches, for example on an excited state of CO^{+} before ionization leading to the (2,0) channel. We suggest that these results can be explained by three steps: excitation, stretching, and ionization, where the stretching allows reaching R's greater than where curve crossings might occur between states leading to CAD and CSD. Ionization after the crossing suppresses the potential depletion of the CAD population.

To nail down which pathway(s) are involved in each step requires further exploration and, in some cases, *ab-initio* structure calculations. Furthermore, the diabatic PECs, while illus-

trative in some cases, are not well-suited for describing the suggested depletion mechanism of the transfer of charge at the crossing $C^{2+} + O \rightarrow C^{+} + O^{+}$.

A rigorous way to test the proposed CAD mechanism would be to perform a pump-probe measurement. One could use a CO^{+} or CO^{2+} beam as the target molecular ion. The latter likely would give a cleaner signal, whereas the former would be easier for technical reasons. A short (5 fs or less) pump pulse could initiate the stretching and a delayed short probe pulse would be utilized to populate the CAD channel. By varying the delay between the two pulses, the time evolution could be studied in detail giving insight into the dynamics that seem to occur between states leading to CSD and CAD final states.

Chapter 4

Phase Tagging

The carrier-envelope phase (CEP) is an important parameter for few-cycle laser pulses. The CEP refers to the difference between the maxima of the carrier and envelope of the electric field of the light pulse, as shown in Fig. 4.1. Technology to lock, or stabilize, the CEP of ultrashort laser pulses has been developed [179] and implemented in many modern laboratories, for example see Refs. [45, 148, 180–185]. It has been experimentally [45, 98, 104, 105, 110, 116, 118, 121, 180, 186–189] and theoretically [84–86, 89, 108, 112, 190, 191] demonstrated that the CEP of a laser pulse can be used as a control parameter governing, for example, spatial asymmetries which arise from pathway interference. Typically, the CEP can be locked for several hours with phase resolution on the order of 10^2 mrad [192–194]. Locking the CEP is therefore a good option for studying CEP effects if the desired experimental statistics can be acquired before the laser loses CEP lock.

As noted in Section 2.2, the target density of an ion-beam target is very low. This attribute of the ion beam necessitates long data acquisition times due to the associated small count rates [131]. A similar limitation is imposed by the COLTRIMS, as coincident detection of particles requires a counting rate of less than one event per laser pulse [127, 128]. These already challenging experiments become nearly impracticable when exploring CEP effects with phase locked lasers.

Recently, a solution to this technical problem has been developed, namely CEP tagging [99, 123, 195]. In this method, a stereographic above threshold ionization (ATI) phase meter

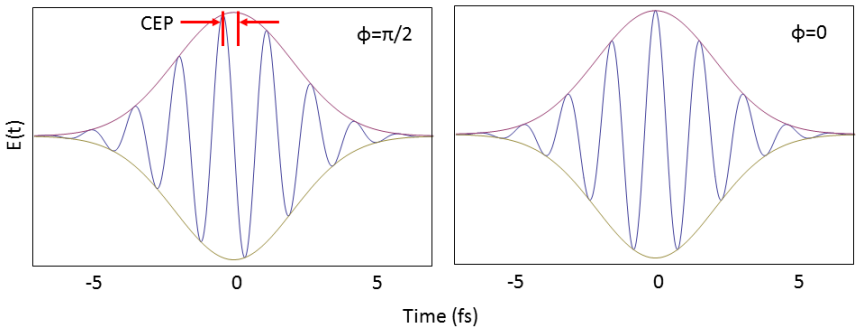

Figure 4.1: Electric field for a 5 fs laser pulse for two CEP values, indicating that even a small change in the CEP results in a significant change in the carrier pulse shape.

is used to monitor the high-energy electrons involved in ATI of Xe atoms. The concept for the phase meter was first developed by Paulus and co-workers [196, 197], and was further technologically improved to work on a single shot basis by Wittmann *et al.* [123]. Phase tagging was implemented for the first time by Johnson *et al.* showing the experimental practicality regarding experiments where long data acquisition times are necessary, using COLTRIMS as a demonstration [99]. Since then, Kübel *et al.* has refined the phase tagging technique to improve its accuracy by accounting for small drifts in the laser parameters throughout the experiment [198]. This becomes especially important regarding CEP dependent yield measurements, which are sensitive to the experimental parameters (such as intensity and pulse duration).

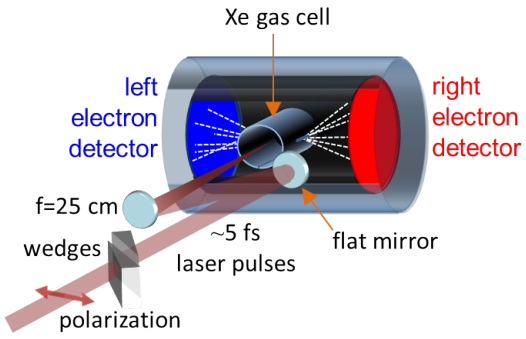

Figure 4.2: Schematic depiction of the phase meter, adapted from Ref. [99].

A schematic of the phase meter is shown in Fig. 4.2 (for an overview of the phase meter design, see Appendix C). The second order dispersion of the short laser pulses is optimized by thin fused silica wedges on an adjustable translation stage. Once the dispersion is properly accounted[1] for, the wedges remain stationary for the duration of the experiment. The pulses enter the phase meter by a folded geometry — a flat mirror followed by an $f = 25\,\text{cm}$ focusing mirror — which introduces a slight, but non-critical, astigmatism to the focus. Here the pulses interact with a 10^{-2} Torr sample of Xe atoms confined in a gas cell. The gas cell has two 1mm (vertical) $\times$2mm (horizontal) slits allowing ionized electrons to exit the cell to the left and right along the laser polarization axis. The vertical dimension of the slits is kept small such that there is good differential pumping between the cell and the detectors, which need a pressure below 10^{-5} Torr for safe operation. The horizontal dimension of the slits is slightly bigger to ensure that enough electrons can reach the microchannel plate (MCP) detectors for single shot operation. In front of the detectors are two flat high-transmission (88%) meshes. The first mesh is set to ground potential, such that the interaction and electron flight regions are field free. The second mesh is set to about $-28\,\text{V}$ to block the low-energy direct electrons, which would saturate the detectors and ultimately reduce the life-time of the MCPs. The time-of-flight (TOF) of the high energy electrons is determined from the time difference between the laser light pulse detected by a fast photodiode near the phase meter apparatus and the electron signal taken from the metal anode of the detectors.

The TOF signals from both detectors are sent to a processing unit, where they are divided into two regions, TOF_1 and TOF_2, as shown for one laser pulse in Fig. 4.3(a). The individual regions are further processed by integrating the signals on the left and right detectors within the TOF_1 and TOF_2 gates, and the normalized difference, $A_{1,2} = (N_L - N_R)/(N_L + N_R)$, which varies from -1 to 1, is calculated. Plotting A_1 versus A_2 results in a parametric asymmetry plot (PAP), commonly referred to as a "phase potato." A typical PAP for sub-5 fs pulses is shown in Fig. 4.3(b).

[1]The dispersion is adjusted such that the shortest possible pulse duration is achieved, determined by maximizing the size (radius) of the PAP.

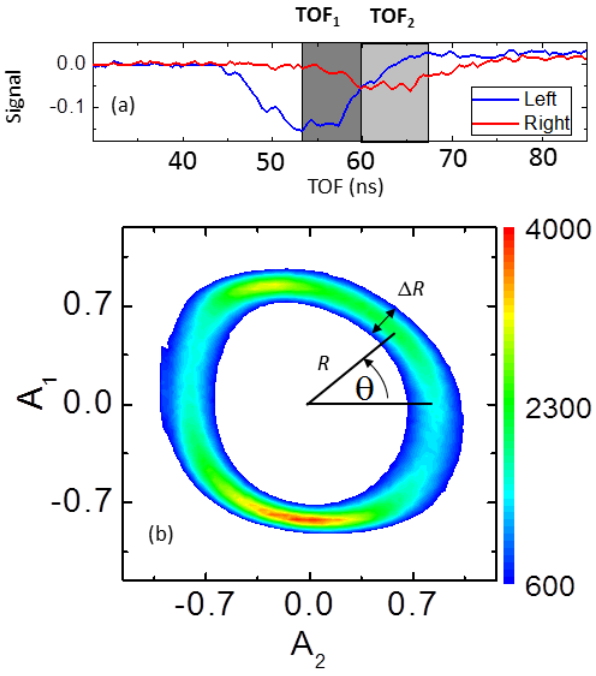

Figure 4.3: (a) TOF signals from a single laser pulse in the stereo-ATI phase meter and (b) PAP for many laser shots with sub-5 fs pulse duration, where θ here is related to ϕ through a transformation (see text). Adapted from Ref. [99].

From the PAP, the CEP, ϕ, of the laser pulse can be determined. The extraction of ϕ from the PAP relies on the assumption that the CEP of the laser is random over the duration of the measurement. This assumption can be tested by comparing the PAPs generated with slightly varied amounts of chirp compensation glass (different wedge positions), which shifts ϕ_0, the offset in ϕ. If the CEP is random, the shape of the PAP should not change as a shift in ϕ_0 is introduced. In contrast, if the CEP is not random, a shift in ϕ_0 would result in a rotation of the PAP. Note that the shape of the PAP is mostly determined by the TOF gates. The angle θ, defined in Fig. 4.3(b), is directly related to the CEP. The relation is obtained by dividing the PAP into several θ bins (depending on the resolution) where the number of counts in each bin is equal. This results in a transformation from θ to ϕ, as shown in Fig. 4.4(a). Figures 4.4(b, c) show histograms for θ and ϕ, the latter being the

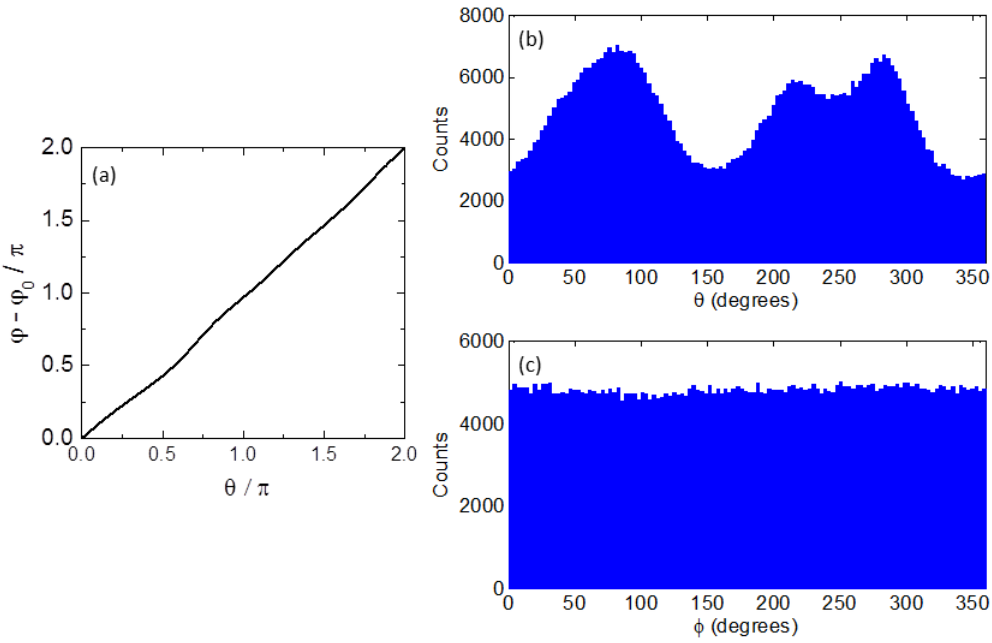

Figure 4.4: (a) Transformation from measured PAP angle θ to CEP, ϕ, (b) histogram of θ, and (c) histogram of ϕ.

result of the assumption that the CEP of the laser is random. More details on how the CEP is determined from the PAP can be found in Refs. [99, 199]. Furthermore, the PAP itself is indicative of the pulse duration and CEP resolution. A larger PAP radius, R, corresponds to a shorter pulse duration [142] and a thinner PAP (i.e. small ΔR) corresponds to a higher resolution [199].

For a single shot measurement, phase tagging is simply a matter of synchronizing the signals in an experiment with the signals generated by the phase meter. We do this by triggering our electronics readout with a fast photodiode. Care must be taken such that the order of triggering is done correctly, as it varies from setup to setup. As the processing unit outputs a voltage level, reached only after about 50 μs, a delayed trigger to the unit reading the CEP signal (such as an analog to digital converter) is needed.

4.1 Phase-Tagged COLTRIMS

As a proof-of-principle for the phase-tagging technique, the non-sequential double ionization (NSDI) of argon was studied using COLTRIMS [99]. Non-sequential double ionization is the enhancement of the double to single ionization ratio, as the laser intensity is reduced [39]. Experimentally NSDI of argon has been shown to exhibit a strong CEP dependence on the longitudinal momentum [200], and theoretically on the total double ionization yield [201]. Total yields are difficult to measure as a function of CEP, especially with CEP-locked laser pulses. To sweep through the 2π CEP range with a CEP-locked laser, dispersive material must be introduced to the path. This is typically done with a pair of fused silica wedges — one wedge is stationary while the other is translatable. The dispersion introduced by the glass allows small changes of the CEP, but it also inadvertently introduces small changes to the pulse envelope, which affects the pulse duration and peak intensity. These changes make it difficult to know if the yield is changing due to the CEP or due to the reduced intensity. Phase tagging circumvents these issues, limited only by the stability[2] of the laser, which can be up to several days.

Non-sequential double ionization has been explained as an inelastic laser-driven recollision mechanism [200], which can be described as three steps [31–33]. First, an electron is tunnel ionized. Second, the freed electron is driven by the laser field. Third, under certain circumstances, the electron recollides with its parent ion. Upon recollision a wealth of phenomena can occur, including high harmonic generation [202], above threshold ionization [38], frustrated tunneling ionization [203], and NSDI [200].

Regarding NSDI, depending on the energy of the returning electron, the parent ion can be excited and ionized later in the pulse through recollision excitation with subsequent ionization (RESI) or directly ionized (e, 2e). For the intensities studied in this work, the main mechanism was found to be RESI (also referred to as recollision-induced excitation

[2]For example, small changes in the laser output power or bandwidth accumulated over time due to fluctuations in temperature or humidity in the lab.

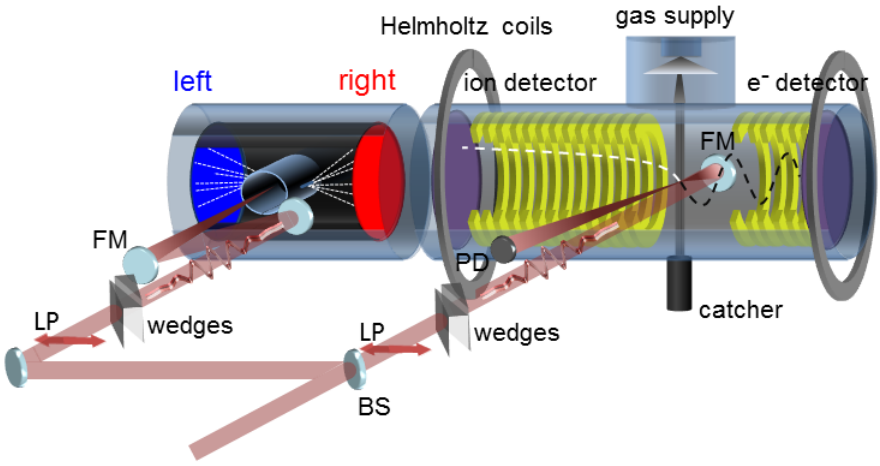

Figure 4.5: Sketch of the setup for phase-tagged COLTRIMS measurements, adapted from Ref. [99]. Short linearly polarized (LP) laser pulses are divided by a broadband beamsplitter (BS), and each arm has adjustable wedges for dispersion compensation. About 30 μJ are focused into the Xe-filled gas cell of the phase meter. The gas cell has two slits, allowing electrons to exit the cell and travel to the left and right detectors along the laser polarization. The laser transmitted (about 25 μJ) through the beam splitter is back focused by a 27 cm focusing mirror (FM) onto the supersonic gas jet in the COLTRIMS chamber. A static electric field supplied by the spectrometer of the COLTRIMS directs ions to the ion detector and electrons (when measured) to the electron detector. When electrons are detected in the experiment, an additional magnetic field is applied through the use of Helmholtz coils. Note that only the ion detector was used for the data in this Chapter.

plus tunneling, RIET [99]). The mechanisms behind NSDI of argon are discussed further in Chapter 5.

The experiment was performed with the AS-1 laser, as described in Section 2.3. Ultrashort laser pulses were generated with a Ne-filled hollow-core fiber, producing sub-5 fs pulses with a central wavelength of 750 nm. The pulses were split into two arms by a broadband beamsplitter. Each arm contained a pair of fused silica wedges which were optimized to give the shortest pulse, but remained stationary throughout the experiment. The reflection off the beamsplitter was directed to the phase meter and the transmission was directed to the COLTRIMS, as shown in Fig. 4.5.

Only the ion imaging side of the COLTRIMS apparatus was used in this measurement

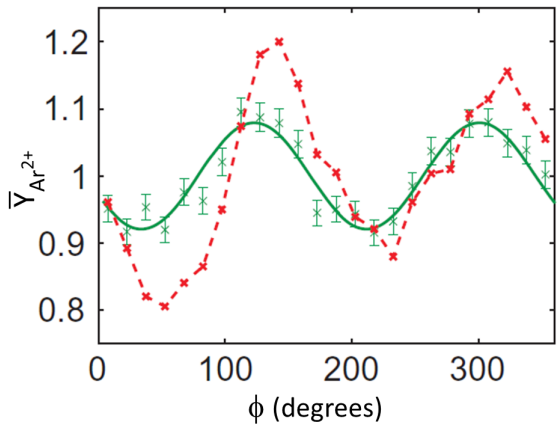

Figure 4.6: Normalized Ar^{2+} yield, $\overline{Y}_{Ar^{2+}}$, as a function of CEP, adapted from Ref. [198]. Red line and crosses are with one reference PAP, while green crosses are with several online reference PAPs (see text), and green line is a sinusoidal fit.

(the COLTRIMS method is described in more detail in Section 2.1). The argon is introduced into the interaction region as a thin supersonic jet. A weak extraction field (about 2.5 V/cm) was applied to the spectrometer for which good momentum resolution (about 0.1 a.u.) was achieved for the Ar^{2+} ions. The ions impinge on a position- and time-sensitive MCP detector with a delay-line anode [130]. These signals are processed by a constant fraction discriminator (CFD) followed by a TDC, which is triggered by the laser pulse detected by a photodiode for readout. The same photodiode triggers the readout of the ADC for the phase meter signals. The resulting yield dependence on CEP is shown in Fig. 4.6.

As there was a bottleneck in the data acquisition that led to dropped signals when trying to process information from every laser shot, a coincidence logic unit was used to keep only the laser shots where an MCP signal was present. The lack of CEP information from every laser shot meant that a reference PAP had to be generated for obtaining the conversion from θ to ϕ. This was done by measuring only the signals from the phase meter for every laser shot for 5-10 minutes before and after the phase-tagged COLTRIMS measurement. The reference PAP measured before and after the data set does not account for changes in the laser parameters throughout the duration of the experiment. Improvements on the method

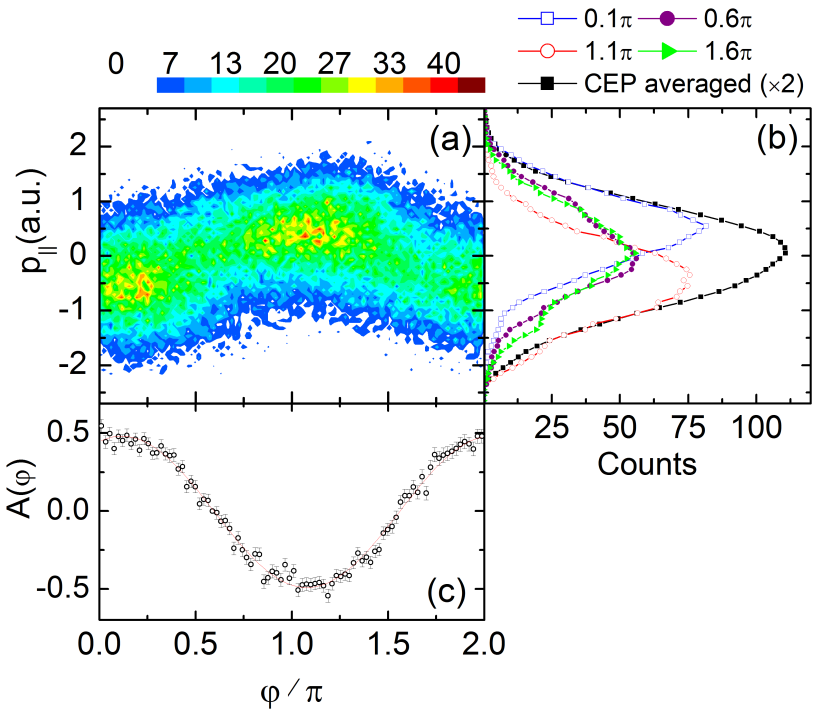

Figure 4.7: Experimental results for NSDI of argon showing (a) the CEP dependence of the Ar^{2+} longitudinal momentum along the laser polarization axis ($p_{||}$), (b) the longitudinal Ar^{2+} momentum spectra for CEP averaged (solid black squares) and four phases as indicated in the legend (integrated within $\pm 0.04\pi$ and averaged over five adjacent $p_{||}$ bins), and (c) the asymmetry parameter, $A(\phi)$, as defined in the text. The error bars denote the statistical error. Adapted from Ref. [99].

have been applied in Ref. [198], where a series of reference PAPs are generated by gating on the ion background signal (*e.g.* any signal that is outside the region of interest), which does not depend on the CEP. This allows for a constant monitoring of the PAP, and even small drifts localized in small increments of the time through the run can be accounted for. The effect of this "running PAP" scheme is shown in green crosses in Fig. 4.6 for which a much smoother trend becomes apparent. Finally, a $\cos 2\phi$ trend becomes clear, which matches the periodicity predicted by Hua and Esry [84].

In our test measurements on the NSDI of argon, we also looked for spatial asymmetries in the longitudinal momentum. The results are shown in Fig. 4.7. The longitudinal momentum for Ar^{2+} is plotted versus the CEP in Fig. 4.7(a). The momentum changes from being mostly

negative to mostly positive as the relative CEP increases from 0 to π. Momentum slices for $\phi = 0.1\pi$, 0.6π, 1.1π, 1.6π and the CEP averaged momentum are shown in Fig. 4.7(b). For $\phi = 0.1\pi$ and 1.1π, the momentum is clearly peaked at non-zero values, while for $\phi = 0.6\pi$ and 1.6π, the momentum is peaked around zero. The asymmetry parameter, considering the full momentum range in Fig. 4.7(a), is shown in Fig. 4.7(c). A high degree of spatial asymmetry is observed with a magnitude of 0.5.

As stated above, NSDI occurs though a recollision process, which necessarily involves more than one electron. This makes it an interesting study in terms of correlated electron dynamics. By measuring the recoil ion, the momentum sum of the two electrons in the continuum is effectively also measured — momentum conservation requires it to be equal in magnitude and opposite in direction — but does not provide any insight on correlated electron motion. In the continuation of this work, the energy sharing of the electrons is studied by measuring the free electrons in coincidence with the Ar^{2+} ion. This is the topic of Section 5.1.

4.2 Phase-Tagged VMI

Although COLTRIMS is a powerful method for measuring physical processes, when the coincidence feature is employed, the count rates are limited to less than one per laser shot. Therefore measuring processes with small probabilities are often impossible or nearly impossible given the current repetition rates of available lasers capable of producing strong fields. Velocity map imaging (VMI) offers a great alternative approach to studying low-probability processes that do not rely on coincidence. In VMI, the target density is limited by space-charge effects and the damage threshold of the detector. Ultimately, this means that the count rate can be, in principle, orders of magnitude higher than in COLTRIMS.

The CEP-tagging technique has also been extended to work with VMI [204]. In VMI, either ions or electrons generated in a localized interaction region are projected onto a two-dimensional MCP detector with a phosphor screen anode, see Fig. 4.8. The glow from the

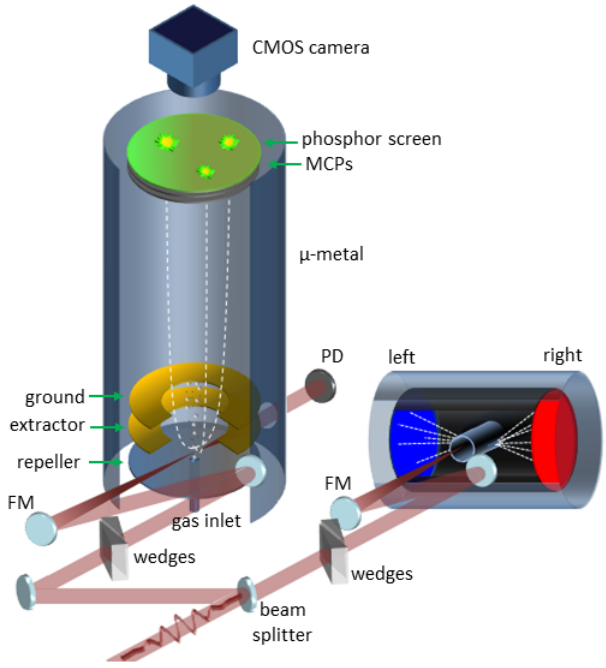

Figure 4.8: Depiction of the phase-tagged VMI experimental setup. A broadband beam splitter (20/80 BS) splits the laser into two arms, each with its own set of glass wedges for residual chirp compensation. The beam transmitted through the BS is focused by a $f = 50\,\text{cm}$ spherical mirror (FM) into the VMI chamber. Ionized electrons are projected onto the MCP/phosphor screen detector by an electrostatic lens. The phosphor glow is recorded by the fast CMOS camera (1 kHz) for every laser shot. The reflected beam off the BS is focused by a $f = 25\,\text{cm}$ spherical mirror into the Stereo-ATI single shot phase meter. Both arms have horizontal polarization. Adapted from Ref. [204].

phosphor is recorded by a camera. The VMI can be operated on a single-shot basis, given that the camera processing time is fast and the phosphor lifetime is short compared to the time between successive laser pulses. In this configuration, the camera is triggered by the laser pulse and records the positions of the fragments generated by a single laser pulse. This is in contrast to the typical VMI mode of operation, for which the camera shutter is open for many laser shots. Otherwise, the concept of VMI is the same as that described in Chapter 7 and Ref. [204].

The fast camera is the key to making single-shot VMI possible. Here, a 1280×1024 pixel complementary metal-oxide semiconductor (CMOS) camera from GSVitec is employed [205].

The CMOS camera can operate up to 1 kHz repetition rate. This also limits the repetition rate of the laser to 1 kHz to allow for single shot measurements. With the single-shot capability of the VMI, it is quite straightforward to phase-tag the signals[3]. Like phase-tagged COLTRIMS (see Section 4.1), laser pulses detected by a photodiode are used to trigger both the VMI camera and the readout of the phase meter. The VMI camera readout is controlled via a Labview program. Therefore, it was necessary to incorporate the phase meter signal processing into Labview as well. This was achieved using a PCI card from Texas Instruments, which acts like the ADC in the phase-tagged COLTRIMS. The CEP of the laser pulse is recovered from the PAP as described in Section 4.1.

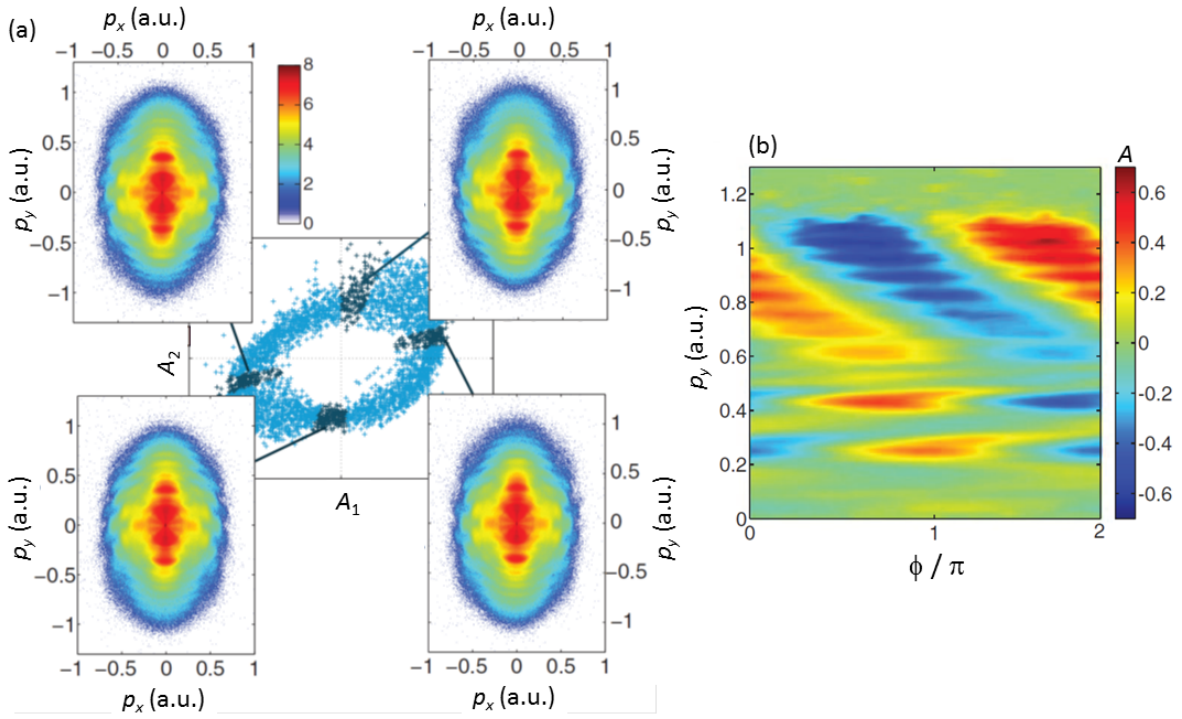

Figure 4.9: (a) Middle: PAP for 5000 free-running laser shots. Outside: non-inverted VMI images for the electrons ionized from Xe by 2.5×10^{13} W/cm^2 laser pulses summed over many laser shots. The images are for four different CE phases over 5×10^4 shots each and their corresponding CEP ranges are highlighted in the PAP. (b) Asymmetry map as a function of momentum along the polarization axis and CEP. Adapted from Ref. [204].

[3]Note that the AS-5 laser at MPQ was used for these studies, which has a repetition rate of 1kHz.

As a test of the phase-tagged single-shot VMI, ATI of xenon was studied. Above threshold ionization of xenon had previously been studied using CEP locked pulses by Kling *et al.* [189]. Like NSDI, ATI can be described by a recollision mechanism. Above threshold ionization occurs when the target absorbs more photons than necessary to overcome the ionization potential and results in peaks that are separated by the photon energy [206]. The raw (non-inverted) signals are shown in Fig. 4.9(a) for four CEP ranges, indicated by the highlighted regions in the PAP, in the middle of the figure. Variations in the spectra along the laser polarization axis (in this case, p_y) are due to the different CEP values. To further illustrate the CEP effect, the spatial asymmetry, A, is plotted as a function of momentum along the polarization axis and CEP in Fig. 4.9(b). Here, the asymmetry values were obtained by integrating over events within an angle of 15 degrees with respect to the p_y axis.

A clear sinusoidal dependence on the CEP is apparent if small longitudinal momentum regions of the asymmetry map [Fig. 4.9(b)] are selected. Each region can be fit by the expected dependence of the asymmetry parameter, $A(\phi) = \alpha \cos(\phi + \phi_0)$ [84], where α is the asymmetry amplitude and ϕ_0 is the phase shift of the asymmetry oscillation with CEP. The highest energy electrons exhibit the highest asymmetry amplitude. The low energy electrons also show a large asymmetry amplitude, as well as a dependence of ϕ_0 on the momentum. This phase-tagged result is consistent with the CEP-locked study by Kling *et al.* [189].

To summarize, in this Chapter, the single-shot stereo-ATI phase tagging method was demonstrated. Phase tagging can be easily extended to other single-shot techniques. In Chapter 6, we use the phase tagging technique to investigate H + H^+ dissociation from an H_2^+ molecular ion beam target measured by coincidence 3D momentum imaging.

Chapter 5

Coherent Control via the Carrier Envelope Phase

One ultimate goal of strong-field ultrafast laser science is to coherently control physical processes [7, 207–209]. The first step in achieving this goal is arguably to understand the dynamics of the involved electrons and nuclei. Exploiting the carrier envelope phase (CEP) of a few-cycle laser pulse has proven to be an effective tool for engineering the dynamics of a system to achieve a desired outcome [210, 211]. The phase tagging technique, described in chapter 4, alleviates the need to lock the CEP of the laser, and allows for studying the physical process in question with all CEP values under the same laser conditions. In this chapter, the phase tagging technique is applied to the study of double ionization of argon atoms, N_2 and NO molecules, and the dissociative ionization of CO and C_2H_2.

5.1 Correlated Electron Motion: Double Ionization of Argon

Double ionization, the process by which two electrons are removed by a strong-field laser, contains rich dynamics. Obviously, two electrons are involved, but what is the level of interaction between them? They could be correlated or anti-correlated, meaning in this context that the electrons are emitted in the same or opposite directions, respectively [43, 94]. The energy sharing between the electrons can be equal or unequal. While many highly-

differential experiments have been carried out to explore the topic [42–44, 212, 213], accurate theoretical support which facilitates interpretation remains a difficult task — as extensions of the single active electron model to describe two electrons is clearly insufficient [214].

Our work on the subject focuses on the non-sequential double ionization (NSDI) of argon atoms [98, 215]. An ultrashort laser pulse was used to liberate two electrons from the atom, which were detected in coincidence with their parent ion using the COLTRIMS technique. Additionally, a semi-classical model was developed to aid the interpretation of the results.

5.1.1 Experiment and Results

At the AS-1 laser (see section 2.3), a COLTRIMS method (see section 2.1) combined with CEP tagging (see section 4.1) was employed to study NSDI of argon. The laser pulses were spectrally broadened by a neon-filled hollow core fiber (see section 2.3.2) to achieve 4 fs duration[1]. The laser beam was split by an 80%/20% broadband beamsplitter, with the strong and weak beams directed and focused into the COLTRIMS and stereo-ATI phase meter, respectively.

In the COLTRIMS, the Ar^{2+} ions and the two ionized electrons associated with it were detected in coincidence. As the two electrons have similar times of flight, the second electron is often lost due to the dead time of the detector. Therefore, to avoid biasing the data, only the first electron recorded in coincidence with an Ar^{2+} was kept for further analysis and the second electron's momentum was calculated, based on momentum conservation. However, to symmetrize the data (*i.e.* determine the zero time and position), the subset of events in which all three particles were detected was used.

The phase meter was used to tag each of the events with the relative CEP of the associated laser pulse. In this way, assuming a Gaussian pulse profile[2], the waveform of the laser pulse is known reasonably well. Therefore, through knowing the CEP of each laser

[1] The pulse duration was measured using multiple techniques, including autocorrelation [141], streaking [216], and the radius of the parametric asymmetry plot [142].

[2] According to streaking measurements, a Gaussian profile is a fairly good assumption.

pulse, despite their few-fs duration, sub-cycle resolution was attained with a few-hundred attosecond precision [98].

The measured "correlated electron maps" are shown in Fig. 5.1, where the yield is plotted as a function of the momentum vector along the polarization axis of the first and second electrons. Due to the indistinguishability of the electrons, the plots are symmetric about the line $p_1 = p_2$. Panel (a) includes all CEP values. It shows a distinct cross shape, centered around the origin (0, 0), indicating that one electron carries the majority of the momentum. This distribution is starkly different than that shown previously by Weber *et al.* [43] for measurements with longer pulses focused to $3.8\times10^{14}\,\mathrm{W/cm^2}$ on helium, where there was a clear momentum correlation pattern (*i.e.* counts appeared in the first and third quadrants in the momentum plot).

The remaining panels of Fig. 5.1 are for CEP bins of 30° size centered at (b) 65°, (c) 155°, (d) 245° and (e) 335°. Depending on the CEP, the counts appear on the upper or lower side of the line $p_1 = -p_2$. For the ϕ bins centered at 155°, and 335°, the signal appears almost exclusively on one side.

5.1.2 Semi-classical Model

A semi-classical description of the NSDI process was developed to gain understanding of the energy sharing. For the intensity used in these studies ($3\times10^{14}\,\mathrm{W/cm^2}$) there are two mechanisms to consider: electron impact ionization (e,2e) and recollision-induced excitation with subsequent ionization (RESI). In (e,2e) a second electron is directly ionized upon impact of the recolliding electron [31]. In RESI, the impact of the recolliding electron excites the parent ion, which is field ionized later in the pulse [217, 218] — as depicted in Fig. 5.2(a).

The experimental data are compared with the model results for single ionization (blue line), and double ionization ((e, 2e)-mechanism (dashed red line) and RESI-mechanism (black line)).

The semiclassical model uses the Ammosov-Delone-Krainov (ADK) tunneling rate, in-

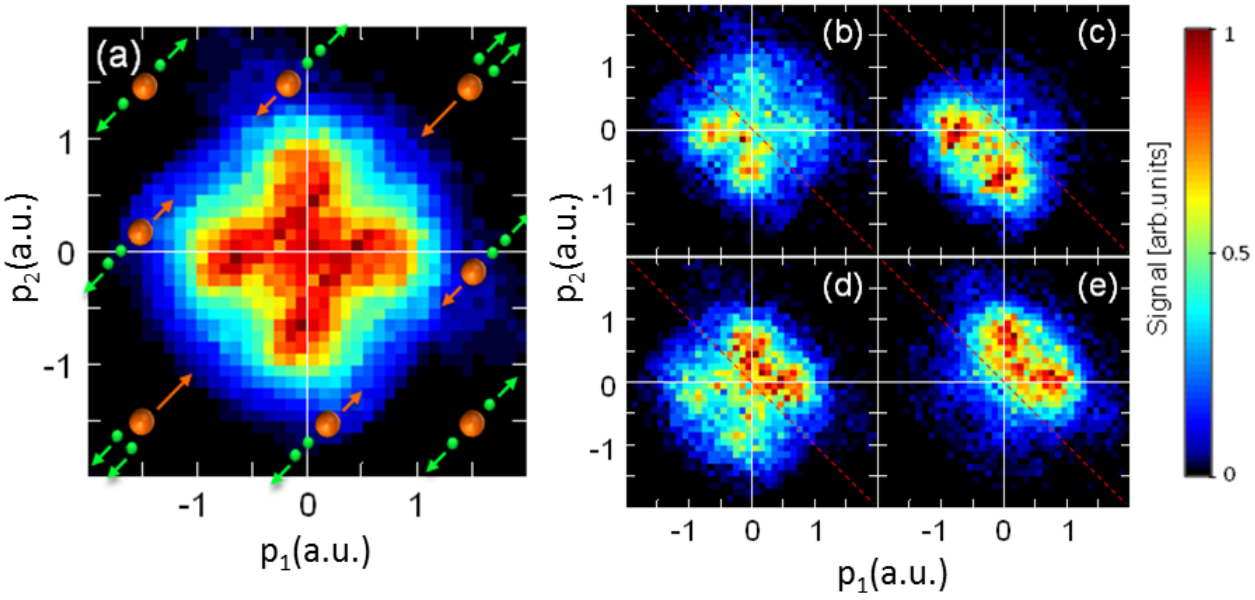

Figure 5.1: Correlated electron map of the longitudinal momentum of the first electron, p_1 and second electron, p_2 for (a) all CEP values and for specific CEP values with a bin size of 30° centered at (b) 65°, (c) 155°, (d) 245° and (e) 335°. In panel (a), the cartoons depict the recoil ion (orange) and the two electrons (green) and the momentum vectors according to where they appear in the plot. Adapted from Ref. [98].

cluding a correction factor to account for over-the-barrier ionization, to calculate the probability for single ionization at any moment within the laser pulse [25]. The propagation of the first ionized electron is treated classically, neglecting the Coulomb interaction with the ionic core and with the other electron. For the trajectories where the electron returns to the Ar^+ parent ion, and the collision occurs with sufficient energy to ionize a second electron, then the second electron is assumed to be liberated via electron impact ionization. Because the second electron is believed to occur at the peak of the electric field, it has zero drift momentum [42]. If, however, the return energy is lower but sufficient to excite the Ar^+, the first excited state is populated. In this scenario, the second electron is liberated by field ionization later in the laser pulse. In both cases, the magnitude of the momentum of the first electron just after the recollision is determined by energy conservation. Meanwhile

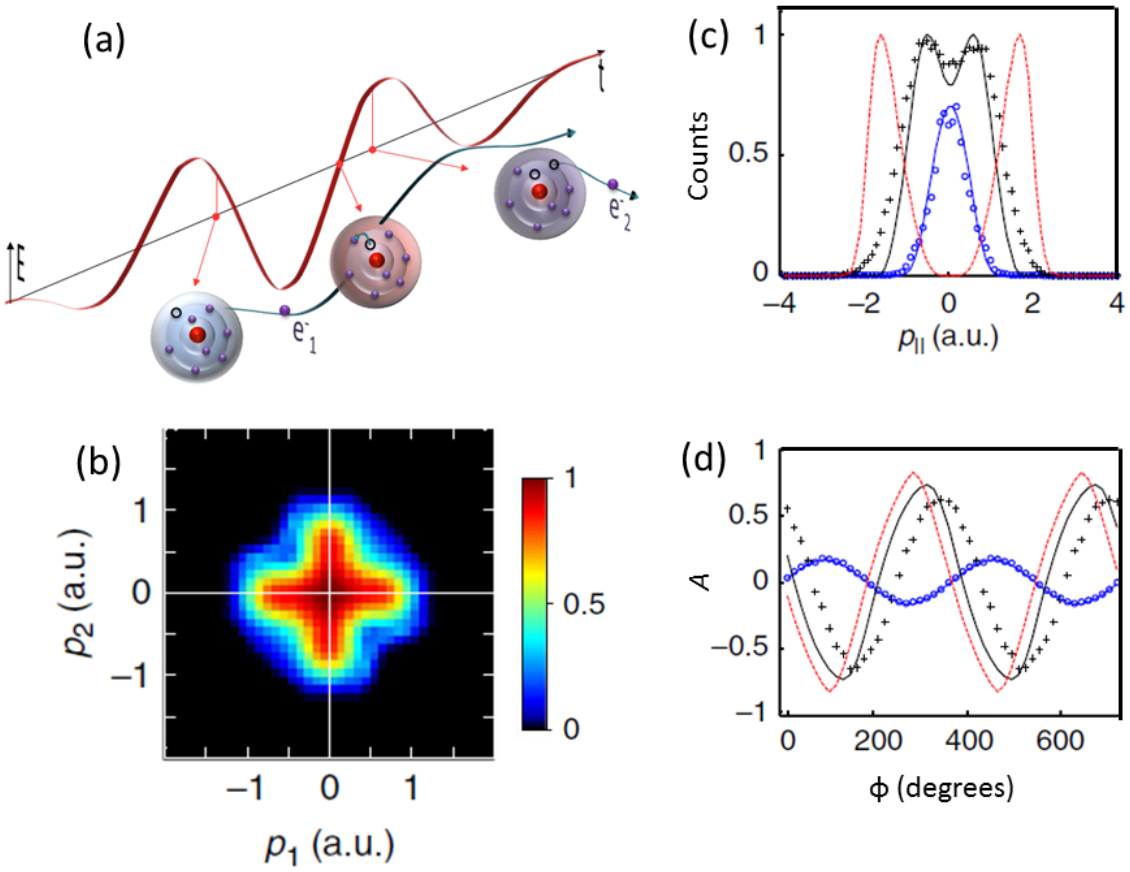

Figure 5.2: (a) Sketch of the RESI mechanism. (b) Correlated electron spectra as resulting from the semi-classical calculation for the RESI process in argon (see text). (c) Comparison of the measured longitudinal recoil ion momentum for Ar^+ (blue circles) and Ar^{2+} (black pluses) with the model results for single ionization (blue line), RESI with $\beta = 20°$ (black solid line) and (e,2e) with $\beta = 0°$ (red dashed line). (d) Comparison of the asymmetry parameter as a function of the CEP with the same legend as in (c). Adapted from Ref. [98].

the direction of the momentum vector is a free parameter, described by the scattering angle β, the angle between the momentum vectors just before and just after the recollision. This is the only free parameter in the model, and it was chosen to be 20° to best fit the measured data. Changing β by 10° only moderately changes the cross-shaped pattern [98]. Very recently, Huang *et al.* [219] used a classical ensemble model to calculate the correlated electron momentum distributions for NSDI of Ar using similar parameters as in our exper-

iment. Their results qualitatively agree with the measured correlated electron momentum spectrum. Furthermore, they kept track of β for each trajectory, and at least for a CEP of 0.6π, the distribution of β peaked exactly at 20°, falling off quickly as the value of β increases or decreases [219].

The experimental and theoretical results for the longitudinal momentum of the Ar^{2+} are shown in Fig. 5.2(c). It is clear that the RESI model fits the experimental data more closely than the (e,2e) model. Furthermore the asymmetry parameter A, plotted in panel (d), also fits the RESI predictions better. Here the asymmetry parameter is defined as

$$A = (N_+ - N_-)/(N_+ + N_-), \tag{5.1}$$

and $N_\pm$ denote the number of ions with positive and negative momentum along the polarization axis. Figure 5.2(d) shows the comparison of A for the two models and the measurement for both Ar^+ and Ar^{2+}. The ϕ-offset is determined by shifting the CEP axes such that the experimental A for Ar^+ and the theory match, as the periodicity and amplitude between theory and experiment in this case, agree quite well. Specifically, both the amplitude of the asymmetry and the periodicity appear to be well described by the model.

For the Ar^{2+}, the asymmetry amplitudes for both processes are in fair agreement with the experiment. However, the calculated phase shift between the Ar^+ and the Ar^{2+} asymmetry curves (154° for RESI and 177° for (e,2e)) do not match the measured phase shift of 114°. Nevertheless, the level of agreement is quite good, considering the simplicity of the model. Taking the RESI simulation one step further, the correlated electron pictures can be compared, as shown in Fig. 5.3 for the CEP values where the maximum Ar^{2+} asymmetry is observed [panels (a) – (c)], and where the Ar^{2+} asymmetry is equal to zero [panels (d) – (f)]. Again, the calculated and experimental results resemble each other, with only small differences between them.

In panels (c) and (f) of Fig. 5.3, the calculated first (green-shaded area) and second ionization (red-shaded area) rates for the RESI process are plotted on the same time scale as the electric field of the laser for the same CEP values as the other panels. Perhaps the

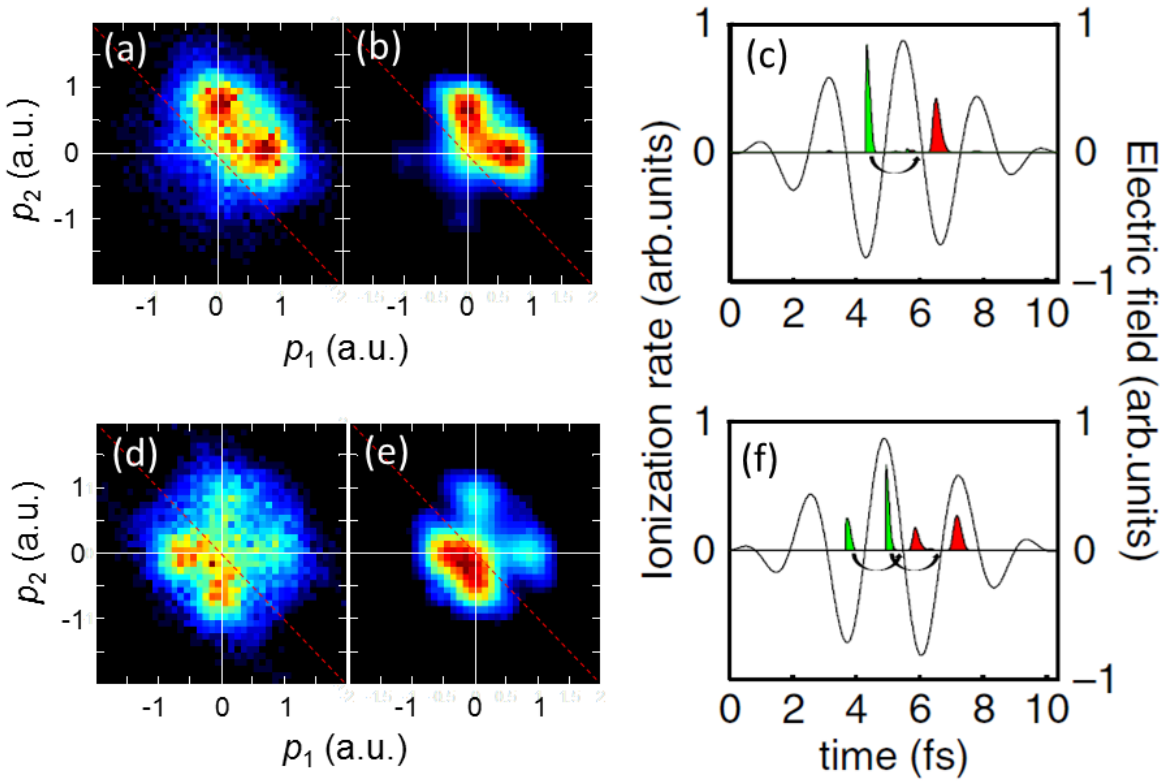

Figure 5.3: Timing of the first and second ionization of argon. Comparison of measured (a, d) and calculated (b, e) two-electron momentum distributions for CEP values corresponding to a maximum (a, b) and zero value (d, e) of the Ar^{2+} asymmetry. The predicted ionization rates of the first (green-shaded area) and second (red-shaded area) electron contributing to NSDI are displayed in (c) and (f) together with the electric field of the laser pulse (black line) for maximum and zero Ar^{2+} asymmetry parameters, respectively. Each black arrow points to the time of recollision for electrons liberated near the tail of the arrow. In (a, b, c) only a single recollision leads to NSDI, while in (d, e, f) two recollision events in successive half-cycles contribute. Adapted from Ref. [98].

most striking feature about these plots is that, for certain CEP values, there is only a single recollision. Furthermore, the time of release for the second electron occurs well before the next maximum of the laser electric field. Adopting the idea that the infrared field can be viewed as an inherent clock [220], the most likely time of ionization of the second electron

after the recollision can be retrieved from $\Delta t = \cos^{-1}(p_0/p_{max})/\omega$, where p_0 and p_{max} are the most probable and the maximum momentum of the second electron, respectively. Carrying out this analysis on the experimental data, it was found that $\Delta t = 430 \pm 40$ attoseconds, which corresponds to 210 ± 40 attoseconds before the next peak of the laser field following the recollisional excitation. The same analysis carried out for the RESI simulations, predicts the second ionization takes place about 230 attoseconds before the next field maximum. This finding is in contrast to the previously assumed case that the second ionization occurs at a field maximum [42].

The finding that the second electron is ionized before the laser electric field reaches its next maximum suggests that the excited Ar^+ population is depleted. Thus the unequal energy sharing of the two electrons can be assigned as the follows: the first electron has momentum close to zero and the second electron takes on a range of momentum, which varies as a function of the CEP. This, again, is not in accordance with the previously assumed case for RESI, where the ionization occurs at an electric field maximum — where the vector potential is zero — which would give rise to the second electron having momentum close to zero [42].

5.1.3 Conclusions

In conclusion, new insight into the NSDI process was achieved by drastically limiting the number of recollision events through the use of near single cycle laser pulses. In contrast to previous work with longer (multi-cycle) laser pulses [43, 212], a cross-shaped pattern was observed in the correlated two-electron momentum spectrum. Through the assistance of semi-classical calculations, RESI was identified as the underlying NSDI mechanism, and the timing of the release of the second electron was determined. The development of more accurate two-electron theories is needed for rigorous testing of the observed correlated electron dynamics.

5.2 CEP Control of Molecular Processes

Molecules are inherently different from atoms in that their electronic structure depends on the distances between the nuclei. Thus studying molecules tends to reveal rich nuclear dynamics, in addition to their electronic dynamics. The rest of this chapter discusses CEP effects in molecular targets. Firstly, the non-dissociative double ionization of N_2 is studied in the NSDI regime and compared to the NSDI of argon. Next, dissociative ionization processes of CO and C_2H_2 (preliminary) are investigated. Finally, NO is exposed to elliptically polarized ultrashort pulses to explore the effects of the transverse laser field component on double ionization.

5.2.1 Nitrogen

Nitrogen ($I_P^{\mathrm{I}} = 15.58$ eV and $I_P^{\mathrm{II}} = 27.12$ eV), having very similar first and second ionization potentials to argon ($I_P^{\mathrm{I}} = 15.76$ eV and $I_P^{\mathrm{II}} = 27.63$ eV), provides an example for extending the NSDI studies to molecules, while being able to compare them to the acquired knowledge of previous studies on atoms. Many studies have shown that the behavior of N_2 and argon, in particular for NSDI, exhibit similarities [221–225]. However, these studies used pulse durations where multiple recollisions can occur, obscuring the interpretation. In section 5.1 and Ref. [98] it was shown that using ultrashort pulses approaching the single-cycle regime leads to dramatically different electron correlation spectra, where the energy is unequally shared between the two electrons, leading to a cross-shaped pattern.

Previous studies by Eremina *et al.* using 35 fs laser pulses, centered at 800 nm, and intensities in the NSDI regime, showed momentum correlations in the emission of two electrons from N_2 [212] and argon [44]. This manifested as contributions to the first and third quadrants of the electron correlation "map", that is, the electron yield plotted as a function of the momentum along the laser polarization of the first and second electrons. This indicates that the energy is shared equally between the electrons, and they are emitted into the same half-sphere. A smaller contribution of the signal appeared in the second and forth

quadrants — indicating the electrons were emitted in opposite directions, often referred to as "anticorrelation." In a pump-probe study, Zeidler *et al.* demonstrated that the portion of anticorrelated electrons can be controlled to some extent via the molecular alignment [226].

Using the phase-tagged COLTRIMS technique (see section 4.1 and Ref. [99]) and ultrashort laser pulses of 4 fs duration at the AS-1 (see section 2.3), we performed a comparative study of NSDI for Ar and N_2 [215]. To ensure that both targets were exposed to the same laser conditions, they were alternately let into the COLTRIMS jet in about 25 minute intervals. As NSDI was desired to be the main process for both targets, a peak intensity of $3.6\times10^{14}\,\mathrm{W/cm^2}$ was chosen. The results are shown in Fig. 5.4. The resulting CEP averaged longitudinal momenta for these ions are shown in Fig. 5.4(d). The spectra for the Ar^{2+} and N_2^{2+} closely resemble each other, the only difference being that for N_2^{2+} the dip at $p_{||}=0$ is less pronounced. The CEP dependence of the longitudinal momentum is shown in Fig. 5.4 for Ar^{2+} [in panel (a)] and N_2^{2+} [in panel (b)]. The "islands" in the N_2^{2+} spectrum extend slightly more towards smaller momentum values than the Ar^{2+} islands do.

The semi-classical model for the RESI mechanism for argon, described in section 5.1.2 and Refs. [98, 215], was utilized to help interpret both the Ar^{2+} and N_2^{2+} results. The calculated longitudinal momenta for Ar^+ and Ar^{2+} are shown in Fig. 5.4(d), and the CEP-resolved momentum for Ar^{2+} is shown in Fig. 5.4(c). As the ϕ offset is experimentally unknown, the CEP axes were shifted to match the theory for the Ar^+. While the simulation qualitatively reproduces the experimental result, the measured Ar^{2+} momentum distribution extends to somewhat higher momenta than in its calculated counterpart. This is probably due to small contributions from higher excited states of Ar^+ that are neglected in the model — as the higher excited states might undergo (e,2e) which would result in higher momentum [42].

To study the electron spectra, each target was measured individually with an intensity of $3.2\times10^{14}\,\mathrm{W/cm^2}$. The correlated electron momenta spectra are shown in Fig. 5.5 for Ar^{2+}, N_2^{2+} and the semi-classical model predictions for the argon dication. The spectra including

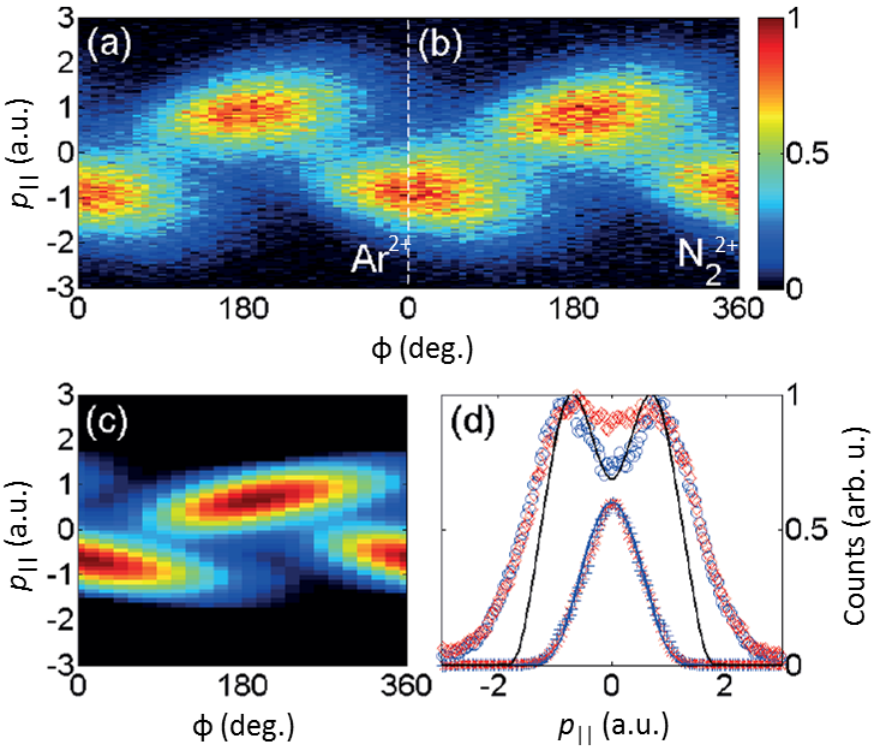

Figure 5.4: Measured yield as a function of $p_{||}$ and CEP (a) Ar^{2+} and (b) N_2^{2+}, from exposure to a peak laser intensity of 3.6×10^{14} W/cm^2. (c) Calculated CEP-dependent $p_{||}$ distributions of Ar^{2+} using the semi-classical model (see text). (d) Measured momentum spectra of Ar^+ (blue pluses), N_2^+ (red crosses), Ar^{2+} (blue circles), N_2^{2+} (red diamonds), averaged over CEP, shown together with predictions for Ar^+ (blue solid line) and Ar^{2+} (black solid line). The maxima of the doubly-charged ion spectra are normalized to 1 and the spectra of the singly-charged ions are normalized to 0.6 for visualization. Adapted from Ref. [198].

all CEP values appear in the first column. All three spectra exhibit a cross-like pattern indicating one electron has momentum close to zero, while the other electron's momentum is changing. The second through fifth columns are for CEP slices around 135°, 225°, 0°, and 90°, each having a width of 45°. Here, again, it can be seen that all three series of spectra exhibit qualitatively the same features. Perhaps the only noteworthy difference is the appearance of a small contribution of low-energy anticorrelated electrons in the N_2^{2+} spectrum — which is responsible for the greater contribution close to $p_{||}=0$ in the dication spectrum N_2^{2+} (see panels (a) and (c) in Fig.5.5).

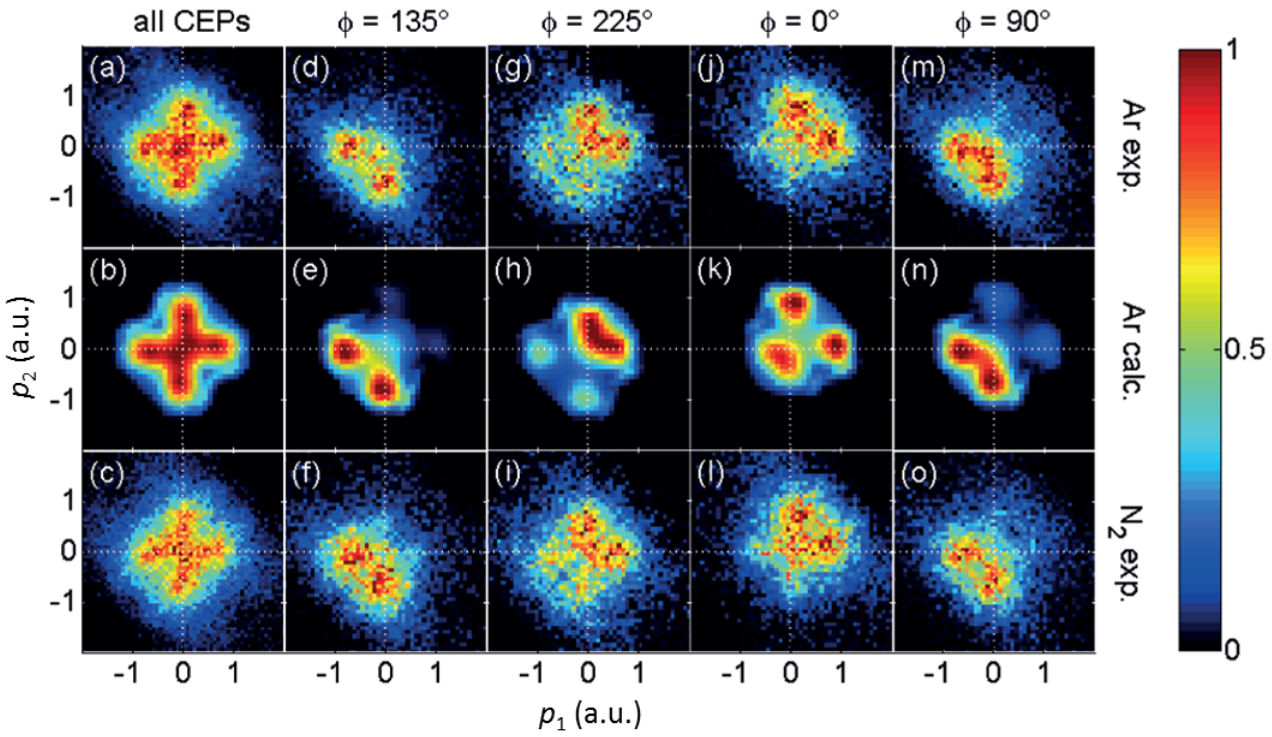

Figure 5.5: Experimental two-electron momentum distributions, showing the correlated momenta along the laser polarization axis of the first (p_1) and second (p_2) electron emitted from Ar^{2+} (top row) or N_2^{2+} (bottom row), and the corresponding predictions for argon (central row) at the peak intensity of $3.2\times10^{14}\,\mathrm{W/cm^2}$. The left column (a, b, c) displays the CEP-averaged results. In the second (d, e, f), third (g, h, i), fourth (j, k, l) and fifth (m, n, o) columns, the correlation spectra are shown for CEP values of 135°, 225°, 0°, and 90°, respectively. Each image is averaged over a CEP range of 45°, symmetrized with respect to the $p_2 = p_1$ diagonal (since the electrons are not distinguishable) and normalized to have the color scale peak at 1. Adapted from Ref. [198].

The origin of the small contribution of anticorrelated electrons in the NSDI of N_2 is the excited states of N_2^+, which are energetically lower than the first excited state of Ar^+. While the low energy excited states can also be populated in the collision with the returning electron, their contribution to the NSDI is small, as the tunneling probability rapidly decreases for lower excited states. A test calculation, using fictitious states with energies ranging from 7.5 to 13.5 eV, showed that for the small portion contributing to the NSDI signal, these low lying states manifest as anti-correlated electrons.

While for Ar and N_2 targets NSDI appears to generally behave in the same way, it is not clear that this trend would carry over to other atom/molecule pairs with similar ionization potentials, such as Xe and O_2. The excited state structure seems to play a role. Therefore, if differences were observed for other atom/molecule pairs, it could be due to their excited state structure.

5.2.2 Nitric Oxide

Nitric oxide, in contrast to Ar and N_2 (discussed before), has a very low first ionization potential of 9.25 eV. And, NO's second ionization potential is 30.3 eV [176], about 3 eV higher than for Ar and N_2. This somewhat complicates the first and third steps of the 3-step model for recollision, as the first electron can be tunnel ionized early in the pulse and it needs substantial recollision energy to ionize a second electron [227]. Therefore, it is an interesting target for further NSDI studies. Some doubly ionized NO molecules will dissociate, like the other molecules mentioned in this section, however, for our first experiments the dissociating molecules are not considered.[3]

Using sub-5 fs pulses generated through spectral broadening of an argon-filled HCF at the LMU (see section 2.3), double ionization of NO was studied with mid-10^{14} W/cm^2 intensities with a phase-tagged COLTRIMS technique (see sections 2.1 and 4.1). The part of the laser beam that was sent to the stereo-ATI phase meter, in order to tag the CEP, had linear polarization. In the laser beam path to the COLTRIMS, a broadband quarter-wave plate was utilized to vary the electric field ellipticity, while a broadband half-wave plate was used to keep the major ellipse axis along the TOF axis of the COLTRIMS spectrometer (the dimension with the highest resolution). An example of an elliptically polarized pulse is shown in Fig. 5.6(f). In order to compare between different ellipticities, the electric-field strength for the major axis was kept approximately constant.

[3] A high voltage is needed on the spectrometer to measure the large KER's, while a low voltage is needed to get good momentum resolution for the NO^{2+}. With the low voltage setting, most of the dissociated fragments are lost.

The yield of the doubly charged ion is plotted as a function of the momentum along the laser polarization, $p_{||}$, and the CEP of the laser pulses, shown in Fig. 5.6(a–e). Panels (a) and (b) are for argon at an intensity of $4.5\times10^{14}\,\mathrm{W/cm^2}$ with ellipticity $\epsilon = 0$ (linear) and 0.18, respectively. For the linear case, the sign and magnitude of $p_{||}$ is modulated by the CEP. Meanwhile, for $\epsilon = 0.18$, the modulation is nearly gone due to the presence of a small transverse component of the electric field. Measuring the momentum of the Ar^{2+} is equivalent to measuring the sum of the momenta of the two electrons due to momentum conservation. Thus, the dynamics of the electrons must be changing in order to account for the differences in the ion momentum. Nevertheless, based on the previous observations on other targets (Ar, N_2, C_2H_2), the modulation of the dication $p_{||}$ with CEP is very likely due to NSDI.

Guo and Gibson carried out studies on the double and single ionization of NO with 30 fs 800 nm laser pulses, with circular and linear polarization [228]. By plotting the NO^{2+}/NO^{+} ratio as a function of intensity, the so-called knee, which is a strong indicator of NSDI, appears for both polarizations. Guo and Gibson suggested, however, that recollision did not play a role in the formation of the knee structure with circular polarization. In fact, it is common practice to use circular polarization when one wishes to suppress the recollision [41].

The results of our phase-tagged momentum measurements on NO for $\epsilon = 0$, 0.18, and 0.25 are shown in Fig. 5.6(c–d) for an intensity of $1.5\times10^{14}\,\mathrm{W/cm^2}$ along the major axis. It turns out, that for linear polarization, the NO^{2+} momentum behaves similarly to that for Ar^{2+} — the momentum is strongly modulated by the CEP of the laser pulse. However, in contrast to Ar, as the ellipticity is increased to 0.18, the modulation with CEP persists. Even for an ellipticity of 0.25, the modulation is still rather strong. Preliminary analysis for higher ellipticities suggests that NSDI is still present.

Classical trajectory calculations by Wang and Eberly have shown that electrons which follow elliptical paths, as is the case for elliptical polarization, can recollide with the parent

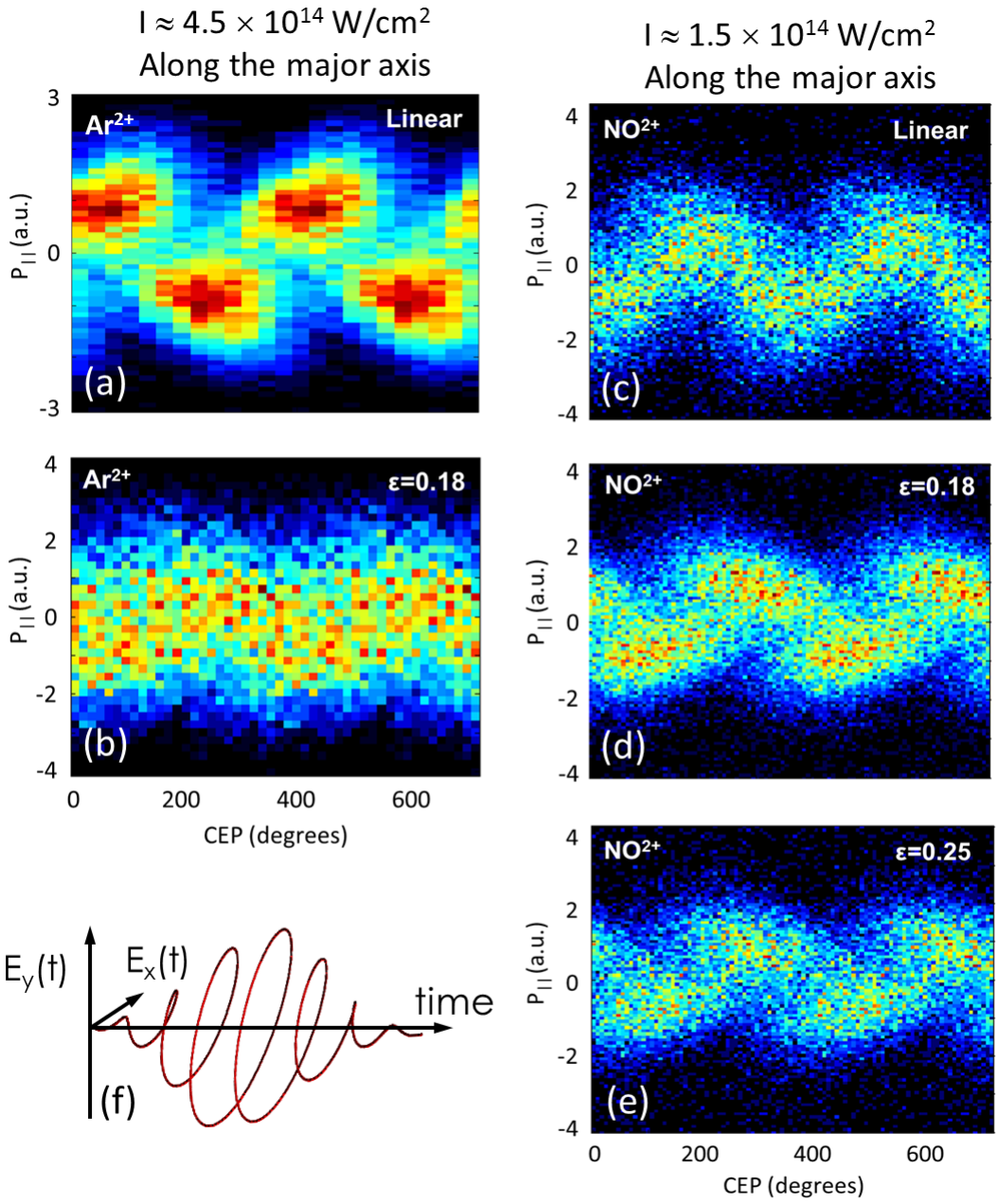

Figure 5.6: Yield as a function of the longitudinal momentum along the major axis of the polarization, $p_{||}$, and CEP for (a) Ar^{2+}, with linear polarization (b) Ar^{2+}, with an ϵ=0.18 polarization, (c) NO^{2+} with linear polarization, (d) NO^{2+} with ϵ=0.18, and (e) NO^{2+} with ϵ=0.25 (f) illustration of the electric field vector for an elliptical pulse.

ion [229]. Similarly, Fu *et al.* conducted semi-classical calculations on atoms suggesting that with circular polarization, NSDI occurs through chaotic trajectories [230]. Fu *et al.* suggested that it is more likely to get NSDI for targets with first ionization potentials below about 11 eV (at 800 nm wavelengths). Recall that for NO, $I_p^{\mathrm{I}} = 9.25\,\mathrm{eV}$. Furthermore, very recent classical calculations by Kamor *et al.* suggest that recollision does, indeed, play a role in the double ionization of NO [95].

5.2.3 Carbon Monoxide

The CO molecule provides an interesting target for studying dissociative ionization by a strong laser field [116, 117, 231]. When a molecule is dissociated, there are several processes for which the CEP can play the role of a control knob, including: ionization, recollisional excitation, and laser-induced population transfer between excited electronic states [116]. Znakovskaya *et al.* [116] studied CO with 4 fs laser pulses, using VMI. The authors monitored the C^+ fragment emission as a function of the CEP for the (1,0)[4] channel and found a spatial asymmetry amplitude of 0.2. However, identifying the process responsible for the CEP control was not possible within the scope of their experiment.

Using the COLTRIMS coincidence technique, Liu *et al.* investigated the directional emission of the ionic fragments from higher charge states of CO [117]. They found spatial asymmetry amplitudes of 0.05 and 0.02 for the C^{2+} fragments from the (2,0) and (2,1) channels, respectively, with a 180° phase shift between them for a 50° cone around the laser polarization. The authors suggested that the processes generating the two outcomes were different in nature. Namely, recollisional excitation leads to (2,0) and recollisional ionization leads to (2,1) for their laser conditions (4.2 fs, 740 nm CEP-stabilized pulses at an intensity of $6\times10^{14}\,\mathrm{W/cm^2}$).

Using the phase-tagged COLTRIMS experimental approach, we also studied the dissociative ionization of CO [118]. With sub-5 fs, 750 nm pulses at a peak intensity of $1.2\times10^{15}\,\mathrm{W/cm^2}$, the same C^{2+} channels as in Ref. [117] were observed. However, the

[4]The same notation as used in Chapter 3 will be used throughout this section.

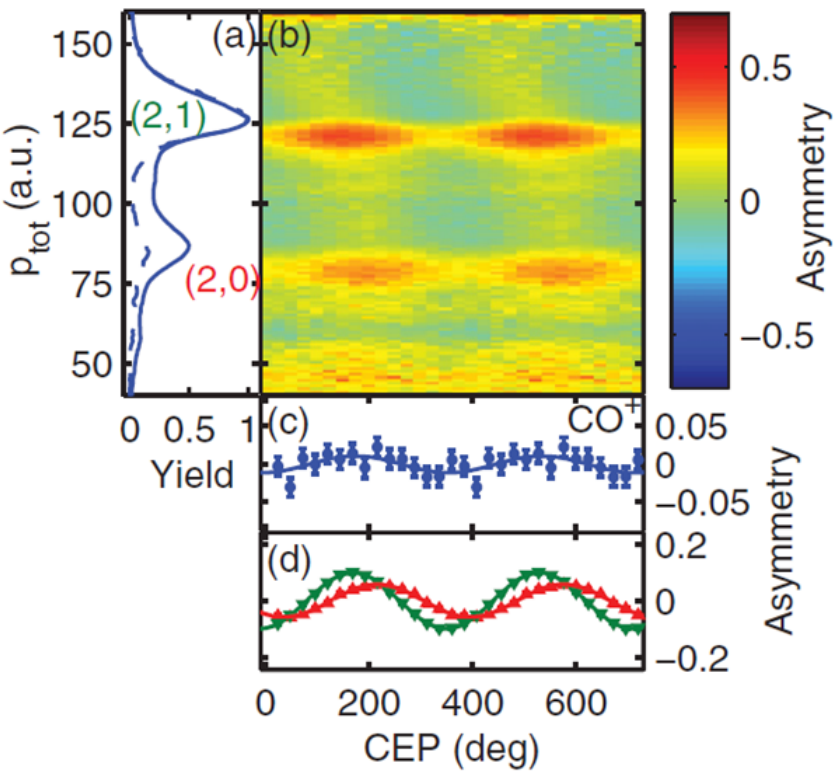

Figure 5.7: Asymmetry of the C^{2+} ion emission at a peak intensity of 1.2×10^{15} W/cm^2. (a) Total momentum spectra of all C^{2+} ions (solid curve) and of C^{2+} ions coincidence filtered for the (2,1) channel (dashed curve). (b) Asymmetry of the C^{2+} ion emission. Note that the asymmetry parameter does not oscillate around zero for all values of p_{tot} due to losses on the detector from localized areas with low efficiency. (c) Asymmetry of the CO^+ ion with statistical error bars. (d) Asymmetry of the (2,0) channel (red upward triangles) and (2,1) channel (green downward triangles), integrated over the ranges $p_{tot} = 70-90$ a.u. and $p_{tot} = 110-130$ a.u., respectively. The asymmetry parameters in (c) and (d) have been shifted to oscillate around zero. Adapted from Ref. [118].

observed phase shift between the (2,0) and (2,1) channels was significantly different than reported in Ref. [117]. The total momentum, p_{tot}, distribution for all of the C^{2+} fragments is shown in Fig. 5.7(a), along with the coincidence filtered C^{2+} fragments from the (2,1) channel. The (2,0) and (2,1) channels are well separated in momentum, allowing for their identification and individual analysis, despite not being able to measure neutrals. The asymmetry map for all C^{2+} fragments is shown in Fig. 5.7(b). A slight phase shift between the

(2,0) and (2,1) channels is visible. In Fig. 5.7(d), the C^{2+} asymmetry for the (2,0) and (2,1) channels is shown, revealing a maximum phase shift of 48°. These results are drastically different than in Ref. [117], where a 180° phase shift was observed for laser pulses with about half of the peak intensity. Furthermore, the asymmetry amplitudes are higher than observed in Ref. [117] — 0.06 for the (2,0) channel and 0.1 for the (2,1) channel.

Another similar measurement on CO at an intensity of $3.5\times10^{14}\,\mathrm{W/cm^2}$ (*i.e.* lower than in Ref. [117]), allowed for a more detailed investigation of the dissociative single ionization channels, namely (1,0) and (0,1). The (1,1) coincidence filtered (dashed line) and total momentum spectra for the C^+ and O^+ ions are shown in Fig. 5.8(a) and (c), respectively. The corresponding asymmetry maps for all C^+ and O^+ are shown in Fig. 5.8(b) and (d).

For both intensities, the asymmetry of the CO^+ ions is used as a reference (shown in Figs. 5.7(c) and 5.8(e)), as it is collected simultaneously with the fragmentation data. The C^+ fragments tend to be closer in phase to the CO^+, while the O^+ fragments tend to be approximately 180 degrees out of phase with the CO^+. Furthermore, for all observed channels, the C^{q+} fragments tend to be emitted into the same direction along the laser polarization with only small phase shifts between the different channels.

In light of these differences to the work by Liu et al. [117], we offer another explanation for our findings. Specifically, the initial ionization step is more likely to be the cause for the observed CEP dependence. This stems from the observation that the asymmetry dependence for all C^{q+} and the CO^+ are similar [118].

5.2.4 Acetylene

Small hydrocarbons have been shown to undergo hydrogen migration where hydrogen atoms or protons migrate from one site to another within a molecule [232–236]. One question, within the scope of this chapter, is: can hydrogen migration be controlled by CEP? To begin answering this question, the acetylene molecule is investigated with an intense 4 fs laser pulse, as acetylene has previously been shown to undergo bond rearrangement to the

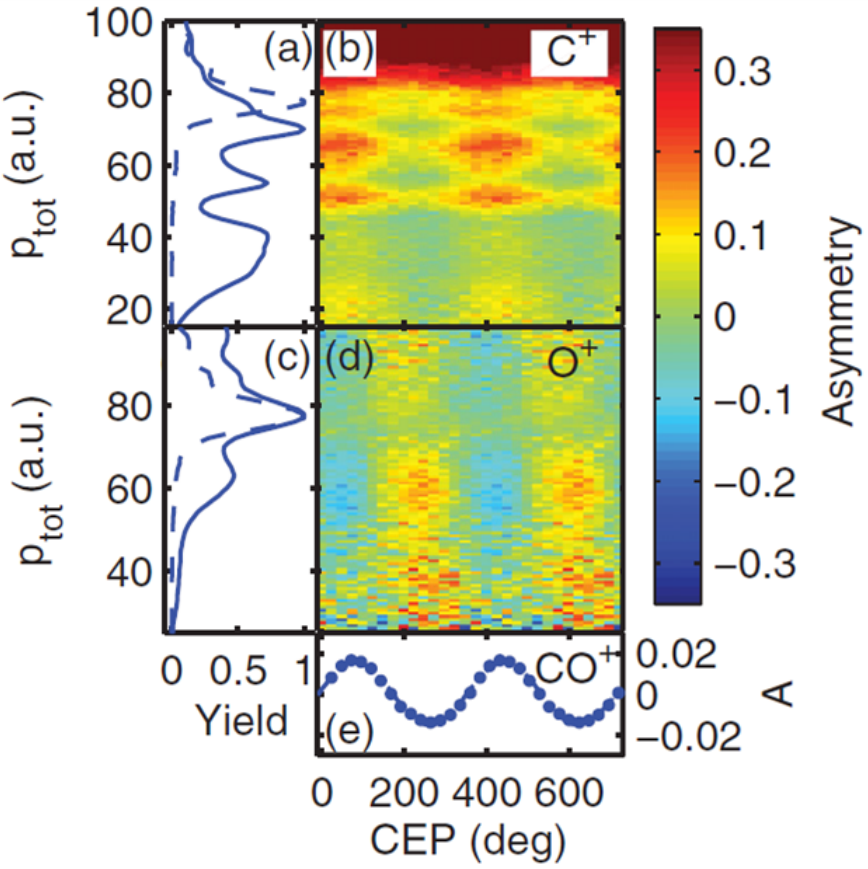

Figure 5.8: The total momentum spectra of all (a) C^+ and (c) O^+ ions (solid curves) and the coincidence-filtered momentum spectra for the ions from the $C^+ + O^+$ channel (dashed curves). Asymmetry maps, for (b) C^+ and (d) O^+ ions at an intensity of 3.5×10^{14} W/cm^2. Panel (e) shows the asymmetry in the CO^+ ion. Adapted from Ref. [118].

vinylidene configuration in the presence of a strong laser field [236–238].

Recently yield modulations as a function of CEP were reported for select dissociative ionization channels of small hydrocarbons by Xie *et al.* [119]. The authors suggested that the observed CEP dependence is due to a recollision mechanism. In particular, for acetylene, they studied the $CH^+ + CH^+$ and $H^+ + CH_2^+$ break up channels and the singly and doubly charged molecular ions. The singly and doubly charged molecular ions did not exhibit a yield dependence on the CEP, but their momentum along the laser polarization did exhibit a modulation in sign and magnitude which varied with the CEP.

Using 4 fs, (740 nm central wavelength) pulses generated through spectral broadening in an argon-filled HCF at the LMU (see section 2.3), double ionization of C_2H_2 was studied at 2.8×10^{14} W/cm^2 intensity using a phase-tagged COLTRIMS technique (see section 4.1) [120]. The longitudinal momentum, $p_{||}$, distribution of the $C_2H_2^{2+}$ dication is shown in Fig. 5.9(b), and the CEP dependence is shown in Fig. 5.9(a). A clear modulation of $p_{||}$ with the CEP is visible.

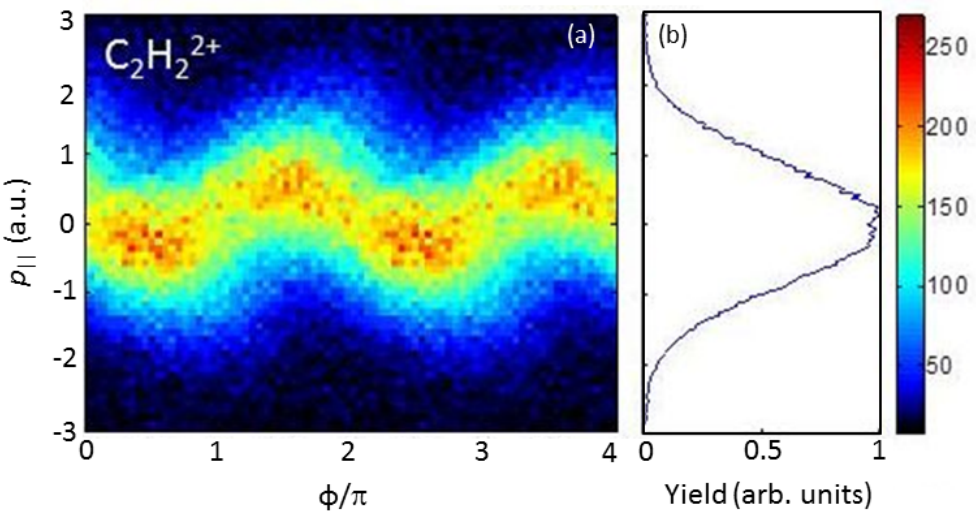

Figure 5.9: (a) Yield as a function of longitudinal recoil momentum, $p_{||}$, and CEP, ϕ, for 4 fs pulses at an intensity of 2.8×10^{14} W/cm^2 for $C_2H_2^{2+}$. The full range of the spectrum, which goes from 0 to 2π, is duplicated and plotted as 2 to 4π for visualization. (b) The corresponding CEP-integrated momenta. Adapted from Ref. [120].

The CEP dependence is most likely due to an electron recollision process, where the first ionized electron is guided by the laser field to collide with the parent ion. For certain CEP values the electron carries sufficient energy to further ionize the parent $C_2H_2^+$ ion. The recoil felt by the ejection of the two electrons offsets the dication momentum from zero, and varies with CEP, similar to the previous findings for NSDI of argon and N_2 (see sections 5.1 and 5.2.1 and Refs. [98, 215]).

The COLTRIMS coincidence technique allows for the break-up channels $C^+ + CH_2^+$, cor-

responding to the vinylidene configuration, and $CH^+ + CH^+$, corresponding to the acetylene configuration, to be distinguished from one another. Preliminary analysis suggests a CEP dependence of these channels, and further analysis is underway.

In summary, in this Chapter, our studies on the coherent control via the CEP using the phase-tagged COLTRIMS technique are outlined. This work includes the double ionization of Ar, N_2, and NO, as well as for the dissociative ionization of CO and C_2H_2 (preliminary). For argon and N_2 the RESI mechanism leading to NSDI plays a large role at the intensities studied. A recollision process also seems to play a role in the double ionization of C_2H_2. Further analysis and experiments are underway to explore the NSDI of NO in ellipically polarized pulses, and the dissociation dynamics, including hydrogen migration, in acetylene.

Chapter 6

CEP Control of Pathway Interference in H_2^+ Dissociation

This Chapter is based on Ref. [110], where phase tagging (see Chapter 4) is applied to the laser-induced molecular dissociation imaging (LIMDI) method (see Section 2.2) for an H_2^+ molecular-ion beam. With the ultimate goal of coherently controlling dissociative reactions [7, 207, 209], this work aims at understanding the control mechanisms and reaction pathways for dissociation into $H^+ + H$. Tailoring the electric field waveform, through varying the carrier-envelope phase (CEP), of few-cycle laser pulses has proven to be a powerful tool to control dynamics of electrons and nuclei [208, 210, 211]. The first direct observation of the CEP playing a role in strong field laser interaction with atoms was accomplished by Paulus *et al.* [196], just over a decade ago. Since then, CEP studies have been undertaken for the dissociative ionization of H_2 and its isotopologues [45, 88, 121, 122, 188, 189] and has recently been extended to more complex diatomic molecules, such as CO [116–118], and to small polyatomic molecules [119, 120, 239]. While these experimental studies have led to great insights for CEP control mechanisms, (near) exact theory — which could provide predictive power and reveal general trends — is so far impossible, due to the stark complexity of the problem. A solution to this conundrum is to study the molecular ion target, H_2^+, which can be solved with near-exact theory [83]. This creates a need for experiments on H_2^+ molecular ion beam targets, where the CEP of the laser pulse is known.

6.1 Previous Work

The electric field of a laser pulse is commonly defined by $E(t) = \varepsilon(t)\cos(\omega t + \phi)$, where $\varepsilon(t)$ is the envelope, ω is the carrier frequency, and ϕ is the CEP. For an ultrashort laser pulse, varying ϕ leads to drastically different electric-field waveforms (see Fig. 4.1). Carrier-envelope phase control over H_2^+ dissociation was first proposed theoretically by Roudnev *et al.* [85, 240]. Despite the theory being available for nearly a decade, the difficulty imposed by the constraints of the experiment has so far prevented this benchmark measurement. Any laser experiment on a molecular-ion beam is challenging due to the low target density. Adding the additional constraints of a CEP-stabilized laser rendered the experiments close to impossible, as the amount of time the CEP could be locked was typically less than an hour, while to collect sufficient statistics, the experiment needed an estimated run time of >24 hours[1]. Therefore, the first experiments on H_2^+ were carried out on the neutral H_2 target, where the H_2^+ was produced by the same laser pulse [45, 189].

For example, Kling *et al.* used 5 fs, 1.2×10^{14} W/cm^2 pulses with stabilized CEP to dissociatively ionize D_2 and found asymmetries in the emission direction of D^+ ions for kinetic energy releases (KER) above 6 eV [45, 189]. The diminished dissociation signal in a circularly polarized laser field indicated that electron recollision played a role. Recollision entails a tunnel-ionized electron undergoing a collision with its parent ion after acceleration by the oscillating laser field [31, 33]. The authors suggested that the energy exchange between the laser-driven electron and the parent ion can promote the D_2^+ to the $2p\sigma_u$ excited state. The coupling of this $2p\sigma_u$ state and the $1s\sigma_g$ ground state [83] on the trailing edge of the laser pulse during the dissociation of D_2^+ was the proposed mechanism for the observed CEP-dependent asymmetry [45, 189].

Another example comes from Kremer *et al.* who exposed an H_2 target to CEP-stabilized, 6 fs, 4.4×10^{14} W/cm^2 laser pulses and observed asymmetries for KER values between 0.4 and 3 eV [121] — energies they attributed to bond softening (BS) and not electron recollision,

[1] Estimate is for a laser repetition rate of 1 kHz

which appears at higher KER. They proposed that the initial ionization of the H_2 generates a coherent wavepacket in H_2^+ that propagates to internuclear distances where the $1s\sigma_g$ and $2p\sigma_u$ states can be coupled by the tail end of the laser pulse [121, 188]. Bond-softening was recently found to play an even larger role in the CEP control of the dissociative ionization of D_2 at mid-infrared wavelengths by Znakovskaya *et al.* [88].

A wealth of theoretical studies have been carried out to qualitatively interpret the main features of the CEP control in these experiments on H_2. Due to the difficulty of treating the ionization and recollision steps, they have not yet been included in any *ab initio* calculations. Thus, the ionization and recollision steps have only been modeled, while the resulting H_2^+ is henceforth treated explicitly using either the time-dependent Schrödinger equation (TDSE) [50, 86–88] or semi-classical calculations [50, 112–114]. In these calculations it is assumed that an initial Franck-Condon vibrational wavepacket is created by the ionization of H_2 within the laser pulse. While these theories and experiments on H_2 have qualitative agreement, the grounds for achieving meaningful quantitative agreement have not been met.

In contrast, by studying an H_2^+ molecular ion target, the need to model the ionization step is circumvented and, with only a single electron, recollision cannot play a role. Furthermore, state-of-the-art H_2^+ calculations including nuclear rotation and intensity averaging [49, 89] provide a nearly exact description of strong-field dissociation so long as ionization remains negligible. Hence, quantitative agreement between theory and experiment for H_2^+ should be attainable, and the theoretical predictions can be verified.

6.2 Experiment

To experimentally study an H_2^+ ion beam target, the LIMDI method is used (see Section 2.2). Laser pulses of 5 fs duration with a 730 nm central wavelength are obtained at a 10 kHz repetition rate from the PULSAR laser at the J. R. Macdonald Laboratory through broadening in a neon-filled hollow-core fiber (see Section 2.3.2).

The pulses are focused to a peak intensity of 2.5×10^{15} W/cm^2 by an $f = 25$ cm spherical

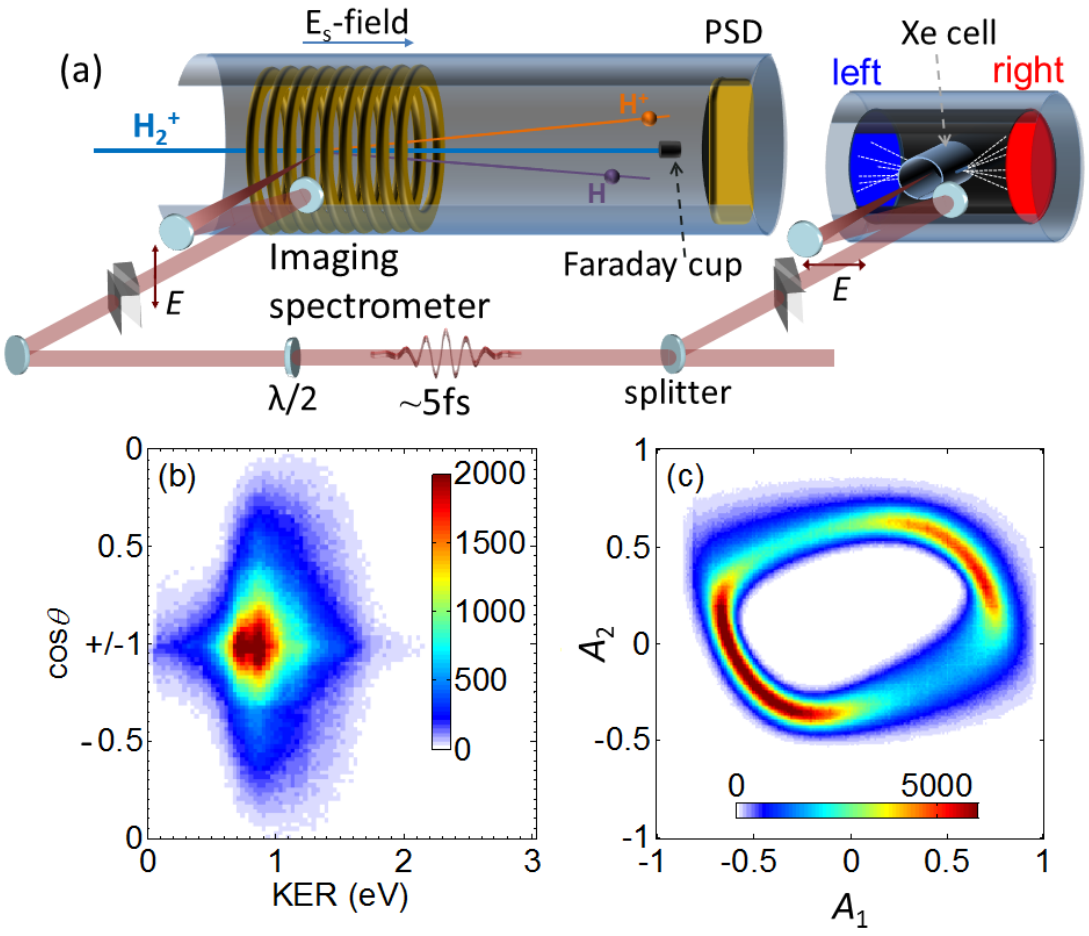

Figure 6.1: (a) Schematic of the phase-tagged ion beam experiment. Vertically polarized light is focused into the imaging spectrometer where it intersects the H_2^+ ion beam. The fragments are detected on a time and position-sensitive detector (PSD), while the main ion beam is collected in a small Faraday cup to normalize the measurements and protect the detector. Horizontally polarized laser pulses are focused into the Xe-filled gas cell of the phase meter, for the determination of the CEP for every laser pulse. The electrons emitted along the laser polarization are detected on detectors situated to the left and right. (b) Yield as a function of KER-cosθ for all CEP. (c) PAP taken with PULSAR. Adapted from Ref. [110].

mirror (with a Rayleigh length of about 1.2 mm). The focused laser beam intersects the ion beam 2 mm in front of the laser focus, where the peak intensity is 4×10^{14} W/cm^2, in order to take advantage of the larger interaction volume and therefore higher count rate. More importantly this minimizes the impact of the Gouy phase shift [241]. Recall from Section 2.2

that the ion and laser beams cross each other within the imaging spectrometer, which has an applied static electric field, E_s, to separate the ionic and neutral beam fragments in time, as shown schematically in Fig. 6.1(a). The H^+ and H fragments are detected in coincidence on a position- and time-sensitive detector (PSD), while the undissociated molecules are collected by the small Faraday cup. More details on the experimental method can be found in Section 2.2 and in Refs. [131, 132].

To monitor the CEP of the pulses, a single-shot stereographic above threshold ionization (ATI) phase meter is employed (see Chapter 4 and Refs. [99, 123, 195]). A broadband beamsplitter picks off 20% of the laser beam, which is then focused by an $f = 25$ cm spherical mirror into the Xe-filled gas cell of the phase meter [see Fig. 6.1(a)]. By simultaneously recording the information from the CEP meter and the molecular dissociation imaging setup, the H_2^+ dissociation event is tagged with the CEP of the associated laser pulse. The parametric asymmetry plot (PAP) is shown in Fig. 6.1(c). The experimental data shown in this Section were taken over 7 hours. In order to reduce the error in the conversion from measured to actual CEP, the data are divided into 20 time-ordered sections and the calculation of the CEP for each section is based on the reference PAP measured during the same time interval [198].

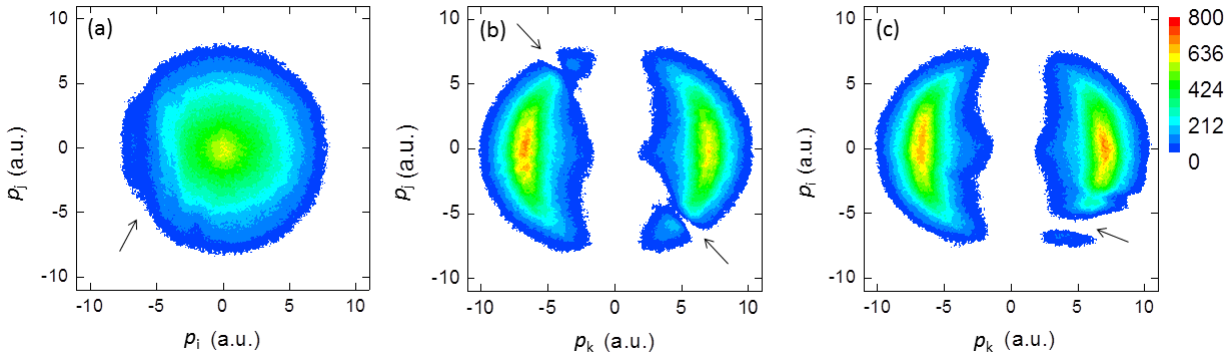

Figure 6.2: Yield as a function of momentum for all CEP, specifically (a) p_i and p_j, (b) p_k and p_j, and (c) p_k and p_i, where k is along the laser polarization. Arrows point to the losses in the spectra either due to noise on the detector, or from the rod which holds the Faraday cup.

The position and time information allows for the reconstruction of the 3D momenta, shown in Fig. 6.2. Due to the rod which holds the Faraday cup, and noise on the detector position signals, some fragments are lost. These losses are depicted by arrows in Fig. 6.2. Using the symmetry of the distributions, the "holes" could be filled in. However, as we are interested in the phase dependence of the asymmetry along the laser polarization, reconstructing the losses is not necessary. The losses do introduce meaningless offsets in the asymmetry parameter, therefore we corrected the offset such that the asymmetry oscillates around zero.

From the 3D momenta, the KER and angular distributions are evaluated (see Appendix B). The yield as a function of KER and $\cos\theta$ is shown in Fig. 6.1(b) where θ is the angle between the H^+ dissociation momentum and the polarization of the laser field. Several characteristic features can be identified in the figure. The peak of bond softening (BS) [54] occurs around 0.86 eV, and it has a "nose" that extends to low energy, where zero-photon dissociation (ZPD) plays a role [58, 59]. Above threshold dissociation (ATD) [56, 89] manifests at higher energies (>1.2 eV). The angular distribution shows that H_2^+ dissociation is preferred when the molecular axis is nearly aligned with the laser polarization axis (assuming an axial recoil approximation [242]). Furthermore, the width of the distribution gives an indication of the number of photons involved [243, 244]. For example, BS is a net one photon process, and it exhibits the broadest angular distribution. Meanwhile ZPD and ATD involve two or more photons, and they exhibit a narrower angular distribution. The CEP-averaged KER for angles $\theta \leq 36.9°$ is shown in Fig. 6.3(a). This choice of angular cut is discussed later.

For H_2^+ dissociation events, the normalized spatial asymmetry is given by

$$A(\mathrm{KER}, \phi) = \frac{N_u(\mathrm{KER}, \phi) - N_d(\mathrm{KER}, \phi)}{N_u(\mathrm{KER}, \phi) + N_d(\mathrm{KER}, \phi)}, \tag{6.1}$$

where $N_{u(d)}(\mathrm{KER}, \phi)$ is the number of $H^+ + H$ events with the proton emitted in the up (down) direction, defined by $\cos\theta$ being positive (negative). The resulting asymmetry map, $A(\mathrm{KER}, \phi)$, is shown in Fig. 6.3(b). For visualization, the data that is recorded from 0 to 2π is duplicated from 2π to 4π.

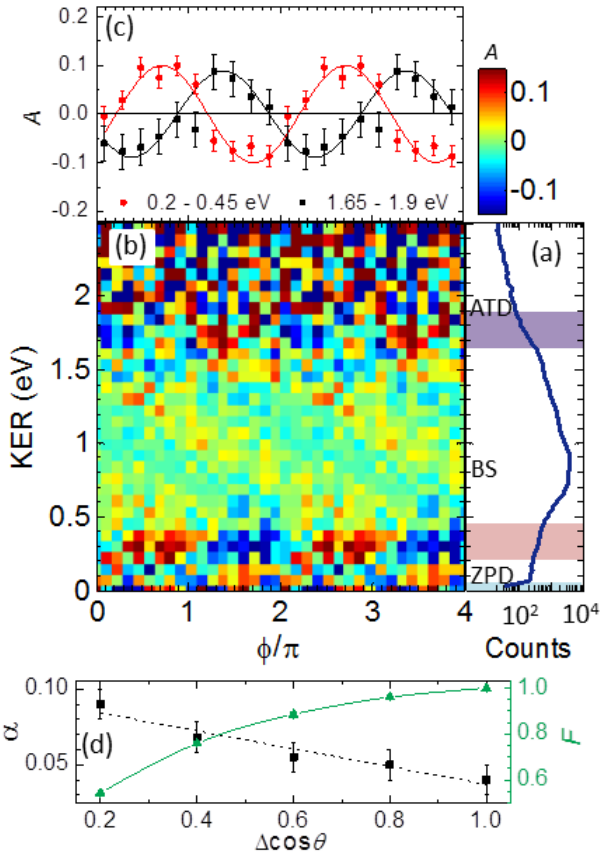

Figure 6.3: (a) KER spectrum of H_2^+ dissociation by 5 fs, 4×10^{14} W/cm^2 laser pulses, averaged over ϕ. The upper (purple) and middle (pink) shaded regions indicate the regions where the highest asymmetries are observed, and the lower (blue) shaded region indicates the losses into the Faraday cup. (b) The corresponding asymmetry map showing the dependence of A(KER,ϕ) on KER and CEP. The data are shown for fragments within a cone, $\Delta\cos\theta = 0.2$, around the polarization axis. For each KER bin, the asymmetry is shifted to oscillate around zero to compensate for instrumental losses. (c) The asymmetry parameter integrated over the indicated energy regions, and fit to sinusoidal curves (see text). (d) The dependence of the asymmetry amplitude α and fraction of the total counts F within the high energy range on the angular range $\Delta\cos\theta$ (lines to guide the eye), adapted from Ref. [110].

A clear CEP-dependent asymmetry is present in the very low KER region (0.2 – 0.45 eV), that has not been observed in earlier studies on neutral H_2. A second strong CEP-dependent asymmetry is observed at higher KER (1.65 – 1.9 eV). The asymmetries within these two

regions are shown in Fig. 6.3(c) as a function of CEP. For these two KER ranges, the asymmetry parameters were fit to sinusoidal curves, $A(\phi) = \alpha\cos(\phi+\phi_0)$ — where α is the asymmetry amplitude and ϕ_0 is an offset. The observed periodicity was predicted by theory involving interference of pathways, starting and ending on the same energy, that differ by one photon (see Refs. [49, 84]).

For the higher KER region, α is plotted for several cone angles about the polarization axis, indicated by $\Delta\cos\theta$ in Fig. 6.3(d), along with F, the fraction of the total counts within this energy range. As $\Delta\cos\theta$ is decreased, the asymmetry amplitude increases. Thus, the cut $\Delta\cos\theta$=0.2 (*i.e.* $\theta \leq 36.9°$) was chosen for the comparison between experiment and theory. With this choice of angular integration, some weak oscillations between 0.5 and 1.5 eV having $\alpha\approx$0.02 with a KER-dependent offset ϕ_0 (*i.e.* tilt) appear in Fig. 6.3(b).

6.3 Theory

The origin of the CEP oscillations in the asymmetry can be understood within the theoretical framework, based on pathway interference, proposed by Esry and coworkers [49, 84, 89, 108]. To mimic the conditions of the experiment on H_2^+, the calculations start from an incoherent population of vibrational levels with a Franck-Condon distribution in the $1s\sigma_g$ state of H_2^+ (generated by electron-impact ionization in the ECR). The dissociation occurs through laser-induced coupling to the $2p\sigma_u$ state. For a single vibrational level the dissociation can occur via different pathways through the absorption/emission of different net numbers of photons leading to the same final energy. When the difference between the net number of photons for two pathways is odd, then the resulting nuclear parity states are even and odd — the conditions under which interference occurs. This interference gives rise to a spatial asymmetry [49, 84, 89, 108].

In Figs. 6.4(b) and (a), the calculated asymmetry map and KER spectrum for 5 fs Gaussian pulses at 1×10^{14} W/cm^2 with a central wavelength of 730 nm, are shown. Overall, the theory agrees well with the experiment. As ϕ is only known up to a constant, arbitrary

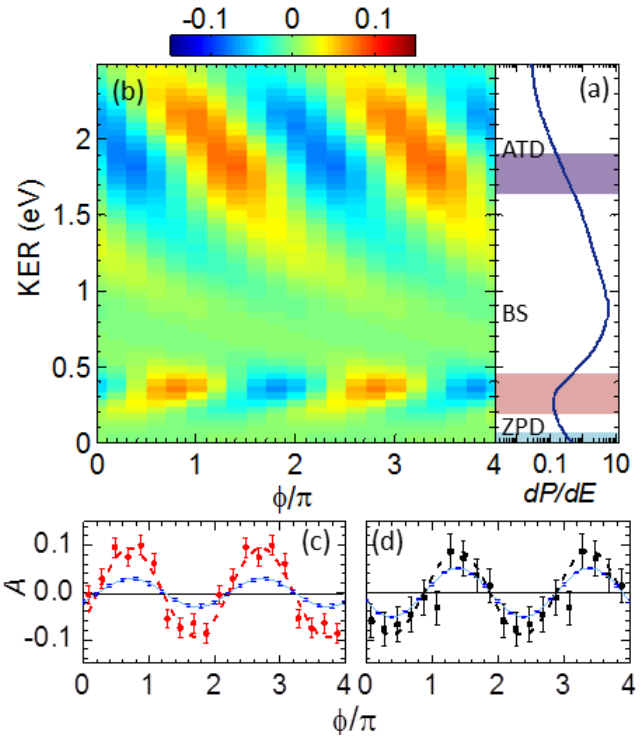

Figure 6.4: Calculated (a) ϕ-averaged dissociation probability, dP/dE, as a function of KER with the same shaded regions as in Fig. 6.3(a) and (b) A(KER,ϕ) as a function of KER and ϕ for the dissociation of H_2^+. The experimental asymmetry, averaged over the (c) low and (d) high KER regions, re-plotted from Fig. 6.3(c). The dashed light blue lines are theoretical predictions for the same KER regions, with the theoretical error bar plotted in dark blue. The calculations include Franck-Condon and intensity averaging for 1×10^{14} W/cm^2, adapted from Ref. [110].

offset in the experiment, the ϕ axes of the measured data were shifted by 0.18π to match theory in the high KER region [see Fig. 6.4(d)]. The experimental and theoretical low-KER asymmetry, shown together in Fig. 6.4(c), are in phase with each other. Furthermore, the experimental and theoretical α are in good agreement for the high KER, meanwhile theory underestimates α by about a factor of three for the low KER. Achieving better quantitative agreement will require further study (both experimental and theoretical). A likely contributor to the difference for the present case stems from having assumed a Gaussian laser pulse profile, which is not a true representation of the pulses used in the experiment. Other possible sources for the discrepancy can be the differences in the intensity or pulse duration.

The pulse duration is only known to within an estimated ±0.5 fs, and therefore might be shorter than the quoted 5 fs. A shorter pulse is expected to result in a higher asymmetry amplitude [108].

6.4 Pathways

The agreement between theory and experiment is sufficiently good to use the theory to help identify the pathways that produce the observed asymmetry. While experimentally the $1s\sigma_g$ and $2p\sigma_u$ final states are not distinguishable, as they share the same asymptotic energy, theory allows for their separation. The asymptotic relative momentum between an H^+ and an H is calculated as an outgoing-wave atomic scattering state, constructed from a linear combination of the $1s\sigma_g$ and $2p\sigma_u$ nuclear wavefunctions taking the indistinguishability of the nuclei and their spin into account [49, 89]. The calculated molecular channel dissociation probabilities (dP/dE, which is shorthand for $dP/dKER$) as a function of KER spectra for each initial vibrational state are shown in Fig. 6.5.

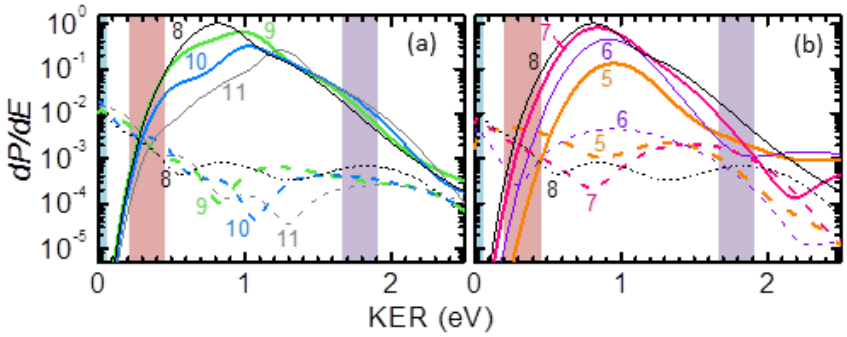

Figure 6.5: Intensity averaged dissociation probability, dP/dE, as a function of KER for H_2^+ in select initial vibrational levels (as indicated), weighted by their Franck-Condon factors, with the angular cut, $\Delta\cos\theta$=0.2. The $2p\sigma_u$ (solid lines) and $1s\sigma_g$ (dashed lines) dissociation probabilities have comparable magnitudes for the (a) low (shaded pink) and (b) high (shaded purple) KER regions exhibiting high asymmetry. Adapted from Ref. [110].

Figure 6.5 suggests that the pathways contributing to the interference in the high- and

low-KER regions start from different vibrational levels. In the low KER region (0.2 – 0.45 eV), ZPD, which is a two-photon Raman process resulting in the net absorption of zero photons from the field [58, 59], interferes with one-photon BS. The former appears in the $1s\sigma_g$ KER spectrum; and the latter, in the $2p\sigma_u$ spectrum. Where these two probability densities, dP/dE, have comparable magnitude, their interference will have the largest contrast. For the $v = 4-12$ states, a subset of which are shown in Fig. 6.5(a), the $1s\sigma_g$ and $2p\sigma_u$ contributions become nearly equal in magnitude precisely at the low KER range for which a high asymmetry is observed.

In the higher KER range (1.65 – 1.9 eV), the asymmetry likely arises from an interference of one-photon BS and net two-photon ATD [245]. The vibrational levels $v = 5-8$ meet the requirements for generating an asymmetry in this region, [see Fig. 6.5(b)]. Three-photon ATD contributes at higher KER with a tail that extends to lower KER, and thus, the three-photon ATD likely does not play a major role in the observed asymmetry. However, the two-photon and three-photon ATD can also interfere and cause an asymmetry in the high KER region. Nevertheless, as the photon number is not a physical observable, these pathway labels are only approximate. Even in the theoretical molecular channel KER spectra for the individual vibrational states there are no clearly distinguishable photon peaks. What theory allows us to definitively state is that the net number of photons was even for the $1s\sigma_g$ channel or odd for $2p\sigma_u$.

According to the theory, the difference in the phase offset between the two KER regions, shown in Fig. 6.3(c), stems from the different pathways contributing to the interference. Moreover, the "tilt" in the asymmetry map can be understood from the fact that at a given intensity and CEP, the relative phase between the interfering pathways also depends on the KER. Preliminary measurements at higher intensities, shown in Fig. 6.6, support this statement, as the tilt appears to be stronger, for instance, in the measurement at 3×10^{15} W/cm^2.

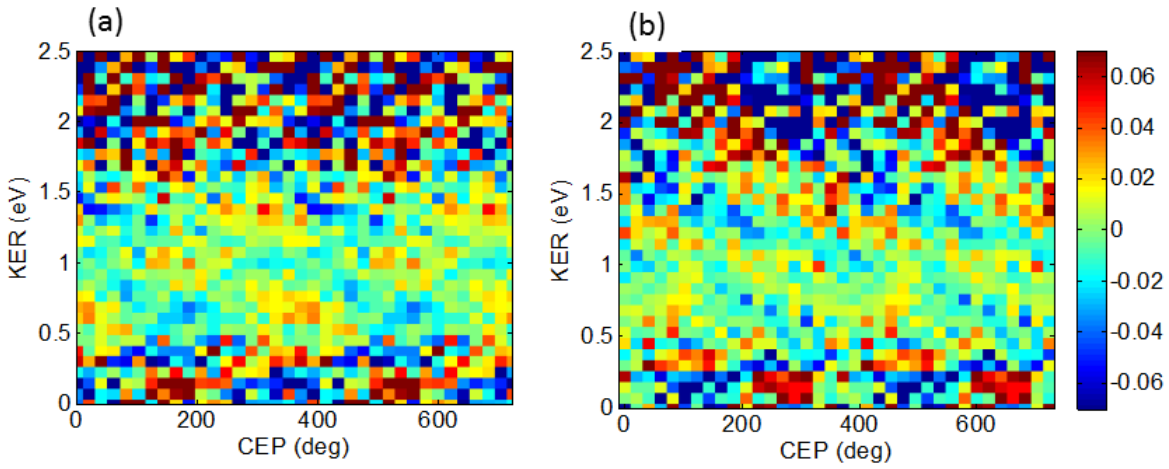

Figure 6.6: Measured asymmetry maps for the dissociation of H_2^+ at a peak intensity of (a) $9{\times}10^{14}\,\mathrm{W/cm^2}$ and (b) $3{\times}10^{15}\,\mathrm{W/cm^2}$. The data recorded from 0° to 360° are duplicated from 360° to 720°. Note that for each KER bin, the average asymmetry value was subtracted such that any CEP-dependent oscillation is around zero.

6.5 Yield

One further advantage of our method is that it facilitates the measurement of relative total dissociation yields as a function of CEP. Thus, motivated by Hua and Esry's prediction of a weak CEP effect in the energy-integrated total yield for non-rotating H_2^+ in 5.9 fs, $10^{14}\,\mathrm{W/cm^2}$ pulses [84], we searched for but found no discernible dependence of the total yield, integrated over all KER, on CEP within our error bars. A map of the measured yield as a function of CEP and KER is shown in Fig. 6.7. This finding is consistent with the present calculations, which give a relative modulation depth of 0.065%. And, despite our ability to make cuts in the angular distribution to select the molecules that broke while nearly aligned with the laser polarization (limited by post-dissociation rotation [246]), intensity averaging apparently washes out any effect. In contrast, Xu *et al.* observed modulation depths of up to 5% in the $H^+ + H$ starting from an H_2 target, with 6 fs, $6 \times 10^{14}\,\mathrm{W/cm^2}$ pulses [122]. Furthermore, work done in parallel to this work, with slightly shorter laser pulses of 4.5 fs, showed substantial yield modulations with CEP for the KER regions 0.2 – 0.5 eV and 1.75 –

2.0 eV (similar to the KER regions discussed in our work) [111].

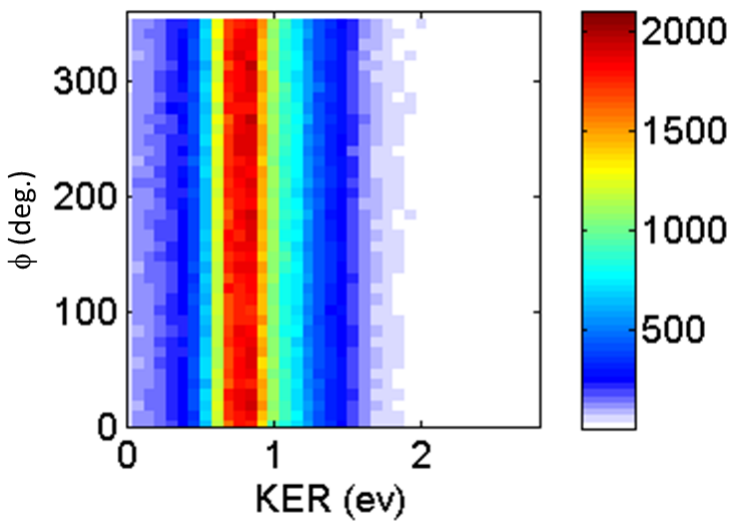

Figure 6.7: H_2^+ dissociation yield as a function of KER and ϕ for 4×10^{14} W/cm^2, 730 nm, 5 fs laser pulses.

6.6 Summary and Future work

In summary, CEP effects have been demonstrated in the dissociation of an H_2^+ molecular ion beam by intense, few-cycle laser fields. Using an H_2^+ ion beam target, instead of a laser populated H_2^+ target as in previous experiments, allowed for direct, unambiguous, quantitative comparisons with nearly exact theory. The mechanisms of the CEP control were identified as interference of pathways involving different photon numbers. This picture applies universally, and gives a good basis for understanding the role that CEP plays in strong-field coherent control. However, further work is needed to achieve quantitative agreement between experiment and theory. By replacing one of the hydrogens of H_2^+ with a deuteron, the nuclei become distinguishable and there are now two dissociation channels: $H^+ + D$ and $H + D^+$. An interesting question arises: by varying the CEP of the laser pulse, can we control which dissociation channel is preferred? Theory by Roudnev *et al.* [85, 240]

has predicted that the channel control is possible, and this question remains on our "to-do" list for future endeavors.

Chapter 7

Thick-Lens VMI

Velocity map imaging (VMI) is a technique where either ions or electrons, generated in a localized interaction volume, are projected onto a two-dimensional MCP detector with a phosphor screen anode. A camera, synchronized to the laser pulse, takes pictures of the light flashes from the phosphor screen, which are recorded by a computer. An Abel inversion process, such as onion peeling [247] or BASEX [248], is then applied to the stored images to retrieve the central slice of the 3D momentum. In this Chapter, a "thick-lens" (TL)-VMI spectrometer design is presented that allows for measuring higher energy electrons and achieving higher resolution, compared to the three electrode design by Eppink and Parker [124]. The TL-VMI has been operating in JRML at Kansas State University. Due to its success, the design has been copied in labs across the world, including in Florida, South Korea, and Australia. This Chapter, based on Ref. [249], focuses on the new design as it pertains to electrons and scaling up their measurable energies.

7.1 Motivation

In contrast to the COLTRIMS and LIMDI techniques discussed in Sections 2.1 and 2.2, respectively, VMI is not a coincidence technique, nor does it operate in event mode. Usually the count rate using VMI is only limited by space charge effects when too many charged particles are created in close proximity to each other [204] resulting in a blurring of the image. Thus, VMI has the advantage of having much higher count rates than coincidence

techniques. As a consequence, processes with low probabilities can be studied. The ability to make measurements with high statistics, for example, allowed De *et al.* to extract the quantum-beat frequency for O^{2+} fragment of an O_2 target ionized and dissociated by a pair of 8 fs infrared laser pulses with a variable delay between them [250]. On the other hand, VMI studies have the disadvantage that the data cannot be further processed in ways that event mode data can be (*e.g.* gating on events that satisfy a certain criterion and processing them again).

The original VMI spectrometer was designed by Eppink and Parker [124] and has been widely used around the world. It simply consists of three electrodes — a repeller, an extractor, and a ground plate. With voltage applied to the repeller and extractor, an electrostatic lens is formed. Ions or electrons generated in the interaction region (between the repeller and extractor) are projected onto an imaging detector. The distance from the interaction region to the detector is relatively long, which gives rise to good energy resolution, yet limits the highest possible energies that can be detected. Typically, the standard VMI, with an overall length (interaction region to the detector) of about 40 cm, can measure electrons up to about 100 eV, with −10 kV on the repeller.

However, there is a great need to be able to measure electrons with much higher energies. For instance, studies with long laser wavelengths also have high ponderomotive energies (U_p), as U_p scales quadratically with wavelength. Thus high-order above threshold ionization, which "cuts off" at $10U_p$ [251], can easily reach 1.5 keV energies for 2 μm pulses versus 240 eV energies for 800 nm pulses with laser intensities on the order of 10^{13} W/cm^2. For example, by ionizing argon with 3.6 μm laser wavelengths, Colosimo *et al.* reported energies up to 1 keV [252].

Despite the increasing need, imaging electrons which carry such high energies remains a difficult task. Recent experiments by Blaga *et al.* [253] have used time of flight (TOF) to measure back scattered electrons with momenta up to 8.5 a.u. (∼980 eV). In order to measure the angular distribution, however, they needed to make a series of measurements,

rotating the laser polarization (using a half wave plate) and only managed an energy resolution ($\Delta E/E$) of 1.4%. This is just one case, where the angularly resolved VMI technique, capable of measuring high energy electrons, could be beneficial.

7.2 TL-VMI Design

The main purpose of the new VMI design [249] is to extend the energy range for which electrons can be detected, up to 1 keV. Measuring high energy electrons in VMI is further complicated by the fact that the polarization vector has to be aligned parallel to the detector and electrons are typically ejected along the laser polarization. Therefore a field strong enough to bend the charged particle trajectory such that it is confined within the radius of the detector, given the time it takes to reach the detector, is needed. This is accomplished in three ways. The first is by using a stronger field — which requires the capability to apply tens of kilovolts to the spectrometer. The second is by extending the distance over which the field is applied. And the third is by shortening the length from the interaction region to the detector plane. The challenge is to implement these changes without significant deterioration of the energy resolution.

To achieve this, the TL-VMI spectrometer is made up of 11 electrodes, including a repeller and an extractor, which is the third electrode away from the repeller, as depicted in Fig. 7.1. The length from the interaction region to the detector plane is 12.7 cm. The electrodes are equally spaced, except for the repeller and the first electrode, which have twice the gap size to allow for the passage of the laser beam. For the case where electrons are to be detected, it is important to have a μ-metal shield around the entire path, to reduce any magnetic fields that may be present. The detector, camera, and all other elements are the same as those used in the standard VMI design [124].

To set the electric field, a voltage drop was applied across the electrodes of the TL-VMI. The voltages along the central axis of the TL-VMI are shown in Fig. 7.2 for the case where the repeller voltage is -10 kV and the extractor voltage is 82% of the repeller

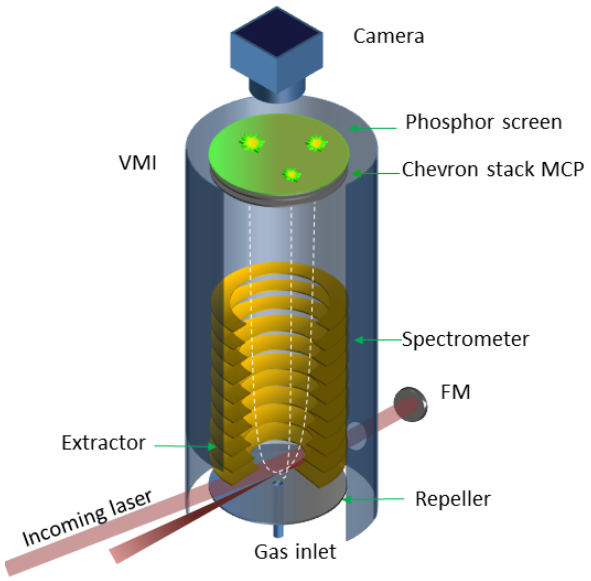

Figure 7.1: Schematic of the thick lens VMI apparatus. The laser beam enters between the repeller and first spectrometer electrode and is focused back into the effusive jet by a 7.5 cm focusing mirror (FM). Ionized electrons are accelerated towards the detector (chevron stack MCP with phosphor screen) by the electrostatic field of the spectrometer.

voltage. The last ring and the front of the MCP stack are at ground potential. The effect of this distribution of voltages is that an electrostatic lens is formed. The lens is designed to spatially focus charged particles with the same initial velocity vector to the same position on the detector, despite being generated in different positions within the interaction region [124]. The focusing strength of the lens is adjustable by tuning the extractor voltage. We found that the best extractor voltage is close to 82% of the repeller voltage. In practice, the voltages for the repeller, the first two rings, and the extractor are independently adjustable in order to fine tune their settings to obtain the highest resolution images. This also helps to account for any small differences between the simulated spectrometer and the actual spectrometer.

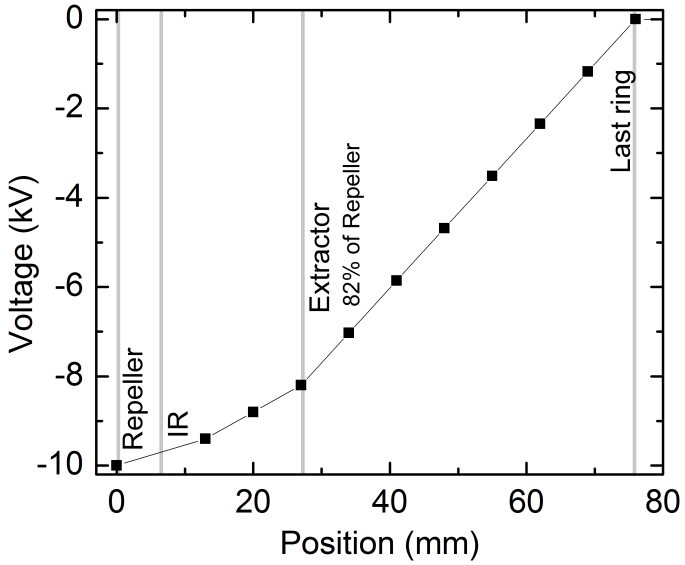

Figure 7.2: Distribution of voltages applied to the rings of the TL-VMI. Gray lines mark the repeller, interaction region (IR), extractor, and last ring. The detector is located 133.5 mm from the repeller, which was defined as 0 mm.

7.3 Simulation

Using SIMION [254, 255], a group of electrons with the same initial velocity are released into the electric field within the interaction region. The group, consisting of 5 electrons, forms a plus sign (see Fig. 7.3(a)), with a diameter of 2 mm, which over-estimates typical interaction regions by a factor of ∼10. Several electron groups are needed to simulate different energies. In Fig. 7.3, four groups of electrons, indicated by different colored trajectories, are used to illustrate the focusing properties of the setup.

In an experiment, the electrons have an initial angular distribution. However, 3D imaging can only be achieved after an inversion of the VMI images. This would require considerably more effort in the simulations, as the trajectories of a large ensemble of electrons would be necessary in order to generate the full picture. Only then can the full image be inverted to regain the central slice of the 3D distribution. Instead, a single angle is purposefully chosen to demonstrate the capabilities of the VMI, that is an "elevation angle" of 90° (*i.e.* the initial velocity is parallel to the detector plane), which simulates the central slice without

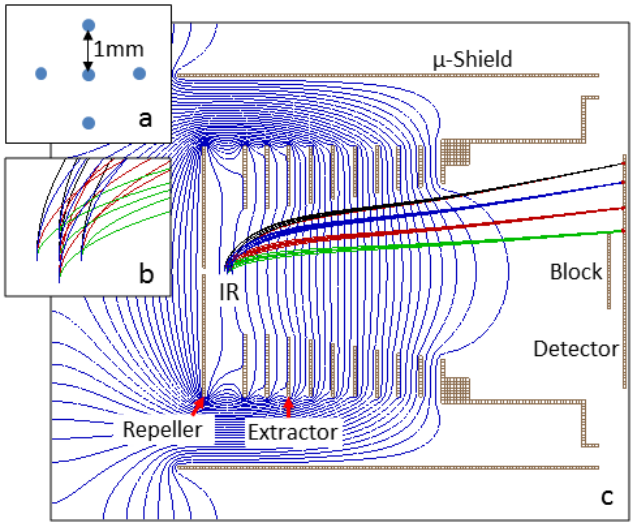

Figure 7.3: Typical Simion simulation for the thick lens VMI. (a) The initial spatial distribution for each electron group. (b) The initial trajectory of the simulated electrons. (c) Four groups of five electrons were simulated with 40, 100, 200, and 300 eV energies (corresponding to green, red, blue, and black colored trajectories, respectively). The repeller voltage was −10 kV and the extractor voltage was −8.2 kV. The equipotential lines (blue) show the formation of the electrostatic lens. The retractable block, located just in front of the detector, is used to shield the detector if the low energy electrons are saturating the MCP.

the need for inversion.

A typical SIMION simulation is shown in Fig. 7.3(c), where electrons with 40, 100, 200 and 300 eV were simulated using a repeller voltage of −10 kV and an extractor voltage of −8.2 kV. The trajectories of the 5 electrons for a given energy group converge spatially as they get closer to the detector. To determine the resolution of the instrument, the radius, R (the average distance from the center of the detector to the center of the group of electrons), and ΔR (the difference between the largest and smallest radii within the energy group) for each electron group are examined. As $E = \frac{1}{2}m(\frac{R}{t})^2$, where E is the energy, m is the mass, and t is the time of flight for the electron, the relative error (*i.e.* energy resolution) is $\Delta E/E \approx 2\Delta R/R$. The results are presented in Fig. 7.4(a) and (b) for electron energies ranging from 0 to 360 eV. As the percentage of voltage on the extractor is decreased, the electron energy with the best resolution shifts to higher values. In most cases, one would

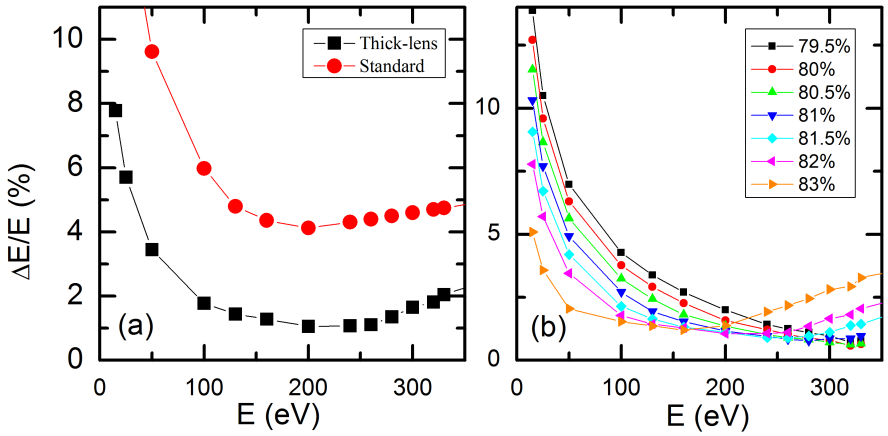

Figure 7.4: Energy resolution versus electron energy for (a) the standard VMI design compared to the TL-VMI design and (b) various extractor settings for the TL-VMI design. Here the repeller voltage was −10 kV.

likely choose a value for the extractor which puts the focus in the middle of the energy range of interest (*e.g.* 82% gives the best resolution for the range 100 – 300 eV electrons). Furthermore, to study different energy ranges, the voltages only need to be scaled.

To illustrate the difference between the TL-VMI and the standard VMI, a simulation was also carried out for the original design by Eppink and Parker [124], but with a flight length of 8.3 cm to allow for detection of electrons up to 360 eV. The comparison of the simulated resolution for the two designs is shown in Fig. 7.4(a). The two VMI designs were compared with −10 kV on the repeller and −9.5 kV and −8.2 kV on the extractor for the standard design and for thick lens design, respectively. The shapes of the two curves are fairly similar, but the magnitude of the resolution error is about four times better for the TL-VMI design for 200 eV electrons.

An important consideration for a VMI design is the relationship between the energy of the particle being measured and its radius R on the detector — as the relation $E \propto R^2$ is used to convert the radius to energy. Fig. 7.5(a) and (c) show the dependence of R^2 on electron energy for both low and high energy electrons considered for the TL-VMI design. The simulated data fit a linear trend fairly well, confirmed by the residuals plotted in Fig. 7.5(b)

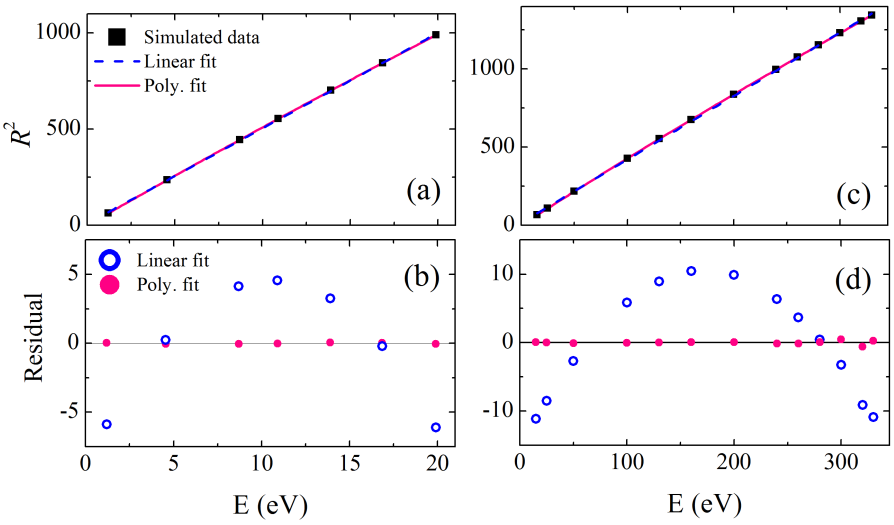

Figure 7.5: The "linearity" of R^2 versus electron energy for (a) the low-energy region (b) and its residual analysis for both a linear fit and a second order polynomial fit. Similarly, (c) shows the linearity and (d) shows the residual analysis for the high-energy region.

and (d). However, using a second order polynomial, although slightly more cumbersome for converting the radius to energy in practice, gives a much better fit, with the residual less than 1 mm^2 for all energies considered.

7.4 Implementation

Our colleagues in South Korea, at POSTECH, have also built a TL-VMI and carried out further simulations to characterize the device. They "manually" tune their voltages to try to further improve the resolution capabilities. An example of their electron trajectories is shown in Fig. 7.6(a), considering a voltage profile given in Fig. 7.6(b).

In order to try to experimentally test the capabilities of the TL-VMI design, ATI of xenon was studied using a 532 nm, 120 picosecond, linearly polarized laser. The pulses were focused by an $f = 45$ cm lens into an effusive Xe gas target. The estimated peak intensity in the experiments was 2×10^{12} W/cm^2. The low energy photoelectrons were projected onto the detector by applying -1 kV on the repeller and a voltage profile as depicted in Fig. 7.6(b)

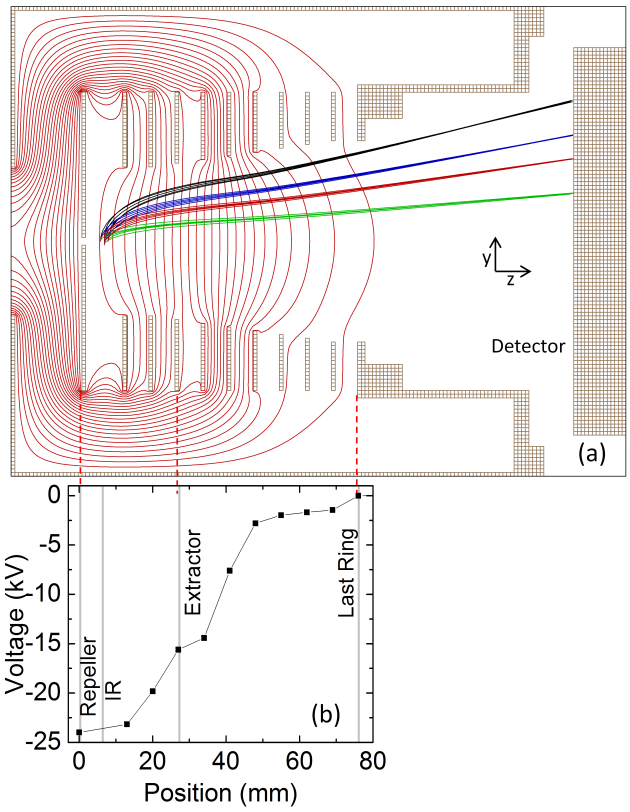

Figure 7.6: (a) TL-VMI geometry with manually tuned voltage profile as implemented at POSTECH, showing the simulated trajectories for 100 eV (green), 300 eV (red), 500 eV (blue), and 900 eV (black) electron groups. (b) Distribution of voltages along the electrodes of the POSTECH TL-VMI.

for the remaining electrodes.

The energy spectrum for the angular distribution within a cone of 25° around the laser polarization, is shown in Fig. 7.7(a). The four photoelectron peaks correspond to six-photon (first two peaks) and seven-photon (last two peaks) absorption from Xe [256, 257]. Using this data set, we also made a quantitative comparison between the experiment and the simulations. For this comparison, the interaction volume was modeled as $100\,\mu\text{m} \times 100\,\mu\text{m} \times 600\,\mu\text{m}$ based on estimates of the beam waist in the focus and the width of the effusive gas jet at the laser focus. For these parameters, the measured and simulated data agree well, see Fig. 7.7(b). An additional simulation was carried out for an interaction volume of $100\,\mu\text{m} \times 100\,\mu\text{m} \times 350\,\mu\text{m}$ to illustrate the dependence of the res-

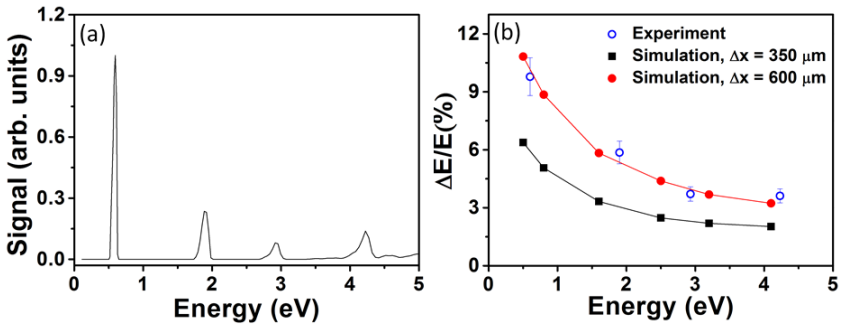

Figure 7.7: Energy spectrum of ATI in xenon, for a 25° cone around the laser polarization. (b) Comparison of the experimental resolution and SIMION simulations.

olution on interaction volume. A more ideal test of capabilities of the TL-VMI would be to study photoionization processes with a synchrotron source, where electrons are released with higher energies and the bandwidth of the light source is narrow.

In summary, a TL-VMI was designed, characterized, and implemented. This new design gives unprecedented energy resolution for angularly resolved measurements compared to similar 3D imaging techniques. The achievable electron energies that can be measured extends to 360 eV, with −10 kV on the repeller. Our simulations indicate that with −30 kV, electron energies up to 1 keV can be detected, with similarly good resolution, as shown in Fig. 7.8 for both voltage profiles discussed in this Chapter, considering a 1 mm × 1 mm × 1 mm interaction volume.

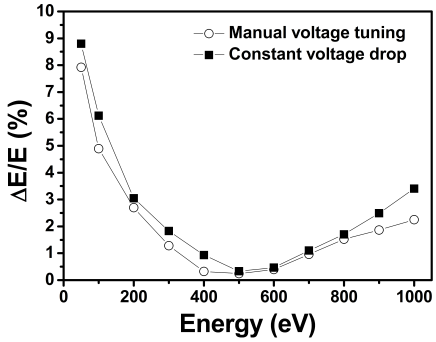

Figure 7.8: Resolution of the TL-VMI for the two different voltage profiles using -30 kV on the repeller, and an interaction volume of 1 mm × 1 mm × 1 mm.

Furthermore, good agreement is found for the comparison of the SIMION simulation to the experimental resolution, for low energy photoelectrons from ATI in xenon. Further comparisons to experiments with higher energy photoelectrons have yet to be done. Nevertheless, the TL-VMI shows great promise for high energy resolution detection of electrons over a large energy range.

Chapter 8

Summary and Future Directions

In conclusion, significant steps toward the control of electron and nuclear motion have been achieved. And, through experimental and theoretical studies on strong-field laser-matter interaction, the questions posed in the introduction "what are the mechanisms behind the control, and to what degree can electron and nuclear motion be controlled?" are starting to have concrete answers. Our main findings are summarized here.

The previously developed LIMDI experimental technique [52] facilitated the novel measurement of kinematically complete charge asymmetric dissociation of CO^+. By varying the pulse duration and intensity, the dynamics of the dissociation process to $C^{2+} + O$ products were explored. The data are consistent with a pathway that involves excitation of the CO^+, which allows the molecule to stretch to internuclear distances beyond the point where the $C^+ + O^+$ potential energy curves cross the $C^{2+} + O$ curves. Classical propagation along the excited CO^+ potential curves suggests that only a few tens of femtoseconds are needed for the nuclei to stretch far enough such that the final CAD product becomes more probable.

To alleviate the need for CEP-stabilized laser pulses, we implemented a single-shot stereo-ATI phase meter in conjunction with either the COLTRIMS or LIMDI coincidence three-dimensional momentum imaging techniques [99]. Electron dynamics were studied for NSDI of argon using the powerful phase-tagged COLTRIMS technique. Monitoring of the CEP of the laser pulses allowed for sub-cycle resolution in the measurement of the correlated electron motion for argon targets. These measurements provide highly differential experimental data,

which were modeled within a semi-classical framework. Experiments carried out under nearly identical laser parameters for NSDI of Ar and N_2 revealed strong similarities in their electron dynamics, indicating that the mechanism driving the dynamics is likely the same, namely RESI.

The phase-tagged COLTRIMS technique was also used to study laser-induced ionization processes of NO, CO [118], and C_2H_2 [120] targets. Previous work by Guo and Gibson[228] gave some indications that NSDI occurs for NO using circularly polarized laser pulses, motivating our measurements of NSDI of NO with varying ellipticity. Preliminary results indicate that NSDI of NO may survive for ellipticities greater than that for Ar. For the CEP control in the dissociative ionization of CO, in contrast to previous work by Liu *et al.* [117], we found that the initial ionization step is mainly responsible for the observed spatial asymmetry [118]. Acetylene can undergo hydrogen migration to the vinylidene configuration. Preliminary results show that the migration process can be controlled by the CEP when initiated by an intense 4 fs laser pulse. Further analysis is underway to confirm this finding.

Furthermore, the phase-tagging method made possible, for the first time, the study of CEP effects on H_2^+ molecular ion-beam targets, where low ion-beam densities severely limit the count rates. This experimental breakthrough comes nearly a decade after theory predicted CEP effects for the hydrogen molecular ion. State-of-the art TDSE calculations, including rotation and intensity averaging, carried out by Esry's theory group have allowed for meaningful quantitative comparisons between theory and experiment [110].

Finally, the thick-lens VMI design is described and characterized. The advantage of the new design is that the detectable electron energy range is extended from about 100 eV (for the Eppink and Parker design [124]) to about 1 keV. This device provides a 3D imaging capability for studying processes for which such high energies are relevant.

Future directions of this work are to extend the methods and concepts using different laser wavelengths. For instance, the recollision energy of an electron depends on the excur-

sion time in the laser field. For longer wavelengths, the excursion time is longer, and the electron can gain more energy through the ponderomotive force from the laser field. This may be of particular interest for the case of NSDI of NO, as to ionize the second electron requires a recollision energy above 30.3 eV.

Also of interest is to study the manipulation of chemical bond breaking or formation for larger systems. Our work on acetylene is a step in this direction. Studies on larger hydrocarbons, such as allene (C_3H_4), which has been shown to undergo hydrogen migration in a strong laser field [232], could provide further insight as to the possible mechanisms for CEP control over the process.

Bibliography

[1] M. Pollard, *The Light Bulb and How It Changed the World* (Facts On File, Incorporated, 1994).

[2] T. H. Maiman, "Stimulated Optical Radiation in Ruby," Nature **187**, 493 (1960).

[3] Photonics, "History of the Laser,", http://www.photonics.com/linearcharts/default.aspx?ChartID=2.

[4] S. Chu, L. Hollberg, J. E. Bjorkholm, A. Cable, and A. Ashk, "Three-Dimensional Viscous Confinement and Cooling of Atoms by Resonance Radiation Pressure," Phys. Rev. Lett. **55**, 48 (1985).

[5] L. E. Hargrove, R. L. Fork, and M. A. Pollack, "Locking of He-Ne laser modes induced by synchronous intracavity modulation," Appl. Phys. Lett. **5**, 4 (1964).

[6] D. Strickland and G. Mourou, "Compression of Amplified Chirped Optical Pulses," Optics Communications **56**, 219 (1985).

[7] P. Brumer and M. Shapiro, "Laser Control of Molecular Processes," Annu. Rev. Phys. Chem. **43**, 257 (1992).

[8] F. Krausz and M. Ivanov, "Attosecond physics," Rev. Mod. Phys. **81**, 163 (2009), and references therein.

[9] J. D. Bhawalkar, G. S. He, and P. N. Prasad, "Nonlinear multiphoton processes in organic and polymeric materials," Rep. Prog. Phys. **59**, 1041 (1996).

[10] W. Waidelich and P. Kiefhaber, eds., *Laser/Optoelectronics in Medicine*, vol. II (Springer, Berlin, 1986).

[11] M. Dierolf, A. Menzel, P. Thibault, P. Schneider, C. M. Kewish, R. Wepf, O. Bunk, and F. Pfeiffer, "Ptychographic X-ray computed tomography at the nanoscale," Nature **467**, 436 (2010).

[12] S. Schell and J. J. Wilkens, "Dosimetric effects of energy spectrum uncertainties in radiation therapy with laser-driven particle beams," Phys. Med. Biol. **57**, N47 (2012).

[13] J. D. Sethian et al., "Fusion energy with lasers, direct drive targets, and dry wall chambers," Nucl. Fusion **43**, 1693 (2003).

[14] J. D. Sethian et al., "The Science and Technologies for Fusion Energy With Lasers and Direct-Drive Targets," IEEE Trans. on Plasma Sci. **38**, 690 (2010).

[15] S. G. Biedron, in *CLEO: 2013* (Optical Society of America, 2013), p. AF2H.1, URL http://www.opticsinfobase.org/abstract.cfm?URI=CLEO_AT-2013-AF2H.1.

[16] A. Rondi, D. Kiselev, S. Machado, J. Extermann, S. Weber, L. Bonacina, J.-P. Wolf, J. Roslund, M. Roth, and H. Rabitz, "Discriminating Biomolecules with Coherent Control Strategies," Chimia **65**, 346 (2011).

[17] J. H. Posthumus, "The dynamics of small molecules in intense laser fields," Rep. Prog. Phys. **67**, 623 (2004), and references therein.

[18] C. F. de Morisson Faria and X. Liu, "Electronelectron correlation in strong laser fields," J. Mod. Opt. **58**, 1076 (2011), and references therein.

[19] N. J. Kylstra, C. J. Joachain, and M. Dörr, in *Atoms, Solids, and Plasmas in Super-Intense Laser Fields*, edited by D. Batani, C. J. Joachain, S. Martellucci, and A. N. Chester (Springer US, 2001), pp. 15–36, ISBN 978-1-4613-5511-3, URL http://dx.doi.org/10.1007/978-1-4615-1351-3_2.

[20] C. J. Joachain, N. J. Kylstra, and R. M. Potvliege, *Atoms in Intense Laser Fields*

(Cambridge University Press, Cambridge, 2011), URL http://dx.doi.org/10.1017/CBO9780511993459.

[21] F. Faisal, *Theory of Multiphoton Processes* (Plenum Press, New York, 1987), ISBN 9780306423178, URL http://books.google.com/books?id=rEs0X8FdKtYC.

[22] M. V. Ammosov, N. B. Delone, and V. P. Krainov, "Tunnel Ionization of Complex Atoms and Atomic Ions by an Alternating Electromagnetic Field," Sov. Phys. JETP **64**, 1191 (1986).

[23] R. V. Kulyagin and V. D. Taranukhin, "Tunneling Ionization of Atoms and Ions in a Strong Laser Field and the Effect of Local Ionization Suppression," Las. Phys. **3**, 644 (1993).

[24] X. M. Tong, Z. X. Zhao, and C. D. Lin, "Theory of molecular tunneling ionization," Phys. Rev. A **66**, 033402 (2002).

[25] X. M. Tong and C. D. Lin, "Empirical formula for static field ionization rates of atoms and molecules by lasers in the barrier-suppression regime," J. Phys. B: At. Mol. Opt. Phys. **38**, 2593 (2005).

[26] V. S. Popov, "On the Theory of Tunneling and Above-Barrier Ionization of Atoms and Ions in a Strong Laser Field," Las. Phys. **10**, 1033 (2000).

[27] V. S. Popov, "Tunnel and multiphoton ionization of atoms and ions in a strong laser field (Keldysh theory)," Phys.-Usp. **47**, 855 (2004).

[28] L. V. Keldysh, "Ionization in the field of a strong electromagnetic wave," Sov. Phys. JETP **20**, 1307 (1965).

[29] R. R. Freeman, P. H. Bucksbaum, and T. J. McIlrath, "The Ponderomotive Potential of High Intensity Light and Its Role in the Multiphoton Ionization of Atoms," IEEE J. Quant. Elect. **24**, 1461 (1988).

[30] P. Balling and J. Schou, "Femtosecond-laser ablation dynamics of dielectrics: basics and applications for thin films," Rep. Prog. Phys. **76**, 036502 (2013).

[31] P. B. Corkum, "Plasma Perspective on Strong-Field Multiphoton Ionization," Phys. Rev. Lett. **71**, 1994 (1993).

[32] M. Lewenstein, P. Balcou, M. Ivanov, A. L'Huillier, and P. Corkum, "Theory of high-harmonic generation by low-frequency laser fields," Phys. Rev. A **49**, 2117 (1994).

[33] J. L. Krause, K. J. Schafer, and K. C.Kulander, "High-Order Harmonic Generation from Atoms and Ions in the High Intensity Regime," Phys. Rev. Lett. **68**, 3535 (1993).

[34] K. Midorikawa, "Ultrafast dynamic imaging," Nature Photonics **5**, 640 (2011).

[35] M. Kohler, T. Pfeifer, K. Hatsagortsyan, and C. Keitel, in *Advances in Atomic, Molecular, and Optical Physics*, edited by E. A. Paul Berman and C. Lin (Academic Press, 2012), vol. 61 of *Advances In Atomic, Molecular, and Optical Physics*, p. 159, and references therein, URL http://www.sciencedirect.com/science/article/pii/B9780123964823000041.

[36] Z. Chen, A.-T. Le, T. Morishita, and C. D. Lin, "Quantitative rescattering theory for laser-induced high-energy plateau photoelectron spectra," Phys. Rev. A **79**, 033409 (2009).

[37] D. B. Milošević, G. G. Paulus, D. Bauer, and W. Becker, "Above-threshold ionization by few-cycle pulses," J. Phys. B: At. Mol. Opt. Phys. **39**, R203 (2006).

[38] G. G. Paulus, W. Becker, W. Nicklich, and H. Walther, "Rescattering effects in above-threshold ionization: a classical model," J. Phys. B **27**, L703 (1994).

[39] D. N. Fittinghoff, P. R. Bolton, B. Chang, and K. C. Kulander, "Observation of nonsequential double ionization of helium with optical tunneling," Phys. Rev. Lett, **69**, 2642 (1992).

[40] A. L'Huillier, L. A. Lompre, G. Mainfray, and C. Manus, "Multiply charged ions induced by multiphoton absorption in rare gases at 0.53 μm," Phys. Rev. A **27**, 2503 (1983).

[41] B. Walker, E. Mevel, B. Yang, P. Breger, J. P. Chambaret, A. Antonetti, L. F. DiMauro, and P. Agostini, "Double ionization in the perturbative and tunneling regimes," Phys. Rev. A **48**, R894 (1993).

[42] A. Rudenko, K. Zrost, B. Feuerstein, V. L. B. de Jesus, C. D. Schröter, R. Moshammer, and J. Ullrich, "Correlated multielectron dynamics in ultrafast laser pulse interactions with atoms," Phys. Rev. Lett. **93**, 253001 (2004).

[43] T. Weber, H. Giessen, M. Weckenbrock, G. Urbasch, A. Staudte, L. Spielberger, O. Jagutzki, V. Mergel, M. Vollmer, and R. Dörner, "Correlated electron emission in multiphoton double ionization," Nature **405**, 658 (2000).

[44] E. Eremina, X. Liu, H. Rottke, W. Sandner, A. Dreischuh, F. Lindner, F. Grasbon, G. G. Paulus, H. Walther, R. Moshammer, et al., "Laser-induced non-sequential double ionization investigated at and below the threshold for electron impact ionization," J. Phys. B: At. Mol. Opt. Phys. **36**, 3269 (2003).

[45] M. F. Kling, C. Siedschlag, A. J. Verhoef, J. I. Khan, M. Schultze, T. Uphues, Y. Ni, M. Uiberacker, M. Drescher, F. Krausz, et al., "Control of Electron Localization in Molecular Dissociation," Science **312**, 246 (2006).

[46] S. L. Haan, J. S. V. Dyke, and Z. S. Smith, "Recollision Excitation, Electron Correlation, and the Production of High-Momentum Electrons in Double Ionization," Phys. Rev. Lett. **101**, 113001 (2008).

[47] A. Giusti-Suzor, F. H. Mies, L. F. DiMauro, E. Charron, and B. Yang, "Dynamics of H_2^+ in intense laser fields," J. Phys. B: At. Mol. Opt. Phys. **28**, 309 (1995).

[48] V. N. Serov, A. Keller, O. Atabek, and N. Billy, "Quantitative theory-versus-experiment comparison for the intense laser dissociation of H_2^+," Phys. Rev. A **68**, 053401 (2003).

[49] F. Anis and B. D. Esry, "Enhancing the Intense Field Control of Molecular Fragmentation," Phys. Rev. Lett. **109**, 133001 (2012).

[50] D. Geppert, P. von den Hoff, and R. de Vivie-Riedle, "Electron dynamics in molecules: a new combination of nuclear quantum dynamics and electronic structure theory," J. Phys. B: At. Mol. Opt. Phys. **41**, 074006 (2008).

[51] K. Burnett, V. C. Reed, and P. L. Knight, "Atoms in ultra-intense laser fields," J. Phys. B At. Mol. Opt. Phys. **26**, 561 (1993).

[52] A. M. Sayler, Ph.D. thesis, Kansas State University (2008).

[53] J. McKenna, F. Anis, A. M. Sayler, B. Gaire, N. G. Johnson, E. Parke, K. D. Carnes, B. D. Esry, and I. Ben-Itzhak, "Controlling strong-field fragmentation of H_2^+ by temporal effects with few-cycle laser pulses," Phys. Rev. A **85**, 023405 (2012).

[54] P. H. Bucksbaum, A. Zavriyev, H. G. Muller, and D. W. Schumacher, "Softening of the H_2^+ molecular bond in intense laser fields," Phys. Rev. Lett. **64**, 1883 (1990).

[55] A. Zavriyev, P. H. Bucksbaum, H. G. Muller, and D. W. Schumacher, "Ionization and dissociation of H_2 in intense laser fields at 1.064 μm, 532 nm, and 355 nm," Phys. Rev. A **42**, 5500 (1990).

[56] A. Giusti-Suzor, X. He, O. Atabek, and F. H. Mies, "Above-threshold dissociaation of H_2^+ in intense laser fields," Phys. Rev. Lett. **64**, 515 (1990).

[57] A. Zavriyev, P. H. Bucksbaum, J. Squier, and F. Saline, "Light-induced vibrational structure in H_2^+ and D_2^+ in intense laser fields," Phys. Rev. Lett. **70**, 1077 (1993).

[58] B. Gaire, Ph.D. thesis, Kansas State University (2011).

[59] J. H. Posthumus, J. Plumridge, L. J. Frasinski, K. Codling, E. J. Divall, A. J. Langley, and P. F. Taday, "Slow protons as a signature of zero-photon dissociation of H_2^+ in intense laser fields," J. Phys. B: At. Mol. Opt. Phys. **33**, L563 (2000).

[60] L. J. Frasinski, J. H. Posthumus, J. Plumridge, K. Codling, P. F. Taday, and A. J. Langley, "Manipulation of Bond Hardening in H_2^+ by Chirping of Intense Femtosecond Laser Pulses," Phys. Rev. Lett. **83**, 3625 (1999).

[61] S. Chelkowski, A. Conjusteau, T. Zuo, and A. D. Bandrauk, "Dissociative ionization of H_2^+ in an intense laser field: Charge-resonance-enhanced ionization, Coulomb explosion, and harmonic generation at 600 nm," Phys. Rev. A **54**, 3235 (1996).

[62] K. Codling, L. J. Frasinski, and P. A. Hatherly, "Multiphoton ionisation of H_2 and D_2 using an intense sub-picosecond laser," J. Phys. B: At. Mol. Opt. Phys. **21**, L433 (1988).

[63] H. Stapelfeldt, E. Constant, and P. B. Corkum, "Wave Packet Structure and Dynamics Measured by Coulomb Explosion," Phys. Rev. Lett. **74**, 3780 (1995).

[64] T. Zuo and A. D. Bandrauk, "Charge-resonance-enhanced ionization of diatomic molecular ions by intense lasers," Phys. Rev. A **52**, R2511 (1995).

[65] J. H. Posthumus, L. J. Frasinski, A. J. Giles, and K. Codling, "Dissociative ionization of molecules in intense laser fields: a method of predicting ion kinetic energies and appearance intensities," J. Phys. B: At. Mol. Opt. Phys. **28**, L349 (1995).

[66] D. L. Hatten, J. Zhu, J. Goldhar, and W. T. Hill, "Above Threshold Dissociation of CO^{2+}," Laser Phys. **7**, 858 (1997).

[67] A. Natan, U. Lev, V. S. Prabhudesai, B. D. Bruner, D. Strasser, D. Schwalm, I. Ben-Itzhak, O. Heber, D. Zajfman, and Y. Silberberg, "Quantum control of photodissociation by manipulation of bond softening," Phys. Rev. A **86**, 043418 (2012).

[68] T. Severt et al., "Zero photon dissociation of CS^{2+} in intense ultrashort laser pulses," (in preparation).

[69] P. Franceschi, D. Ascenzi, P. Tosi, R. Thissen, J. Žabka, J. Roithov, C. L. Ricketts, M. D. Simone, and M. Coreno, "Dissociative double photoionization of N_2 using synchrotron radiation: Appearance energy of the N^{2+} dication," J. Chem. Phys. **126**, 134310 (2007).

[70] V. Tagliamonti, H. Chen, and G. N. Gibson, "Internuclear-separation-resolved asymmetric dissociation of I_2 in a two-color laser field," Phys. Rev. A **84**, 043424 (2011).

[71] W. Eberhardt, E. W. Plummer, I. W. Lyo, R. Carr, and W. K. Ford, "Auger-electron ion coincidence studies of soft-x-rayinduced fragmentation of N_2," Phys. Rev. Lett. **58**, 207 (1987).

[72] K. Boyer, T. S. Luk, J. C. Solem, and C. K. Rhodes, "Kinetic energy distributions of ionic fragments produced by subpicosecond multiphoton ionization of N_2," Phys. Rev. A **39**, 1186 (1989).

[73] G. Gibson, T. S. Luk, A. McPherson, K. Boyer, and C. K. Rhodes, "Observation of a new inner-orbital molecular transition at 55.8 nm in N_2^{2+} produced by multiphoton coupling," Phys. Rev. A **40**, 2378 (1989).

[74] C. Guo, M. Li, and G. N. Gibson, "Charge Asymmetric Dissociation Induced by Sequential and Nonsequential Strong Field Ionization," Phys. Rev. Lett. **82**, 2492 (1999).

[75] Q. Liang, C. Wu, Z. Wu, M. Liu, Y. Deng, and Q. Gong, "Molecular dynamics of CO in few-cycle laser fields," Int. J. Mass Spectrom. **286**, 28 (2009).

[76] G. N. Gibson, M. Li, C. Guo, and J. P. Nibarger, "Direct evidence of the generality of charge-asymmetric dissociation of molecular iodine ionized by strong laser fields," Phys. Rev. A **58**, 4723 (1998).

[77] C. Cornaggia, J. Lavancier, D. Normand, J. Morellec, and H. X. Liu, "Molecular dynamics of CO in few-cycle laser fields," Phys. Rev. A **42**, 5464 (1990).

[78] S. V. Menon, J. P. Nibarger, and G. N. Gibson, "A framework for understanding molecular ionization in strong laser fields," J. Phys. B: At. Mol. Opt. Phys. **35**, 2961 (2002).

[79] H. Liu, Z. Yang, and Z. Gao, "Ionization and dissociation of CH_3I in intense laser field," J. Chem. Phys. **126**, 044316 (2007).

[80] D. T. Strickland, Y. Beaudoin, P. Dietrich, and P. B. Corkum, "Optical studies of inertially confined molecular iodine ions," Phys. Rev. Lett. **68**, 2755 (1992).

[81] K. Hoshina, Y. Furukawa, T. Okino, and K. Yamanouchi, "Efficient ejection of H_3^+ from hydrocarbon molecules induced by ultrashort intense laser fields," J. Chem. Phys. **129**, 104302 (2008).

[82] H. Xu, T. Okino, K. Nakai, K. Yamanouchi, S. Roither, X. Xie, D. Kartashov, M. Schöffler, A. Baltuska, and M. Kitzler, "Hydrogen migration and CC bond breaking in 1,3-butadiene in intense laser fields studied by coincidence momentum imaging," Chem. Phys. Lett. **484**, 119 (2010).

[83] B. H. Bransden and C. J. Joachain, *Physics of Atoms and Molecules*, vol. 2nd Ed. (Prentice-Hall, New York, 2003).

[84] J. J. Hua and B. D. Esry, "The role of mass in the carrierenvelope phase effect for H_2^+ dissociation," J. Phys. B: At. Mol. Opt. Phys. **42**, 085601 (2009).

[85] V. Roudnev, B. D. Esry, and I. Ben-Itzhak, "Controlling HD^+ and H_2^+ Dissociation with the Carrier-Envelope Phase Difference of an Intense Ultrashort Laser Pulse," Phys. Rev. Lett. **93**, 163601 (2004).

[86] F. He, C. Ruiz, and A. Becker, "Control of Electron Excitation and Localization in the Dissociation of H2 and Its Isotopes Using Two Sequential Ultrashort Laser Pulses," Phys. Rev. Lett. **99**, 083002 (2007).

[87] F. He, A. Becker, and U. Thumm, "Strong-Field Modulated Diffraction Effects in the Correlated Electron-Nuclear Motion in Dissociating H_2^+," Phys. Rev. Lett. **101**, 213002 (2008).

[88] I. Znakovskaya, P. von den Hoff, G. Marcus, S. Zherebtsov, B. Bergues, X. Gu, Y. Deng, M. J. J. Vrakking, R. Kienberger, F. Krausz, et al., "Subcycle Controlled Charge-Directed Reactivity with Few-Cycle Midinfrared Pulses," Phys. Rev. Lett. **108**, 063002 (2012).

[89] F. Anis, Ph.D. thesis, Kansas State University (2009).

[90] F. Anis and B. D. Esry, "Role of nuclear rotation in dissociation of H_2^+ in a short laser pulse," Phys. Rev. A **77**, 033416 (2008).

[91] K. J. Shafer, in *Strong Field Laser Physics*, edited by T. Brabec (Springer, New York, 2008), vol. 134.

[92] R. Panfili, J. H. Eberly, and S. L. Haan, "Comparing classical and quantum dynamics of strong-field double ionization," Opt. Exp. **8**, 431 (2001).

[93] S. L. Haan, L. Breen, A. Karim, and J. H. Eberly, "Recollision Dynamics and Time Delay in Strong-Field Double Ionization," Opt. Exp. **15**, 767 (2007).

[94] A. Emmanouilidou and A. Staudte, "Intensity dependence of strong-field double-ionization mechanisms: From field-assisted recollision ionization to recollision-assisted field ionization," Phys. Rev. A **80**, 053415 (2009).

[95] A. Kamor, F. Mauger, C. Chandre, and T. Uzer, "How Key Periodic Orbits Drive Recollisions in a Circularly Polarized Laser Field," Phys. Rev. Lett. **110**, 253002 (2013).

[96] C. D. Lin, A.-T. Le, Z. Chen, T. Morishita, and R. Lucchese, "Strong-field rescattering physicsself-imaging of a molecule by its own electrons," J. Phys. B: At. Mol. Opt. Phys. **43**, 122001 (2010).

[97] Z. Chen, Y. Liang, D. H. Madison, and C. D. Lin, "Strong-field nonsequential double ionization of Ar and Ne," Phys. Rev. A **84**, 023414 (2011).

[98] B. Bergues, M. Kübel, N. G. Johnson, B. Fischer, N. Camus, K. J. Betsch, O. Herrwerth, A. Senftleben, A. M. Sayler, T. Rathje, et al., "Attosecond tracing of correlated electron-emission in non-sequential double ionization," Nature Commun. **3**, 813 (2012).

[99] N. G. Johnson, O. Herrwerth, A. Wirth, S. De, I. Ben-Itzhak, M. Lezius, B. Bergues, M. F. Kling, A. Senftleben, C. D. Schröter, et al., "Single-shot carrier-envelope-phase-tagged ion-momentum imaging of nonsequential double ionization of argon in intense 4-fs laser fields," Phys. Rev. A **83**, 013412 (2011).

[100] C. F. de Morisson Faria, T. Shaaran, and M. T. Nygren, "Time-delayed nonsequential double ionization with few-cycle laser pulses: Importance of the carrier-envelope phase," Phys. Rev. A **86**, 053405 (2012).

[101] T. Shaaran, M. T. Nygren, and C. F. de Morisson Faria, "Laser-induced nonsequential double ionization at and above the recollision-excitation-tunneling threshold," Phys. Rev. A **81**, 063413 (2010).

[102] T. Shaaran and C. F. de Morisson Faria, "Laser-induced nonsequential double ionization: kinematicconstraints for the recollision-excitation-tunneling mechanism," J. Mod. Opt. **57**, 984 (2009).

[103] D. Bauer, D. B. Milosevic, and W. Becker, "Strong-field approximation for intense-laser atom processes: the choice of gauge," Phys. Rev. A **72**, 023415 (2008).

[104] M. F. Kling, J. Rauschenberger, A. J. Verhoef, E. Hasović, T. Uphues, D. B. Milošević, H. G. Muller, and M. J. J. Vrakking, "Imaging of carrier-envelope phase effects in above-threshold ionization with intense few-cycle laser fields," New J. Phys. **10**, 025024 (2008).

[105] P. Eckle, M. Smolarski, P. Schlup, J. Biegert, A. Staudte, M. Schöffler, H. G. Muller, R. Dörner, and U. Keller, "Attosecond angular streaking," Nature Phys. **4**, 565 (2008).

[106] W. C. Wallace, M. G. Pullen, D. E. Laban, O. Ghafur, H. Xu, A. J. Palmer, G. F. Hanne, K. Bartschat, A. N. Grum-Grzhimailo, H. M. Quiney, et al., "Carrier-envelope phase effects in above-threshold ionization of atomic hydrogen," New J. Phys. **15**, 033002 (2013).

[107] F. Anis and B. D. Esry, "Enhancement of carrier-envelope phase effects in photoexcitation of alkali atoms," J. Phys. B: At. Mol. Opt. Phys. **42**, 191001 (2009).

[108] V. Roudnev and B. D. Esry, "General Theory of Carrier-Envelope Phase Effects," Phys. Rev. Lett. **99**, 220406 (2007).

[109] M. Abel, T. Pfeifer, A. Jullien, P. M. Nagel, M. J. Bell, D. M. Neumark, and S. R. Leone, "Carrier-envelope phase-dependent quantum interferences in multiphoton ionization," J. Phys. B: At. Mol. Opt. Phys. **42**, 075601 (2009).

[110] N. G. Kling, K. J. Betsch, M. Zohrabi, S. Zeng, F. Anis, U. Ablikim, B. Jochim,

Z. Wang, M. Kübel, M. F. Kling, et al., "Carrier-envelope phase control over pathway interference in strong-field dissociation of H_2^+," Phys. Rev. Lett. **accepted** (2013).

[111] T. Rathje, A. M. Sayler, S. Zeng, P. Wustelt, H. Figger, B. D. Esry, and G. G. Paulus, "Coherent Control at Its Most Fundamental: Carrier-Envelope-Phase-Dependent Electron Localization in Photodissoziation of a H_2^+ Molecular Ion Beam Target," Phys. Rev. Lett. **111**, 093002 (2013).

[112] X. M. Tong and C. D. Lin, "Dynamics of Light-Field Control of Molecular Dissociation at the Few-Cycle Limit," Phys. Rev. Lett. **98**, 123002 (2007).

[113] S. Gräfe and M. Y. Ivanov, "Effective Fields in Laser-driven Electron Recollision and Charge Localization," Phys. Rev. Lett. **99**, 163603 (2007).

[114] F. Kelkensberg, G. Sansone, M. Y. Ivanov, and M. Vrakking, "A semi-classical model of attosecond electron localization in dissociative ionization of hydrogen," Phys. Chem. Chem. Phys. **13**, 8647 (2011).

[115] X. Urbain, B. Fabre, E. M. Staicu-Casagrande, N. de Ruette, V. M. Andrianarijaona, J. Jureta, J. H. Posthumus, A. Saenz, E. Baldit, and C. Cornaggia, "Intense-Laser-Field Ionization of Molecular Hydrogen in the Tunneling Regime and Its Effect on the Vibrational Excitation of H_2^+," Phys. Rev. Lett. **92**, 163004 (2004).

[116] I. Znakovskaya, P. von den Hoff, S. Zherebtsov, A. Wirth, O. Herrwerth, M. J. J. Vrakking, R. de Vivie-Riedle, and M. F. Kling, "Attosecond Control of Electron Dynamics in Carbon Monoxide," Phys. Rev. Lett. **103**, 103002 (2009).

[117] Y. Liu, X. Liu, Y. Deng, C. Wu, H. Jiang, and Q. Gong, "Selective Steering of Molecular Multiple Dissociative Channels with Strong Few-Cycle Laser Pulses," Phys. Rev. Lett. **106**, 073004 (2011).

[118] K. J. Betsch, N. G. Johnson, B. Bergues, M. Kübel, O. Herrwerth, A. Senftleben, I. Ben-Itzhak, G. G. Paulus, R. Moshammer, J. Ullrich, et al., "Controlled directional ion emission from several fragmentation channels of CO driven by a few-cycle laser field," Phys. Rev. A **86**, 063403 (2012).

[119] X. Xie, K. Doblhoff-Dier, S. Roither, M. S. Schöffler, D. Kartashov, H. Xu, T. Rathje, G. G. Paulus, A. Baltuška, S. Gräfe, et al., "Attosecond-recollision-controlled selective fragmentation of polyatomic molecules," Phys. Rev. Lett. **109**, 243001 (2012).

[120] A. Alnaser, K. J. Betsch, M. Kübel, R. Siemering, B. Bergues, N. G. Kling, Y. Deng, Z. A. Alahmed, A. M. Azzeer, R. Moshammer, et al., "Sub-femtosecond control of hydrogen-bond rearrangement," (in preparation).

[121] M. Kremer, B. Fischer, B. Feuerstein, V. L. B. de Jesus, V. Sharma, C. Hofrichter, A. Rudenko, U. Thumm, C. D. Schröter, R. Moshammer, et al., "Electron Localization in Molecular Fragmentation of H_2 by Carrier-Envelope Phase Stabilized Laser Pulses," Phys. Rev. Lett **103**, 213003 (2009).

[122] H. Xu, J.-P. Maclean, D. E. Laban, W. C. Wallace, D. Kielpinski, R. T. Sang, and I. V. Litvinyuk, "Carrier-envelope-phase-dependent dissociation of hydrogen," New J. Phys. **15**, 023034 (2013).

[123] T. Wittmann, B. Horvath, W. Helml, M. G. Schätzel, X. Gu, A. L. Cavalieri, G. G. Paulus, and R. Kienberger, "Single-shot carrier-envelope phase measurement of few-cycle laser pulses," Nature Phys. **5**, 357 (2009).

[124] A. T. J. B. Eppink and D. H. Parker, "Velocity map imaging of ions and electrons using electrostatic lenses: Application in photoelectron and photofragment ion imaging of molecular oxygen," Rev. Sci. Inst. **68**, 3477 (1997).

[125] C. Maharjan, Ph.D. thesis, Kansas State University (2007).

[126] R. Dörner, V. Mergel, L. Spielberger, M. Achler, K. Khayyat, T. Vogt, H. Bräuning, O. Jagutzki, T. Weber, J. Ullrich, et al., "Kinematically Complete Experiments Using Cold Target Recoil Ion Momentum Spectroscopy," Nucl. Inst. Meth. B **124**, 225 (1997).

[127] R. Dörner, V. Mergel, O. Jagutzki, L. Spielberger, J. Ullrich, R. Moshammer, and H. Schmidt-Böcking, "Cold Target Recoil Ion Momentum Spectroscopy: a momentum microscope to view atomic collision dynamics," Phys. Report **330**, 95 (2000).

[128] J. Ullrich, R. Moshammer, A. Dorn, R. Dörner, L. P. H. Schmidt, and H. Schmidt-Böcking, "Recoil-ion and electron momentum spectroscopy:reaction-microscopes," Rep. Prog. Phys. **66**, 1463 (2003).

[129] A. Staudte, Ph.D. thesis, Johann Wolfgang Goethe Universität (2005).

[130] RoentDek, "RoentDek Handels GmbH,", http://www.roentdek.com.

[131] I. Ben-Itzhak, P. Q. Wang, J. F. Xia, A. M. Sayler, M. A. Smith, K. D. Carnes, and B. D. Esry, "Dissociation and Ionization of H2+ by Ultrashort Intense Laser Pulses Probed by Coincidence 3D Momentum Imaging," Phys. Rev. Lett. **95**, 073002 (2005).

[132] P. Q. Wang, A. M. Sayler, K. D. Carnes, J. F. Xia, M. A. Smith, B. D. Esry, and I. Ben-Itzhak, "Dissociation of H_2^+ in intense femtosecond laser fields studied by coincidence three-dimensional momentum imaging," Phys. Rev. A **74**, 043411 (2006).

[133] W. Wolff, J. McKenna, R. Vácha, M. Zohrabi, B. Gaire, K. D. Carnes, and I. Ben-Itzhak, "Three-dimensional energy profile measurement of a molecular ion beam by coincidence momentum imaging compared to a retarding field analyzer," J. Inst. **5**, 10006 (2010).

[134] I. Ben-Itzhak, in *Fragmentation Processes Topics in Atomic and Molecular Physics*, edited by C. T. Whelan (Cambridge University Press, Cambridge, 2013).

[135] Z. Chang, *Fundamentals of Attosecond Optics* (Taylor and Francis Group, LLC, Boca Raton, 2011).

[136] E. Hecht, *Optics*, vol. 4nd Ed. (San Francisco: Pearson Education, Inc., 2002).

[137] T. Pfeifer and M. C. Downer, "Direct experimental observation of periodic intensity modulation along a straight hollow-core optical waveguide," Journal of the Opt. Soc. America B, **24**, 1025 (2007).

[138] L. Gallmann, T. Pfeifer, P. M. Nagel, M. J. Abel, D. M. Neumark, and S. R. Leone, "Comparison of the filamentation and the hollow-core fiber characteristics for pulse compression into the few-cycle regime," Appl. Phys. B **86**, 561 (2007).

[139] T. M. GmbH, "TEM Messtechnik GmbH,", http://www.tem-messtechnik.de.

[140] M. Trachy, Ph.D. thesis, Kansas State University (2008).

[141] Femtolasers, "FEMTOMETER Few cycle pulse characterization,", http://www.femtolasers.com/FEMTOMETER-TM.120.0.html.

[142] A. M. Sayler, T. Rathje, W. Müller, C. Kürbis, K. Rhle, G. Stibenz, and G. G. Paulus, "Real-time pulse length measurement of few-cycle laser pulses using above-threshold ionization," Opt. Exp. **19**, 4464 (2011).

[143] O. Optics, "Ocean Optics,", http://www.oceanoptics.com.

[144] A. Rudenko, T. Ergler, K. Zrost, R. Feuerstein, V. L. B. de Jesus, C. D. Schröter, R. Moshammer, and J. Ullrich, "Intensity-dependent transitions between different pathways of strong-field double ionization," Phys. Rev. A **78**, 015403 (2008).

[145] M. Busuladžić, A. Gazibegović-Busuladžić, and D. B. Milošević, "High-Order Above-Threshold Ionization in a Laser Field: Influence of the Ionization Potential on the High-Energy Cutoff," Laser Physics **16**, 289 (2006).

[146] S. Zherebtsov, F. Süßmann, C. Peltz, J. Plenge, K. J. Betsch, I. Znakovskaya, A. S. Alnaser, N. G. Johnson, M. Kübel, A. Horn, et al., "Carrierenvelope phase-tagged imaging of the controlled electron acceleration from SiO_2 nanospheres in intense few-cycle laser fields," New J. Phys. **14**, 075010 (2012).

[147] A. S. Alnaser, X. M. Tong, T. Osipov, S. Voss, C. M. Maharjan, B. Shan, Z. Chang, and C. L. Cocke, "Laser-peak-intensity calibration using recoil-ion momentum imaging," Phys. Rev. A **70**, 023413 (2004).

[148] C. Li, E. Moon, H. Mashiko, C. M. Nakamura, P. Ranitovic, C. M. Maharjan, C. L. Cocke, Z. Chang, and G. G. Paulus, "Precision control of carrier-envelope phase in grating based chirped pulse amplifiers," Opt. Exp. **14**, 11468 (2006).

[149] E. Moon, C. Li, Z. Duan, J. Tackett, K. L. Corwin, B. R. Washburn, and Z. Chang, "Reduction of fast carrier-envelope phase jitter in femtosecond laser amplifiers," Opt. Exp. **14**, 9758 (2006).

[150] Z. Chang, "Carrier-envelope phase shift caused by grating-based stretchers and compressors," Appl. Opt. **45**, 8350 (2006).

[151] S. Ghimire, B. Shan, C. Wang, and Z. Chang, "High-Energy 6.2-fs Pulses for Attosecond Pulse Generation," Laser Phys. **15**, 838 (2005).

[152] C. Li, E. Moon, H. Wang, H. Mashiko, C. Nakamura, J. Tackett, and Z. Chang, "Determining the Phase-Energy Coupling Coefficient in Carrier-envelope Phase Measurements," Opt. Lett. **32**, 796 (2007).

[153] H. Wang, C. Li, J. Tackett, H. Mashiko, C. Nakamura, E. Moon, and Z. Chang, "Power locking of high-repetition-rate chirped pulse amplifiers," Appl. Phys. B: Lasers Opt. **89**, 275 (2007).

[154] H. Mashiko, C. M. Nakamura, C. Li, E. Moon, H. Wang, J. Tackett, and Z. Chang, "Carrier-envelope phase stabilized 5.6 fs, 1.2 mJ pulses," Appl. Phys. Lett. **90**, 161114 (2007).

[155] M. Schultze, A. Wirth, I. Grguras, M. Uiberacker, T. Uphues, A. J. Verhoef, J. Gagnon, M. Hofstetter, U. Kleineberg, E. Goulielmakis, et al., "State-of-the-art attosecond metrology," J. Electron Spectros. Relat. Phenomena **184**, 68 (2011).

[156] N. G. Kling, J. McKenna, A. M. Sayler, B. Gaire, M. Zohrabi, U. Ablikim, K. D. Carnes, and I. Ben-Itzhak, "Charge asymmetric dissociation of a CO^+ molecular-ion beam induced by strong laser fields," Phys. Rev. A **87**, 013418 (2013).

[157] I. Ben-Itzhak, S. G. Ginther, and K. D. Carnes, "Multiple-electron removal and molecular fragmentation of CO by fast F^{4+} impact," Phys. Rev. A **47**, 2827 (1993).

[158] K. Wohrer, G. Sampoll, R. L. Watson, M. Chabot, O. Herber, and V. Horvat, "Dissociation of multicharged CO molecular ions produced in collisions with 97-MeV Ar^{14+}: Dissociation fractions and branching ratios," Phys. Rev. A **46**, 3929 (1992).

[159] K. Codling, L. J. Frasinski, and P. A. Hatherly, "On the field ionisation of diatomic molecules by intense laser fields," J. Phys. B: At. Mol. Opt. Phys. **22**, L321 (1989).

[160] N. Levasseur, P. Millie, P. Archirel, and B. Levy, "Bond formation between positively charged species. Non-adiabatic analysis and valence-bond model in the CO^{2+} case," Chem. Phys. **153**, 387 (1991).

[161] R. S. Mulliken, "Intensities of Electronic Transitions in Molecular Spectra II. Charge-Transfer Spectra," J. Chem. Phys. **7**, 20 (1939).

[162] I. Kawata, H. Kono, Y. Fujimura, and A. D. Bandrauk, "Intense-laser-field-enhanced ionization of two-electron molecules: Role of ionic states as doorway states," Phys. Rev. A **62**, 031401(R) (2000).

[163] D. M. Villeneuve, M. Y. Ivanov, and P. B. Corkum, "Enhanced ionization of diatomic molecules in strong laser fields: A classical model," Phys. Rev. A **54**, 736 (1996).

[164] R. Trebino, *Frequency-resolved optical gating: the measurement of ultrashort laser pulses* (Kluwer Academic Publishers, Norwell, Massachusetts, 2000).

[165] M. Lein, "Molecular imaging using recolliding electrons," J. Phys. B: At. Mol. Opt. Phys. **40**, R135 (2007).

[166] B. Gaire et al., "Molecular fragmentation below the n-photon dissociation threshold in strong laser fields," (in preparation).

[167] R. Polák and J. Čížek, "On the VB adiabaticdiabatic picture of bonding in CO^{2+}," J. Mol. Struct. **547**, 17 (2001).

[168] T. Šedivcová, P. R. Žd'ánská, V. Špirko, and J. Fišer, "Computed lifetimes of metastable states of CO^{2+}," J. Chem. Phys. **124**, 214303 (2006).

[169] K. Okada and S. Iwata, "Accurate potential energy and transition dipole moment curves for several electronic states of CO^{+}," J. Chem. Phys. **112**, 1804 (2000).

[170] L. D. Landau, "On the theory of transfer of energy at collisions II," Phys. Z. Sowjetunion **2**, 46 (1932).

[171] C. Zener, "Non-Adiabatic Crossing of Energy Levels," Proc. R. Soc. London, Ser. A **137**, 696 (1932).

[172] U. Ablikim et al., "Dissociation of CO^{+} molecular ions by strong laser fields," (in preparation).

[173] M. S. Child and M. Shapiro, "Photodissociation and the Condon reflection principle," Mol. Phys. **48**, 111 (1983).

[174] M. S. Child, H. Essén, and R. J. L. Roy, "An RKR-like inversion procedure for bound-continuum transition intensities," J. Chem. Phys. **78**, 6732 (1983).

[175] P. H. Krupenie and S. Weissman, "Potential-Energy Curves for CO and CO^+," J. Chem. Phys. **43**, 1529 (1965).

[176] K. P. Huber and G. Herzberg, *Molecular Spectra and Molecular Structure*, vol. IV Constants of Diatomic Molecules (Van Nostrand, Reinhold, 1979).

[177] C. Guo, "Holding molecular dications together in strong laser fields," Phys. Rev. A **73**, 041401 (2006).

[178] I. Ben-Itzhak, P. Q. Wang, A. M. Sayler, K. D. Carnes, M. Leonard, B. D. Esry, A. S. Alnaser, B. Ulrich, X. M. Tong, I. V. Litvinyuk, et al., "Elusive enhanced ionization structure for H_2^+ in intense ultrashort laser pulses," Phys. Rev. A **78**, 063419 (2008).

[179] D. J. Jones, S. A. Diddams, J. K. Ranka, A. S. Robert, S. Windeler, J. L. Hall, and S. T. Cundiff, "Carrier-Envelope Phase Control of Femtosecond Mode-Locked Lasers and Direct Optical Frequency Synthesis," Science **288**, 635 (2000).

[180] A. Wirth, M. T. Hassan, I. Grguraš, J. Gagnon, A. Moulet, T. T. Luu, S. Pabst, R. Santra, Z. A. Alahmed, A. M. Azzeer, et al., "Synthesized Light Transients," Science **334**, 195 (2011).

[181] O. D. Mücke, R. Ell, A. Winter, J. W. Kim, J. R. Birge, L. Matos, and F. X. Kärtner, "Self-Referenced 200 MHz Octave-Spanning Ti:Sapphire Laser with 50 Attosecond Carrier-Envelope Phase Jitter," Opt. Exp. **13**, 5163 (2005).

[182] S. Rausch, T. Binhammer, A. Harth, J. Kim, R. Ell, F. X. Kärtner, and U. Morgner, "Controlled waveforms on the single-cycle scale from a femtosecond oscillator," Opt. Exp. **16**, 9739 (2008).

[183] M. Nisoli, G. Sansone, S. Stagira, J.-P. Caumes, C. Vozzi, S. D. Silvestri, M. Pascolini, L. Poletto, P. Villoresi, and G. Tondello, "Single-atom effects in high-order harmonic generation: role of carrier-envelope phase in the few-optical-cycle regime," App. Phys. B **78**, 873 (2004).

[184] E. Gagnon, I. Thomann, A. Paul, A. L. Lytle, S. Backus, M. M. Murnane, H. C. Kapteyn, and A. S. Sandhu, "Long-term carrier-envelope phase stability from a grating-based, chirped pulse amplifier," Opt. Lett. **31**, 1866 (2006).

[185] M. Kakehata, H. Takada, Y. Kobayashi, K. Torizuka, H. Takamiya, K. Nishijima, T. Homma, H. Takahashi, K. Okubo, S. Nakamura, et al., "Carrier-envelope-phase stabilized chirped-pulse amplification system scalable to higher pulse energies," Opt. Exp. **12**, 2070 (2004).

[186] M. Nisoli, G. Sansone, S. Stagira, S. D. Silvestri, C. Vozzi, M. Pascolini, L. Poletto, P. Villoresi, and G. Tondello, "Effects of Carrier-Envelope Phase Differences of Few-Optical-Cycle Light Pulses in Single-Shot High-Order-Harmonic Spectra," Phys. Rev. Lett. **91**, 213905 (2003).

[187] P. Eckle, A. N. Pfeiffer, C. Cirelli, A. Staudte, R. Dörner, H. G. Muller, M. Büttiker, and U. Keller, "Attosecond Ionization and Tunneling Delay Time Measurements in Helium," Science **322**, 1525 (2008).

[188] B. Fischer, M. Kremer, T. Pfeiffer, B. Feuerstein, V. Sharma, U. Thumm, C. Hofrichter, A. Rudenko, U. Thumm, C. D. Schröter, et al., "Steering the Electron in H_2^+ by Nuclear Wave Packet Dynamics," Phys. Rev. Lett. **105**, 223001 (2010).

[189] M. F. Kling, C. Siedschlag, I. Znakovskaya, A. J. Verhoef, S. Zherebtsov, F. Krausz, M. Lezius, and M. J. J. Vrakking, "Strong-field Control of Electron Localization during Molecular Dissociation," Mol. Phys. **106**, 455 (2008).

[190] V. Roudnev and B. D. Esry, "HD^+ in a short strong laser pulse: Practical consideration of the observability of carrier-envelope phase effects," Phys. Rev. A **76**, 023403 (2007).

[191] P. Lan, E. J. Takahashi, and K. Midorikawa, "Efficient control of electron localization by subcycle waveform synthesis," Phys. Rev. A **86**, 013418 (2012).

[192] T. J. Yu, K. H. Hong, H. G. Choi, J. H. Sung, I. W. Choi, D. K. Ko, J. Lee, J. Kim, D. E. Kim, and C. H. Nam, "Precise and long-term stabilization of the carrier-envelope phase of femtosecond laser pulses using an enhanced direct locking technique," Opt. Exp. **15**, 8203 (2007).

[193] J. Rauschenberger, T. Fuji, M. Hentschel, A.-J. Verhoef, T. Udem, C. Gohle, T. W. Hänsch, and F. Krausz, "Carrier-envelope phase-stabilized amplifier system," Las. Phys. Lett. **3**, 37 (2006).

[194] L. Canova, X. Chen, A. Trisorio, A. Jullien, A. Assion, G. Tempea, N. Forget, T. Oksenhendler, and R. Lopez-Martens, "Carrier-envelope phase stabilization and control using a transmission grating compressor and an AOPDF," Opt. Lett. **34**, 1333 (2009).

[195] T. Rathje, N. G. Johnson, M. Möller, F. Süßmann, D. Adolph, M. Kübel, R. Kienberger, M. F. Kling, G. G. Paulus, and A. M. Sayler, "Review of attosecond resolved measurement and control via carrierenvelope phase tagging with above-threshold ionization," J. Phys. B: At. Mol. Opt. Phys. **45**, 074003 (2012).

[196] G. G. Paulus, F. Grasbon, H. Walther, P. Villoresi, M. Nisoli, S. Stagira, E. Priori, and S. D. Silvestri, "Absolute-phase phenomena in photoionization with few-cycle laser pulses," Nature **414**, 182 (2001).

[197] G. G. Paulus, "A Meter of the "Absolute" Phase of Few-Cycle Laser Pulses," Nature **15**, 843 (2005).

[198] M. Kübel, K. J. Betsch, N. G. Johnson, U. Kleineberg, R. Moshammer, J. Ullrich, G. G. Paulus, M. F. Kling, and B. Bergues, "Carrier-envelope-phase tagging in measurements with long acquisition times," New J. Phys. **14**, 093027 (2012).

[199] A. M. Sayler, T. Rathje, W. Müller, K. Rühle, R. Kienberger, and G. G. Paulus, "Precise, real-time, every-single-shot, carrier-envelope phase measurement of ultrashort laser pulses," Opt. Lett. **36**, 1 (2011).

[200] X. Liu, H. Rottke, E. Eremina, W. Sandner, E. Goulielmakis, K. O. Keeffe, M. Lezius, F. Krausz, F. Lindner, M. G. Schätzel, et al., "Nonsequential Double Ionization at the Single-Optical-Cycle Limit," Phys. Rev. Lett. **93**, 263001 (2004).

[201] S. Micheau, Z. Chen, A. T. Le, and C. D. Lin, "Quantitative rescattering theory for nonsequential double ionization of atoms by intense laser pulses," Phys. Rev. A **79**, 013417 (2009).

[202] P. Agostini and L. F. DiMauro, "The physics of attosecond light pulses," Rep. Prog. Phys. **67**, 813 (2004).

[203] B. Manschwetus, T. Nubbemeyer, K. Gorling, G. Steinmeyer, U. Eichmann, H. Rottke, and W. Sandner, "Strong Laser Field Fragmentation of H_2: Coulomb Explosion without Double Ionization," Phys. Rev. Lett. **102**, 113002 (2009).

[204] F. Süßmann, S. Zherebtsov, J. Plenge, N. G. Johnson, M. Kübel, A. M. Sayler, V. Mondes, C. Graf, E. Rühl, G. G. Paulus, et al., "Single-shot velocity-map imaging of attosecond light-field control at kilohertz rate," Rev. Sci. Instrum. **82**, 093109 (2011).

[205] G. Vitec, "GS Vitec," (2013), http://www.gsvitec.com.

[206] P. Agostini, F. Fabre, G. Mainfray, G. Petite, and N. K. Rahman, "Free-Free Transitions Following Six-Photon Ionization of Xenon Atoms," Phys. Rev. Lett. **42**, 1127 (1979).

[207] A. H. Zewail, "Femtochemistry. Past, present, and future," Pure Appl. Chem. **72**, 2219 (2000).

[208] H. Rabitz, R. de Vivie-Riedle, M. Motzkus, and K. Kompa, "Whither the Future of Controlling Quantum Phenomena?," Science **288**, 824 (2000).

[209] M. Shapiro and P. Brumer, "Coherent control of molecular dynamics," Rep. Prog. Phys. **66**, 859 (2003).

[210] P. von den Hoff, R. Siemering, M. Kowalewski, and R. de Vivie-Riedle, "Electron dynamics and its control in molecules: From diatomics to larger molecular systems," IEEE Journal of Selected Topics in Quantum Electronics **18**, 119 (2012).

[211] M. F. Kling, P. von den Hoff, I. Znakovskaya, and R. de Vivie-Riedle, "(Sub-)femtosecond control of molecular reactions via tailoring the electric field of light," Phys. Chem. Chem. Phys. pp. – (2013), URL http://dx.doi.org/10.1039/C3CP50591J.

[212] E. Eremina, X. Liu, H. Rottke, W. Sandner, M. G. Schätzel, A. Dreischuh, G. G. Paulus, H. Walther, R. Moshammer, and J. Ullrich, "Influence of Molecular Structure on Double Ionization of N_2 and O_2 by High Intensity Ultrashort Laser Pulses," Phys. Rev. Lett. **92**, 173001 (2004).

[213] N. Camus, B. Fischer, M. Kremer, V. Sharma, A. Rudenko, B. Bergues, M. Kübel, N. G. Johnson, M. F. Kling, T. Pfeifer, et al., "Attosecond Correlated Dynamics of Two Electrons Passing through a Transition State," Phys. Rev. Lett. **108**, 073003 (2012).

[214] R. Moshammer, J. Ullrich, B. Feuerstein, D. Fischer, A. Dorn, C. D. Schröter, J. R. C. L´opez-Urrutia, C. Höhr, H. Rottke, C. Trump, et al., "Strongly directed electron emission in non-sequential double ionization of Ne by intense laser pulses," J. Phys. B: At. Mol. Opt. Phys. **36**, L113 (2003).

[215] M. Kübel, N. G. Kling, K. J. Betsch, N. Camus, A. Kaldun, U. Kleineberg, I. Ben-Itzhak, R. R. Jones, G. G. Paulus, T. Pfeifr, et al., "Non-Sequential Double-Ionization of N_2 in a Near Single-Cycle Laser Pulse," Phys. Rev. A **88**, 023418 (2013).

[216] E. Goulielmakis, M. Uiberacker, R. Kienberger, A. Baltuska, V. Yakovlev, A. Scrinzi, T. Westerwalbesloh, U. Kleineberg, U. Heinzmann, M. Drescher, et al., "Direct Measurement of Light Waves," Science **305**, 1267 (2004).

[217] B. Feuerstein, R. Moshammer, D. Fischer, A. Dorn, C. D. Schröter, J. Deipenwisch, J. R. C. Lopez-Urrutia, C. Höhr, P. Neumayer, J. Ullrich, et al., "Separation of recollision mechanisms in nonsequential strong field double ionization of Ar: the role of excitation tunneling," Phys. Rev. Lett. **87**, 043003 (2001).

[218] R. Kopold, W. Becker, H. Rottke, and W. Sandner, "Routes to nonsequential double ionization," Phys. Rev. Lett. **85**, 3781 (2000).

[219] C. Huang, Y. Zhou, Q. Zhang, and P. Lu, "Contribution of recollision ionization to the cross-shaped structure in nonsequential double ionization," Opt. Exp. **21**, 11382 (2013).

[220] A. N. Pfeiffer, C. Cirelli, M. Smolarski, and U. Keller, "Recent attoclock measurements of strong field ionization," Chem. Phys. **414**, 84 (2013).

[221] G. N. Gibson, R. R. Freeman, and T. J. McIlrath, "Dynamics of the high-intensity multiphoton ionization of N_2," Phys. Rev. Lett. **67**, 1230 (1991).

[222] F. Grasbon, G. G. Paulus, S. L. Chin, H. Walther, J. Muth-Böhm, A. Becker, and F. H. M. Faisal, "Signatures of symmetry-induced quantum-interference effects observed in above-threshold-ionization spectra of molecules," Phys. Rev. A **63**, 041402 (2001).

[223] A. Talebpour, C.-Y. Chien, and S. L. Chin, "The effects of dissociative recombination in multiphoton ionization of O_2," J. Phys. B: At. Mol. Opt. Phys. **29**, L677 (1996).

[224] C. Guo, M. Li, J. P. Nibarger, and G. N. Gibson, "Single and double ionization of diatomic molecules in strong laser fields," Phys. Rev. A **58**, R4271 (1998).

[225] C. J. G. J. Uiterwaal, C. R. Gebhardt, H. Schröder, and K.-L. Kompa, "Predicting intense-field photoionization of atoms and molecules from their linear photoabsorption spectra in the ionization continuum," Eur. Phys. J. D **30**, 379 (2004).

[226] D. Zeidler, A. Staudte, A. B. Bardon, D. M. Villeneuve, R. Dörner, and P. B. Corkum, "Controlling Attosecond Double Ionization Dynamics via Molecular Alignment," Phys. Rev. Lett. **95**, 203003 (2005).

[227] A. Talebpour, S. Larochelle, and S. L. Chin, "Nonsequential Ionization of Atoms and Diatomic Molecules in Intense Laser Field," Las. Phys. **7**, 851 (1997).

[228] C. Guo and G. N. Gibson, "Ellipticity effects on single and double ionization of diatomic molecules in strong laser fields," Phys. Rev. A **63**, 040701(R) (2001).

[229] X. Wang and J. H. Eberly, "Elliptical trajectories in nonsequential double ionization," New J. Phys. **12**, 093047 (2010).

[230] L. B. Fu, G. G. Xin, D. F. Ye, and J. Liu, "Recollision Dynamics and Phase Diagram for Nonsequential Double Ionization with Circularly Polarized Laser Fields," Phys. Rev. Lett. **108**, 103601 (2012).

[231] S. De, I. Znakovskaya, D. Ray, F. Anis, N. G. Johnson, I. A. Bocharova, M. Magrakvelidze, B. D. Esry, C. L. Cocke, I. V. Litvinyuk, et al., "Field-Free Orientation of CO Molecules by Femtosecond Two-Color Laser Fields," Phys. Rev. Lett. **103**, 153002 (2009).

[232] H. Xu, T. Okino, K. Nakai, and K. Yamanouchi, in *Progress in Ultrafast Intense Laser Science VII*, edited by K. Yamanouchi, D. Charalambidis, and D. Normand (Springer, Heidelberg, 2011).

[233] T. Osipov, C. L. Cocke, M. H. Prior, A. Landers, T. Weber, O. Jagutzki, L. Schmidt, H. Schmidt-Böcking, and R. Dörner, "Photoelectron-Photoion Momentum Spectroscopy as a Clock for Chemical Rearrangements: Isomerization of the Di-Cation of Acetylene to theVinylidene Configuration," Phys. Rev. Lett. **90**, 233002 (2003).

[234] A. Hishikawa, A. Matsuda, M. Fushitani, and E. J. Takahashi, "Visualizing Recurrently Migrating Hydrogen in Acetylene Dication by Intense Ultrashort Laser Pulses," Phys. Rev. Lett. **99**, 258302 (2007).

[235] M. E.-A. Madjet, Z. Li, and O. Vendrell, "Ultrafast hydrogen migration in acetylene cation driven by non-adiabatic effects," J. Chem. Phys. **138**, 094311 (2013).

[236] Y. H. Jiang, A. Rudenko, O. Herrwerth, L. Foucar, M. Kurka, K. U. Kühnel, M. Lezius, M. F. Kling, J. van Tilborg, A. Belkacem, et al., "Ultrafast Extreme Ultraviolet Induced Isomerization of Acetylene Cations," Phys. Rev. Lett. **105**, 263002 (2010).

[237] A. S. Alnaser, I. Litvinyuk, T. Osipov, B. Ulrich, A. Landers, E. Wells, C. M. Maharjan, P. Ranitovic, I. Bocharova, D. Ray, et al., "Momentum-imaging investigations of the dissociation of D_2^+ and the isomerization of acetylene to vinylidene by intense short laser pulses," J. Phys. B: At. Mol. Opt. Phys. **39**, S485 (2006).

[238] T. S. Zyubina, Y. A. Dyakov, S. H. Lin, A. D. Bandrauk, and A. M. Mebel, "Theoretical study of isomerization and dissociation of acetylene dication in the ground and excited electronic states," J. Chem. Phys. **123**, 134320 (2005).

[239] D. Mathur, K. Dota, A. K. Dharmadhikari, and J. A. Dharmadhikari, "Carrier-Envelope-Phase Effects in Ultrafast Strong-Field Ionization Dynamics of Multielectron Systems: Xe and CS_2," Phys. Rev. Lett. **110**, 083602 (2013).

[240] V. Roudnev and B. D. Esry, "HD^+ photodissociation in the scaled coordinate approach," Phys. Rev. A **71**, 013411 (2005).

[241] F. Lindner, G. G. Paulus, H. Walther, A. Baltuška, E. Goulielmakis, M. Lezius, and F. Krausz, "Gouy Phase Shift for Few-Cycle Laser Pulses," Phys. Rev. Lett. **92**, 113001 (2004).

[242] R. N. Zare, "Dissociation of H_2^+ by Electron Impact: Calculated Angular Distribution," J. Chem. Phys. **47**, 204 (1967).

[243] A. M. Sayler, P. Q. Wang, K. D. Carnes, B. D. Esry, and I. Ben-Itzhak, "Determining laser-induced dissociation pathways of multielectron diatomic molecules: Application to the dissociation of O_2^+ by high-intensity ultrashort pulses," Phys. Rev. A **75**, 063420 (2007).

[244] A. Hishikawa, S. Liu, A. Iwasaki, and K. Yamanouchi, "Light-induced multiple electronic-state coupling of O_2^+ in intense laser fields," J. Chem. Phys. **114**, 9856 (2001).

[245] J. McKenna, A. M. Sayler, F. Anis, B. Gaire, N. G. Johnson, E. Parke, J. J. Hua, H. Mashiko, C. M. Nakamura, E. Moon, et al., "Enhancing High-Order Above-Threshold Dissociation of H_2^+ Beams with Few-Cycle Laser Pulses," Phys. Rev. Lett. **100**, 133001 (2008).

[246] F. Anis, T. Cackowski, and B. D. Esry, "Rotational dynamics of dissociating H_2^+ in a short intense laser pulse," J. Phys. B: At. Mol. Opt. Phys. **42**, 091001 (2009).

[247] S. Manzhos and H.-P. Loock, "Photofragment image analysis using the Onion-Peeling Algorithm," Comp. Phys. Commun. **154**, 76 (2003).

[248] V. Dribinski, A. Ossadtchi, V. A. Mandelshtam, and H. Reisler, "Reconstruction

of Abel-transformable images: The Gaussian basis-set expansion Abel transform method," Rev. Sci. Inst. **73**, 2634 (2002).

[249] N. G. Kling, D. Paul, A. Gura, G. Laurent, H. Li, Z. Wang, S. De, B. Ahn, C. H. Kim, T. K. Kim, et al., "Thick-lens velocity-map imaging spectrometer with high resolution suited for kilo-electronvolt charged particle detection," Rev. Sci. Instrum. **submitted** (2013).

[250] S. De, I. A. Bocharova, M. Magrakvelidze, D. Ray, W. Cao, B. Bergues, U. Thumm, M. F. Kling, I. V. Litvinyuk, and C. L. Cocke, "Tracking nuclear wave-packet dynamics in molecular oxygen ions with few-cycle infrared laser pulses," Phys. Rev. A **82**, 013408 (2010).

[251] C. J. Joachain, N. J. Kylstra, and R. M. Potvliege, *Atoms in Intense Laser Fields* (Cambridge University Press, Cambrigde, 2012).

[252] P. Colosimo, G. Doumy, C. I. Blaga, J. Wheeler, C. Hauri, F. Catoire, J. Tate, R. Chirla, A. M. March, G. G. P. H. G. Muller, et al., "Scaling strong-field interactions towards the classical limit," Nature **4**, 386 (2008).

[253] C. I. Blaga, J. Xu, A. D. DiChiara, E. Sistrunk, K. Zhang, P. Agostini, T. A. Miller, L. F. DiMauro, and C. D. Lin, "Imaging ultrafast molecular dynamics with laser-induced electron diffraction," Nature **483**, 194 (2012).

[254] D. A. Dahl, J. E. Delmore, and A. D. Appelhans, "SIMION PC/PS2 electrostatic lens design program," Rev. Sci. Inst. **61**, 607 (1990).

[255] SIMION, "SIMION Industry standard charged particle optics simulation software.,", http://simion.com/.

[256] F. Fabre, G. Petite, P. Agostini, and M. Clement, "Multiphoton above-threshold ionisation of xenon at 0.53 and 1.06 μm," J. Phys. B: At. Mol. Phys. **15**, 1353 (1982).

[257] T. J. McIlrath, P. H. Bucksbaum, R. R. Freeman, and M. Bashkansky, "Above-threshold ionization processes in xenon and krypton," Phys. Rev. A **35**, 4611 (1987).

[258] G. H. für Schwerionenforschung, "New GSI Analysis System GO4,", http://www-win.gsi.de/go4/.

[259] Photonis, "Photonis,", http://www.photonis.com.

[260] T. Osipov, Ph.D. thesis, Kansas State University (2003).

[261] A. Senftleben, Ph.D. thesis, Ruperto-Carola University of Heidelberg (2009).

[262] G. G. Paulus, "Attosecond double-slit experiment,", http://faculty.physics.tamu.edu/ggp/.

[263] Mathworks, "Matlab The Language of Technical Computing,", http://www.mathworks.com/products/matlab/.

Appendix A

Electronics

To illustrate the electronics used in the experiments presented in this thesis the phase-tagged COLTRIMS setup is described here. As the detectors are the same for the phase-tagged COLTRIMS (in Garching, Germany) and LIMDI (in JRM lab) setups, the electronics are very similar, and often times, the same units are used in both cases. The coincidence imaging detectors used in the COLTRIMS and LIMDI apparatuses consist of a stack of two microchannel plates (MCP) in a chevron configuration with a delay line anode, available commercially from Roentdek [130]. A photo of the ion detector (and a guide for the labeling), is shown in Fig. A.2, and a schematic of the electronics for the ion and electron detectors are shown in Fig. A.3 and Fig. A.4, respectively. The focus of the discussion here will be on the ion detector.

The detectors are built on a vacuum flange with feedthrough connections to the outside. These feedthroughs provide both the needed power and signal pick-off connections for the delay-line wires and the MCP. To pick off the signal, the power supply connection is part of a resistor-capacitor (RC) circuit — the basis for a decoupling box. A simple example schematic of a decoupling box (used to pick off the phase meter anode signal) is shown in Fig. A.1. For the MCP, at the output of the decoupling box, a small positive voltage signal with a fast rise time is produced. For the delay line wires, the voltage signal is negative.

In order to trigger the amplifier, the signals must be negative, so an inverter follows the decoupling box picking the MCP signal. The amplifier (Ortec FTA820) boosts the

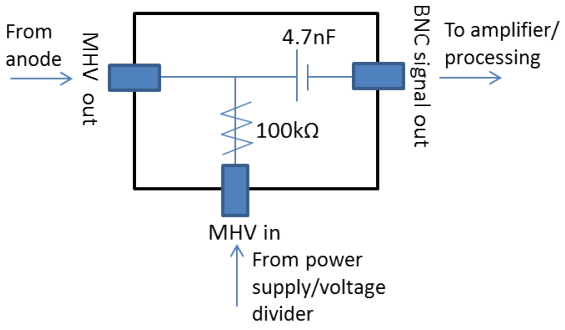

Figure A.1: Schematic of a decoupling box and its connections. Note that this is the design used for the phase meter, but the concept is the same for the detectors of the COLTRIMS and LIMDI setups.

signal (MCP and delay-line wires) strengths by a factor of 200 (*i.e.* 2 mV signals become 400 mV signals). With such a signal, the constant fraction discriminator (CFD) can be triggered. The CFD (Ortec 935 or Phillips Scientific 715) helps to clean the pulse from noise by requiring a certain threshold, and, more importantly, it determines the trigger times independent from the peak heights of the signal. This reduces time walk, and therefore allows for better time resolutions.

After the CFD, the signals are fed into a time-to-digital converter (TDC). The photodiode signal measuring "time zero" is also fed into channel zero of the TDC (C.A.E.N. V1290N), which allows for subtracting the jitter on the signals. The resolution provided by the TDC is 25 ps. A delayed photodiode signal (using a SRS DG635) provides the trigger signal for the TDC, which operates in common stop mode. The TDC signals are then sent to the computer through an ethernet connection (in JRM, the connection is provided by a fiber optic cable).

As the data acquisition (Go4 [258]) was slow for this setup, trying to collect all of the signals caused the program to crash. Therefore, a coincidence logic box (CO 4001) was incorporated into the electronics scheme to pre-select the signals that came with a laser pulse and registered on the MCP. This logic lowered the rate of data flowing to the computer to a level that the data acquisition could handle. Note that the data acquisition (SpecTcl) used

in the JRM lab did not have this problem.

The electronics for the phase meter (see Fig. A.5) are somewhat different than that for the COLTRIMS. The detectors consist of a chevron stack of MCPs with a metal anode from Photonis [259]. They are mounted on vacuum flanges with feedthroughs for power and the anode signal is picked off. Only the anode has a decoupling box. The anode signal then goes to a home-built device, referred to as the "mouse-piano box." Here the signal from the detector is divided up into two regions, decided by user-set gates. Each region is integrated, much like a box-car integrator unit would do. Then fast logic computes the asymmetry in the signal on the "left" and "right" detector in the two gated regions: $A_{1,2} = (L_{1,2} - R_{1,2}) / (L_{1,2} + R_{1,2})$ and outputs them as a voltage level between 0 and 4 V, which is read by an analog-to-digital converter (ADC, C.A.E.N. V785N). Specifically, a voltage of 0 corresponds to an asymmetry of -1, while a voltage of 4 V corresponds to an asymmetry of 1. The voltage level needs about 50 μs to saturate before it can be read by the ADC.

For completeness, the electronic diagram for the LIMDI setup is shown in Fig. A.6, and the electronic diagram for the phase meter (in JRML) used with the LIMDI setup is shown in Fig. A.7.

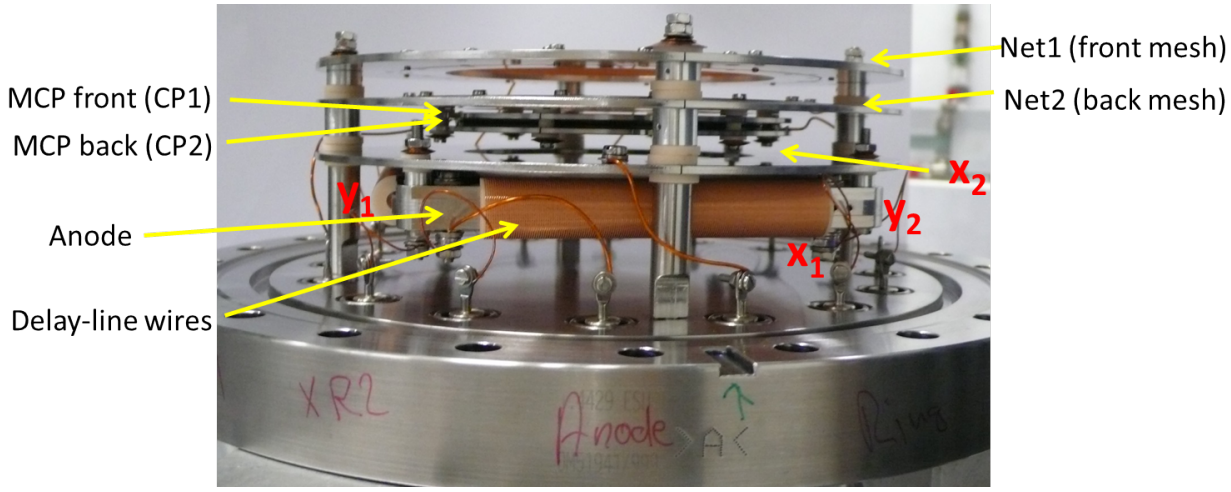

Figure A.2: Photo of the ion detector for the phase-tagged COLTRIMS in Germany.

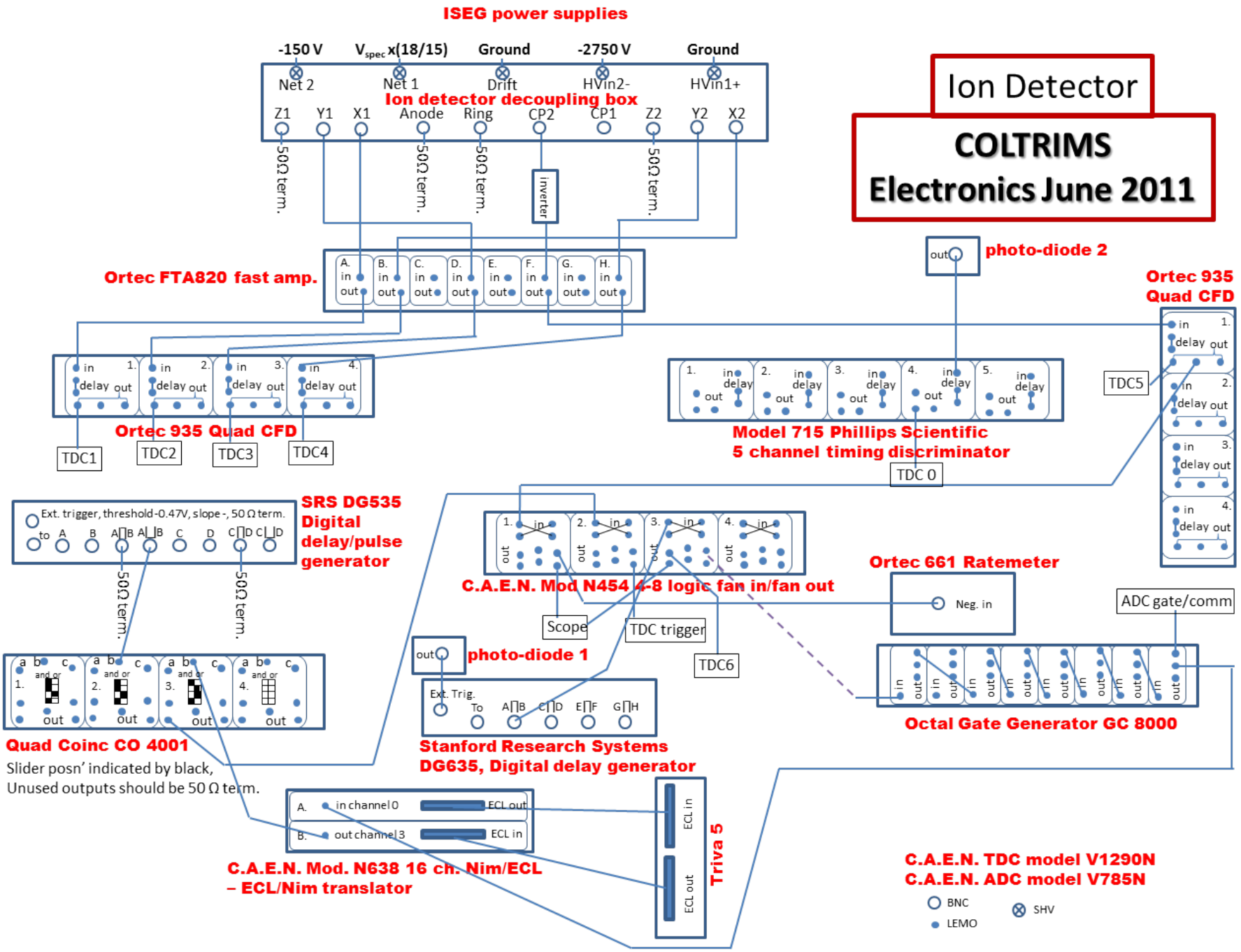

Figure A.3: Electronics and connections for the COLTRIMS ion detector.

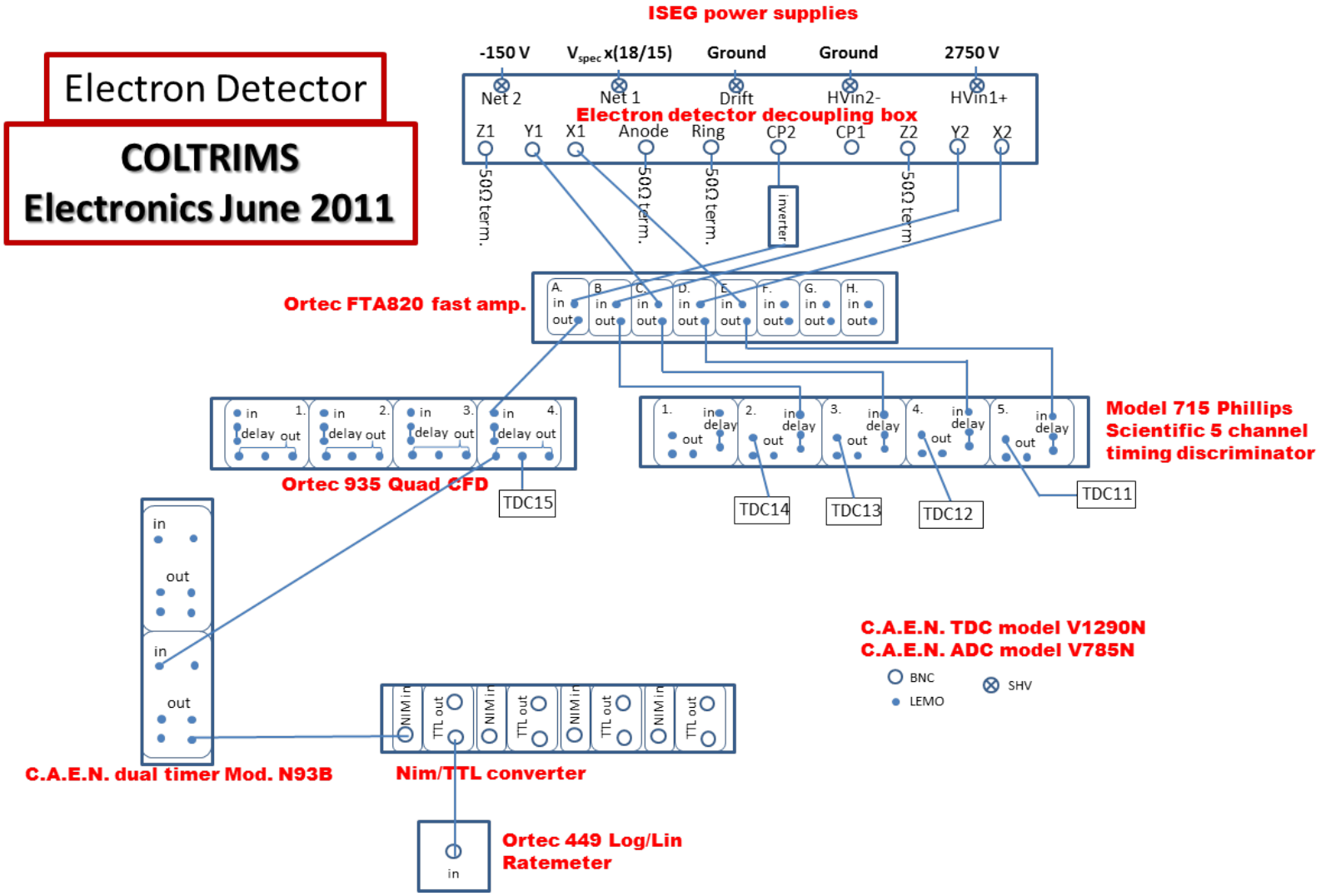

Figure A.4: Electronics and connections for the COLTRIMS electron detector.

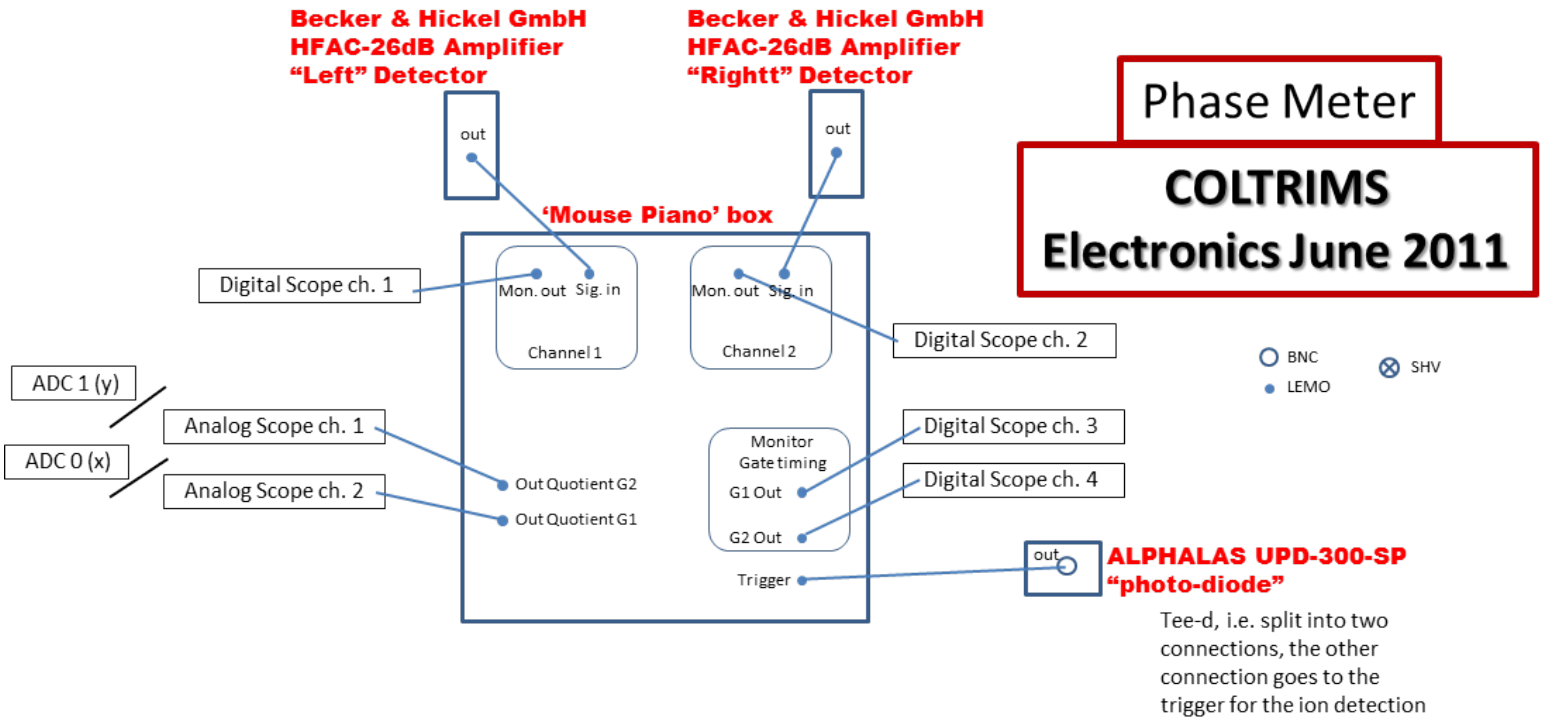

Figure A.5: Electronics and connections for the phase meter used with the COLTRIMS setup.

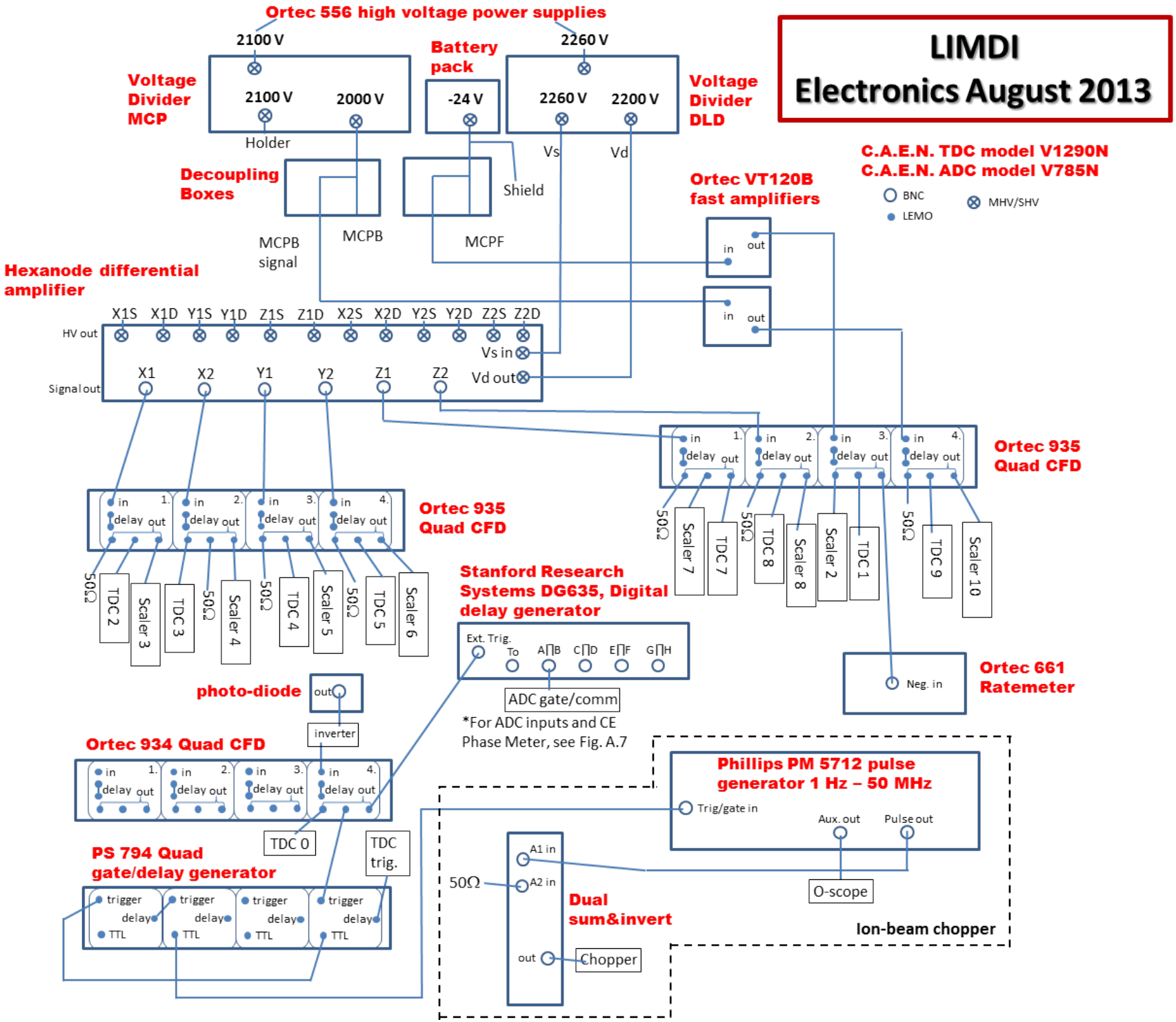

Figure A.6: Electronics and connections for the LIMDI setup.

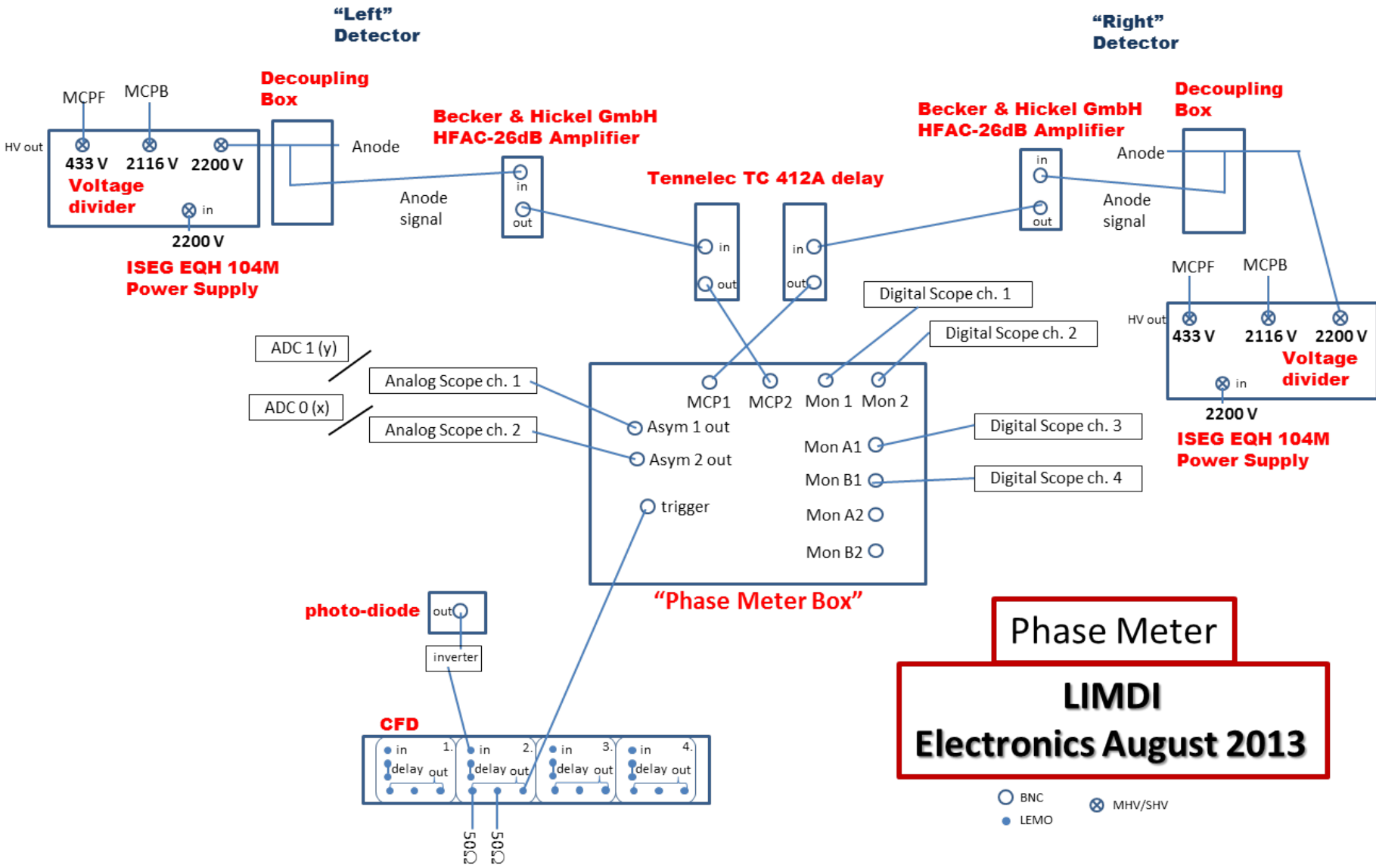

Figure A.7: Electronics and connections for the phase meter used with the LIMDI setup.

Appendix B

Imaging

In this Appendix, a synopsis of the 3D imaging formulation is given for the COLTRIMS and LIMDI methods for completeness. As these methods are well documented in previous theses and papers, the description here will be brief, and references will be referred to, where relevant. Thus a simplified version of the actual imaging equations are used to illustrate the imaging concepts.

B.1 COLTRIMS

Details for the 3D momentum imaging using COLTRIMS can be found, for example, in Refs. [125, 127–129, 260, 261]. A schematic of the COLTRIMS is shown in Fig. B.1, along with a definition of the coordinates used in this Section. An electric field is provided by the spectrometer, which extends nearly the entire path from the interaction region to the detectors, except for a small region between the meshes and the detectors. When electrons are being measured, a magnetic field along the spectrometer axis is used to confine them. The ions and electrons are detected on microchannel plate (MCP) detectors with delay-line anodes.

The time-of-flight, t_j [where the subscript j represents either an ion (i) or electron (e)] is given by the difference between the arrival time of a particle on the MCP (t_{MCP}) and the

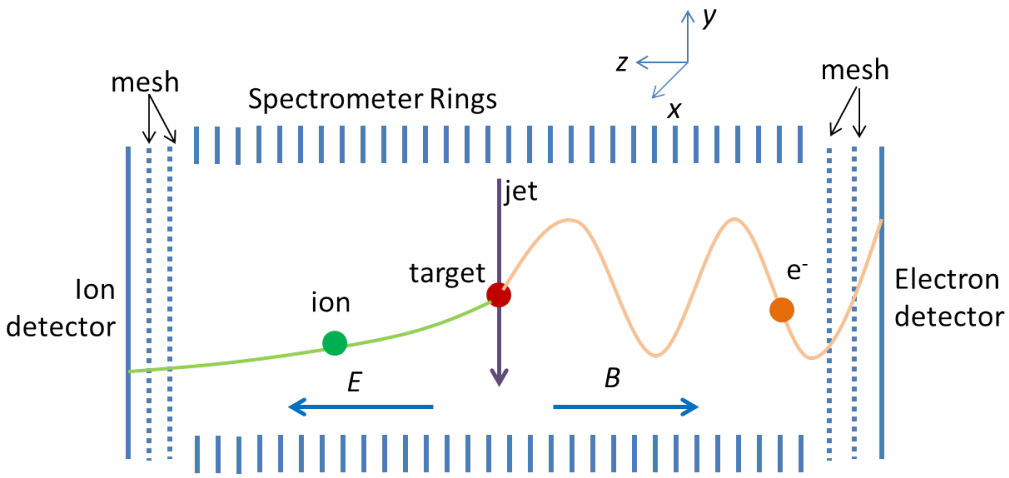

Figure B.1: Schematic of the COLTRIMS setup in Garching.

signal generated when a laser pulse illuminates a photodiode (t_{laser})

$$t_j - t_0 = t_{MCP} - t_{laser}. \tag{B.1}$$

The position signals come from the delay line wires. For a single delay-line wire, the position is recovered from the time difference between the signals arriving at the two ends, for the x-wire, $x_{1,2}$ (see Fig. A.2).

$$x_j - x_0 = (t_{x_1} - t_{x_2})c_x \tag{B.2a}$$

$$y_j - y_0 = (t_{y_1} - t_{y_2})c_y, \tag{B.2b}$$

where $c_{x,y}$ are constants that relate to the speed of the signals propagating through the wires. These timing signals include the propagation time through the electronics, which are accounted for in the offset variables t_0, x_0, and y_0. The position offsets are set such that x and y are relative to the center of the image on the detector. Therefore, the momenta in the x- and y-directions are centered around zero. The time offset is also adjusted such that the momentum in the z-direction is centered around zero. Note that the thermal motion is neglected as it is expected to be small for a supersonic jet [125].

B.1.1 Ion Imaging

Ions generated though laser interaction with a jet of neutral atoms or molecules are accelerated by the static electric field provided by the COLTRIMS spectrometer. Here we assume that the electric field is only along the spectrometer axis (z-direction), and is homogeneous all the way to the detector. In reality small corrections are needed to account for the region between the mesh and the detector. From the measured t_i, x_i, y_i, and the geometry of the COLTRIMS setup, the momentum of an ion in the lab frame can be evaluated with the following simplified equations.

$$p_x = m_i \frac{x_i - x_0}{t_i} \tag{B.3}$$

$$p_y = m_i \frac{y_i - y_0}{t_i} \tag{B.4}$$

$$p_z = \frac{m_i l_i}{t_i - t_0} - \frac{qE(t_i - t_0)}{2}. \tag{B.5}$$

Here m_i is the mass of the ion, x_0, y_0, and t_0 are the position and time of flight, for a given species, at the center of its distribution. The length from the interaction region to the detector is l_i, the charge of the ion is q, and the electric field strength of the COLTRIMS spectrometer is E.

The total momentum is calculated as

$$p_{tot} = \sqrt{p_x^2 + p_y^2 + p_z^2}, \tag{B.6}$$

and the kinetic energy is calculated as

$$KE = p_{tot}^2 / 2m_i. \tag{B.7}$$

When molecules break into two ionic fragments, they can be measured in coincidence. In this case, it helps to write the imaging equations in the center-of-mass (CM) frame such that the momentum conservation relation can be used to eliminate unknowns from the

equations (see, for example, Ref. [260] for more details). Alternatively, selecting fragment pairs with $p_{cm} = p_1 + p_2$ close to zero (in the lab frame) can help to clean the data from random coincidences. For ion pairs, the kinetic energy release (KER) is calculated from the momentum of one particle.

$$KER = p_{tot}^2/2\mu \tag{B.8}$$

where μ is the reduced mass of the nuclei. Furthermore, the angle between the dissociation direction and the laser polarization is calculated, assuming the axial-recoil approximation,

$$cos\theta = p_z/p_{tot}. \tag{B.9}$$

B.1.2 Electron Imaging

In order to increase the collection angle of the electrons, an axial magnetic field is used. This magnetic field does not have much influence on the ions, therefore it only calls for small corrections to the ion imaging formulas [261]. However, the formulas for imaging the electrons are somewhat more complex as the electrons are substantially affected by the magnetic field. The cyclotron frequency, $\omega_c = eB/m_e$ — the angular frequency of the electron in the magnetic field, B, in the x-y plane (see Fig. B.1) — is needed to calculate the electron momenta, which can be determined from the data [125, 260]. Again, assuming the electric field provided by the spectrometer is uniform and along z, the electron momenta in the lab frame are (see, for example, Ref. [125]):

$$p_x = \frac{m_e\omega_c}{2}[(x_e - x_{0e})\cos(\frac{\omega_c(t_e - t_{0e})}{2} + (y_e - y_{0e}))], \tag{B.10}$$

$$p_y = \frac{m_e\omega_c}{2}[(y_e - y_{0e})\cos(\frac{\omega_c(t_e - t_{0e})}{2} + (x_e - x_{0e}))], \tag{B.11}$$

and

$$p_z = \frac{m_e l_e}{(t_e - t_{0e})} - \frac{eE(t_e - t_{0e})}{2}. \tag{B.12}$$

Here l_e is the length from the interaction region to the electron detector, and m_e, e, and t_e are the respective mass, charge, and time of flight of the electron. And, again, the offsets,

t_{0e}, x_{0e}, and y_{0e} have been introduced to account for the signal propagation through the electronics.

The COLTRIMS method is a powerful technique when electrons and ions from the same atom or molecule are measured in coincidence. When this is the case, again, it is best to write the equations in the CM frame such that momentum conservation can be invoked to help clean the data from background. For example, for single ionization, when the momentum (each dimension separately) of the ion and electron are plotted as a 2D spectrum, a line forms for the true events which is centered around zero (assuming the offsets are accounted for properly) and $p_i = -p_e$.

B.2 LIMDI

Details for the 3D momentum imaging using the LIMDI method can be found, for example, in Refs. [52, 58, 131, 132, 134]. A schematic picture for the LIMDI setup is shown in Fig. B.2. Here we require that two particles are measured in coincidence. Thus, the indexing in this Section differs from the COLTRIMS imaging Section in that the subscript numbers 1 and 2 (denoted by j in some places) refer to the first and second particles which hit the detector. In the LIMDI experiments, the true time of the particles are measured, accessible via the measurement of the photon peak, described in Section 2.2.

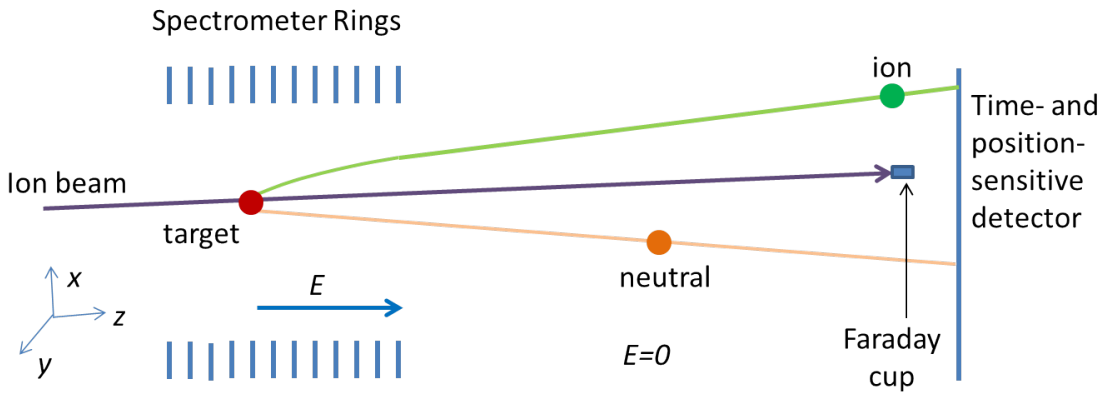

Figure B.2: Schematic of the LIMDI setup.

The true time t_j it takes for a fragment generated in the interaction region ($t_{interaction}$) to reach the detector (t_{MCP}), is:

$$t_j = t_{MCP} - t_{interaction}. \tag{B.13}$$

The position signals come from the delay line wires.

$$x_j = (t_L - t_R)c_x \tag{B.14a}$$

$$y_j = (t_U - t_D)c_y \tag{B.14b}$$

Here t_L, t_R, t_U, t_D are the timing signals from the ends of the x and y wires [52].

It is instructive to first consider the 3D LIMDI method with no voltage applied to the spectrometer, as is the case in "field-free imaging." We define the z-axis to be along the ion-beam direction (see Fig. B.2). The x,y origin is defined to be in the center of the beam spot on the imaging detector, and the z origin is where the laser-molecular ion interaction occurred. Using the x variable as an example (the equations are the same for the y variable), the displacement of the two fragments are

$$x_1 - x_{0i} = (v_{0xi} + v'_{1x})t_1 \tag{B.15a}$$

$$x_2 - x_{0i} = (v_{0xi} + v'_{2x})t_2, \tag{B.15b}$$

where x_{0i} is the position where a specific molecule fragmented, v_{0xi} is its center-of-mass (CM) velocity component, and v'_{1x} and v'_{2x} are the x velocities of each fragment in the CM system. The two dissociation velocities are linked by momentum conservation in the CM system, explicitly:

$$m_1 v'_{1x} + m_2 v'_{2x} = 0, \tag{B.16}$$

where m_1 and m_2 are the masses of the first and second fragment.

This set of three equations (B.15a, B.15b, and B.16) has four unknown variables: v'_{1x}, v'_{2x}, v_{0xi}, and x_{0i}. Therefore, one variable must be eliminated in order to be able to solve for the others. In our case, the interaction volume is small, so we approximate x_{0i} as zero.

We use eqn. B.16 to solve for v'_{2x}, to get

$$v'_{2x} = -\frac{m_1}{m_2} v'_{1x}, \tag{B.17}$$

which is substituted into eqn. B.15b and subtracted from eqn. B.15a, to finally get the solution for v'_{1x}

$$v'_{1x} = \frac{x_1 - x_2}{t_1 + \beta t_2} + \frac{v_{0xi}(t_2 - t_1)}{t_1 + \beta t_2}. \tag{B.18}$$

Here $\beta \equiv \frac{m_1}{m_2}$, the mass ratio of the fragments. The solution for v_{0xi} is

$$v_{0xi} = \frac{1}{1+\beta}[\frac{x_2}{t_2} + \beta \frac{x_1}{t_1}]. \tag{B.19}$$

The z component is evaluated using the flight times, given by

$$t_1 = \frac{d - z_i}{v_{0zi} + v'_{1z}} \tag{B.20a}$$

$$t_2 = \frac{d - z_i}{v_{0zi} + v'_{2z}}, \tag{B.20b}$$

where d is the distance from the interaction region to the detector, z_i is the location of the dissociation of a specific molecular ion within the interaction volume, and v_{0zi} is the beam velocity of each molecule. Due to the spread in beam energy, the range of v_{0zi} is much larger than that for the x and y velocity components. From momentum conservation we get the relationship between the dissociation velocity of the two fragments in the CM frame:

$$m_1 v'_{1z} + m_2 v'_{2z} = 0. \tag{B.21}$$

Similar to case for the x component (described above), there are four unknowns and only three equations. Thus, we replace z_i with its average value, $\overline{z_i}$ such that the solutions for v'_{1z} and v_{0zi} are

$$v'_{1z} = \frac{1}{1+\beta}(\frac{d - \overline{z_i}}{t_1} - \frac{d - \overline{z_i}}{t_2}) \tag{B.22}$$

and

$$v_{0zi} = \frac{1}{1+\beta}(\frac{\beta(d - \overline{z_i})}{t_1} - \frac{d - \overline{z_i}}{t_2}). \tag{B.23}$$

We determine the value of $\overline{z_i}$ by imposing reflection symmetry for the v'_{1z} distribution.

With the velocity components known, the momentum can be calculated by

$$p_{1x} = m_1 v'_{1x} = p_{2x} \tag{B.24a}$$

$$p_{1y} = m_1 v'_{1y} = p_{2y} \tag{B.24b}$$

$$p_{1z} = m_1 v'_{1z} = p_{2z}. \tag{B.24c}$$

The measurables, p_{tot}, KER and cosθ are evaluated by substituting these momentum values into equations B.6, B.8, and B.9, respectively.

By adding a weak electric field via the spectrometer, the ionic fragments are separated by their charge to energy ratio. The longitudinal field does not affect the transverse components, besides the small effect of fringe fields which are corrected for by treating them as "magnification factors" (see discussion in Ref. [52]). In addition, a small misalignment between the velocity of the ion beam and the spectrometer axis is corrected for by symmetrizing the data — where the average beam velocities, v_{0x} and v_{0y}, are accounted for.

This leaves the z component, which we model as:

$$t_1 = \frac{2d_1}{v_{0zi}} \frac{1}{\eta_1} [\sqrt{(1+u_{1z})^2 + \eta_1(1-z'_i)} - (1+u_{1z})] + \frac{d_2}{v_{0zi}} \frac{1}{\sqrt{(1+u_{1z})^2 + \eta_1(1-z'_i)}}. \tag{B.25}$$

Using SIMION [255], we verified that the model formula has an accuracy within the time resolution of the experiment. In equation B.25 d_1 is the length from the interaction region to the end of the spectrometer and d_2 is the length from the end of the spectrometer to the detector. Also, a couple of scaled parameters are introduced, namely the scaled location of the fragmentation, $z'_i \equiv z_i/d_1$, the scaled dissociation velocity of the first fragment in the CM system, $u_{1z} \equiv v'_{1z}/v_{0zi}$, and finally $\eta_1 \equiv 0.8qV_s/0.5m_1 v^2_{0zi}$, where V_s is the spectrometer voltage and q is the charge of the ion. To solve for the v'_{1z} and v_{0zi} velocities requires making the approximation (as in field-free imaging) that z_i is replaced by its average value, $\overline{z_i}$. Then the equations B.25, B.20b, and B.21 are solved numerically.

Appendix C

Phase Meter Design

An overview of the design of the single-shot sterographic-above threshold ionization (ATI) phase meter in the JRM lab is given in this Appendix. Using this device, one can measure the carrier envelope phase (CEP) of each and every laser shot [123]. When used in combination with another single-shot detection device, the relative CEP of the laser pulses can be tagged [99].

C.1 Apparatus

A top view drawing of the phase meter (cut through the center of the flight tubes) is shown in Fig. C.1. The basic components are the high vacuum chamber, the gas cell (located in the center), two detectors, a μ-metal shield, and a turbo pump. The basic premise of the apparatus is to ionize xenon atoms with a strong field laser and detect the number of electrons traveling to the "left" and "right" along the laser polarization axis. Thus, a laser beam, focused by an f =25 cm mirror, is directed into a gas cell containing xenon at about 10^{-3} Torr. The light enters the chamber through a 1 mm thick ultraviolet (UV)-grade fused silica window. A second window, located at the exit of the chamber, allows both for alignment of the laser through the chamber and a place for a photodiode. Typically, the laser power required by the phase meter is between 25 and 40 μJ/pulse, depending slightly on the pulse duration, to get a sufficient number (hundreds) of high energy electrons for each laser shot.

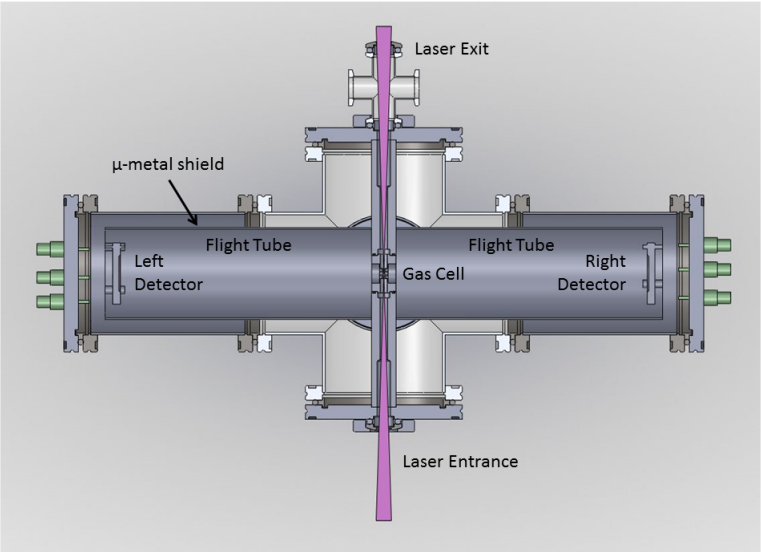

Figure C.1: Technical top-view drawing of the phase-meter apparatus, cut through the center of the flight tubes.

The density of the xenon gas inside the cell is also important. The pressure is balanced such that a sufficient number of electrons are detected, while the overall chamber pressure remains low enough for safe operation of the MCP detectors. The pressure is monitored by an ion gauge located between the turbo-molecular pump and the gas cell. The base pressure is typically in the low 10^{-7} Torr range. Under operating conditions, the pressure at the ion gauge is between 1 and 2×10^{-5} Torr. This corresponds roughly to a pressure of 10^{-3} Torr in the gas cell [99]. This differential pumping is possible due to the small size of the two slits in the gas cell, each of which is 1 mm wide in the direction perpendicular to the laser propagation and 2 mm wide in the direction along the laser propagation.

These slits allow the electrons ionized along the laser polarization direction to "escape." As the interaction region is free of static fields, the electrons drift to the detectors with speeds depending on the energy they acquired in the ionization process. There are two distinct energy regions corresponding to the direct electrons and the backscattered electrons. Figure C.2 shows typical spectra for ionized electrons from xenon. The dominant feature appears at low energy — these are the direct electrons. The electrons at higher energy,

i.e. above about 20 eV, are the backscattered electrons. The electron production in both energy regimes depends on the CEP of the laser pulse, but the effect is more dramatic for the backscattered electrons. Thus, for monitoring the CEP, these are the electron energies of interest.

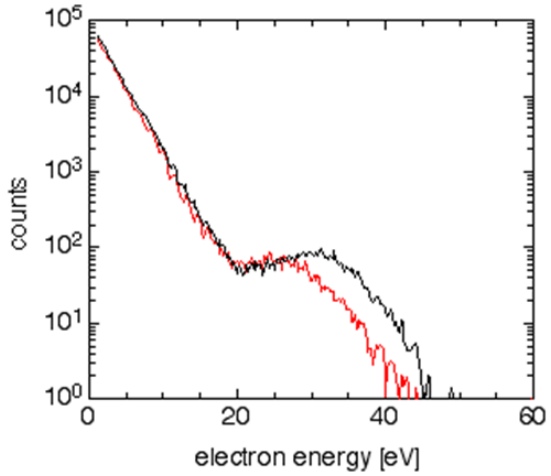

Figure C.2: Histogram of the electron energy from above threshold ionization of xenon. The direct electrons appear between 0 and about 20 eV, while the backscattered electrons are above about 20 eV. Adapted from [262].

As the rate of the direct electrons is orders of magnitude higher than the backscattered electrons, a two mesh design is used to deflect the low energy electrons. These meshes are mounted just in front of the detectors. The first (or top) mesh is grounded, such that the interaction region and drift regions are field free, and the second mesh has a small negative voltage (typically -27 V) applied to it in order to repel the direct electrons. The lifetime of the detector is increased by protecting it from the large rate of direct electrons.

The detectors consist of two particle-detection quality MCPs in a chevron configuration with a metal anode, purchased as an assembly from Photonis [259]. The diameter of the active MCP area is 25 mm, and the open area ratio is 55 %. The detectors are mounted on vacuum flanges with high vacuum feedthroughs for the voltage supply. A voltage of 2200 V is applied to the anode, 2116 V is applied to MCP back, and 433 V is applied to MCP front.

All voltages are supplied through a voltage divider, driven by a single power supply.

A thin sheet of μ-metal shields the electron path, from the interaction region to the detectors, from magnetic fields. Therefore, the trajectories of the electrons are not influenced by the earth or stray magnetic fields. A sketch of the parts and assembly of the phase meter is shown in Figs. C.3, C.4, and C.5.

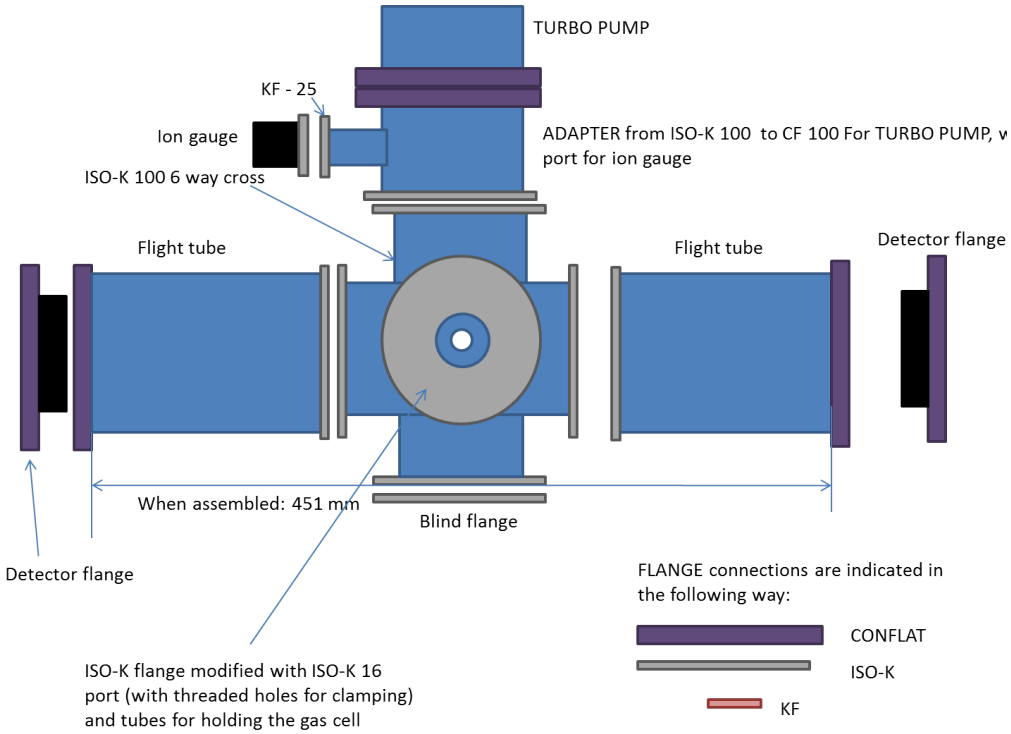

Figure C.3: Schematic top view of the phase meter apparatus.

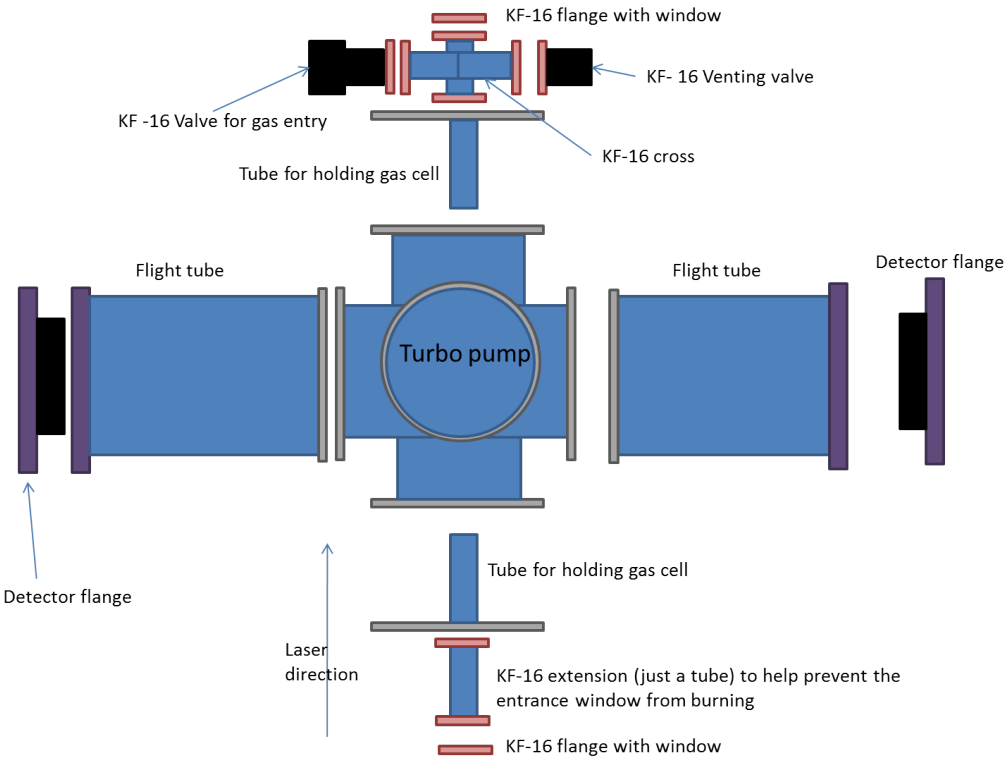

Figure C.4: Schematic side view of the phase meter apparatus.

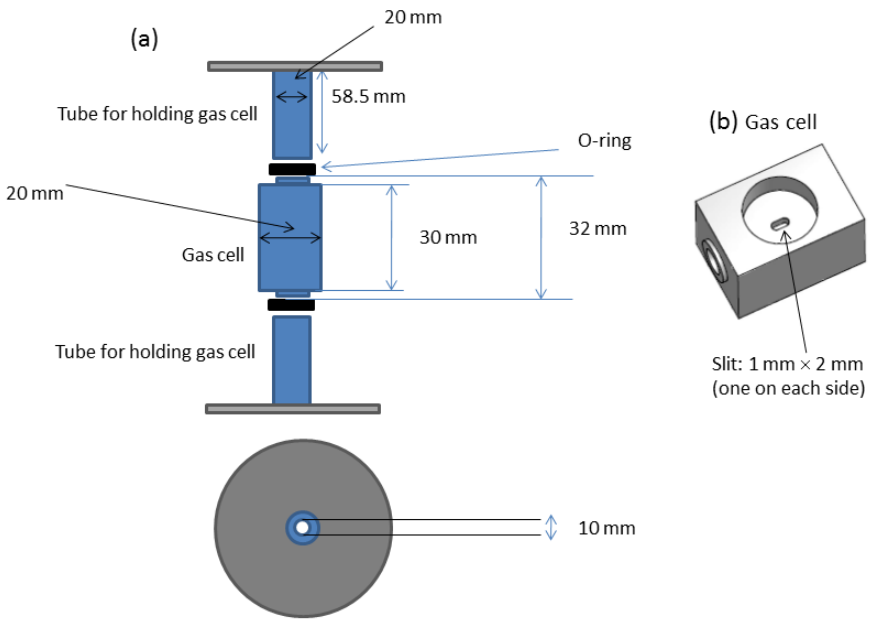

Figure C.5: (a) Schematic view of the gas cell assembly for the phase meter and (b) technical drawing of the gas cell.

C.2 Analysis

The electron time-of-flight signals for each detector are processed electronically, as outlined in Appendix A and Chapter 4. The resulting parametric asymmetry plot (PAP), shown for example in Fig. 4.3(b), must be further analyzed to retrieve the CEP. We use a code written in Matlab [263] for this purpose. The code does two things: (i) calculates a conversion from measured angle θ (see Fig. 4.3) to CEP angle ϕ based on a "reference" PAP, and (ii) applies the conversion to the phase-tagged data.

The best case scenario for a reference PAP is to measure every laser shot, as a purely random sample of the CEP is desired to properly convert θ to ϕ. The data acquisition system in JRML allows us to do this. However, post-processing of the reference PAP for every laser shot is quite time consuming. Therefore, we chose every 10th laser shot to be the reference PAP. This provided a large enough sample to preserve its random nature. Comparison of both cases led to no noticeable differences in the outcome (such as in an asymmetry map or a yield map).

At MPQ/LMU, the data-taking software would crash as it could not handle the large amount of information. To circumvent this problem, a coincidence logic box was incorporated into the electronics such that the data readout was limited to the case where both a photodiode signal and an MCP signal for the ion detector of the COLTRIMS was detected. To generate the reference PAP, the phase information that came with a background event (*i.e.* everything except the signal of interest) was used. The validity of this approach to generating a reference PAP was tested by plotting a histogram of the resulting ϕ distribution to make sure it was flat, as well as phase tagging different species within a measurement (such as Ar^+ and Ar^{2+} in the COLTRIMS measurement) and seeing phase shifts, if they are expected.

As mentioned above, the conversion from θ to ϕ relies on the assumption that the CEP distribution of the reference PAP is purely random. Figure 4.4(b) shows a histogram of θ. The θ distribution is not uniform due to several possible factors, including the difference

in detector efficiency, any geometrical differences between the two sides of the apparatus, the position of the time-of-flight gates, etc. Using a Matlab code, the distribution of θ is re-binned such that the number of counts in each new bin is the same. The resulting uniform distribution is ϕ, shown for example in Fig. 4.4(c).

Once the transformation from θ to ϕ is obtained from the reference PAP, it can be applied to any phase-tagged data within the same measurement. This refers to, for instance, the momentum along the laser polarization for Ar^{2+} in the COLTRIMS measurement [99].

There are a few tests that can be carried out to check that an observed CEP effect is not an artifact. The most convincing test is to offset the asymmetry parameters from the phase meter by one (or more) pulses compared to the data. Any CEP effect should disappear when the data is tagged with the "wrong" laser pulse, thus eliminating the CEP correlation between the two measurements. If an effect persists, it is likely an artifact, and further checks should be carried out to verify that this is the case. One should be especially suspicious if the oscillations with CEP follow any oscillations observed in the ϕ histogram. Oscillations in the ϕ histogram can occur when, for example, the phase signal saturates during the experiment (see arrows in Fig. C.6), and cutting out the saturated signal biases the conversion. While an asymmetry parameter for the phase tagged data is more robust against this kind of artifact, an artifact arising in the CEP dependence of the yield can be caused by the saturation. Note that the level of saturation in the PAP must be kept below about 0.1% (number of saturated counts compared to the number of good counts). The only way to avoid such artifacts completely is to have no saturation of the asymmetry parameters from the phase meter.

If the laser pulse is slightly drifting in intensity or bandwidth throughout the duration of the experiment, this can be accounted for, to good extent, by breaking the data into several time "steps". Here, both the reference PAP and the phase-tagged data are split into equal sections. This requires that the rate of detection for the phase-tagged data was stable throughout the run. For each step, the reference PAP is used to calculate the conversion from

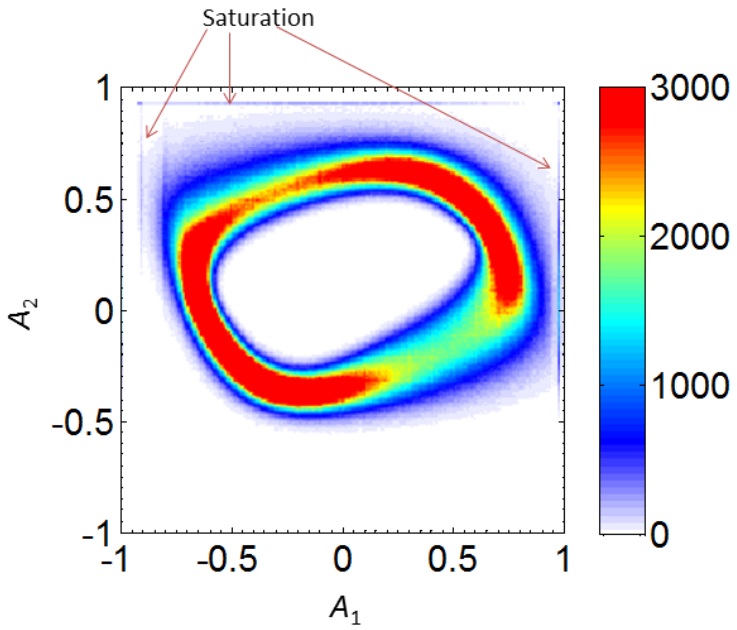

Figure C.6: Parametric asymmetry plot that has a small amount of saturation, indicated by the arrows.

θ to ϕ and then the individual reference PAP is used for each phase-tagged data segment corresponding to the same time step. Taking this idea further, as is the premise of Ref. [198], the phase offset for each time step can be corrected for. Not accounting for the phase drift can lead to misleading results, especially for measurements on the CEP dependence of the total yield. In practice, one can measure the asymmetry of a CEP-dependent species in the experiment, such as Ar^+ in the Ar^{2+} experiment. An example of the evolution of the Ar^+ asymmetry is shown in Fig. C.7(b). The phase offset slowly drifts over the course of the measurement. For each time step, the phase offset can be determined by fitting a sinusoidal curve to the asymmetry (see Fig. C.7(a)) and recording the relative ϕ from the first time step. Storing this as a list, each phase offset can be added to the asymmetry evaluation of the species of interest.

This phase correction procedure can be quite easily carried out for the COLTRIMS experiments where there tend to be multiple species measured simultaneously. However, it

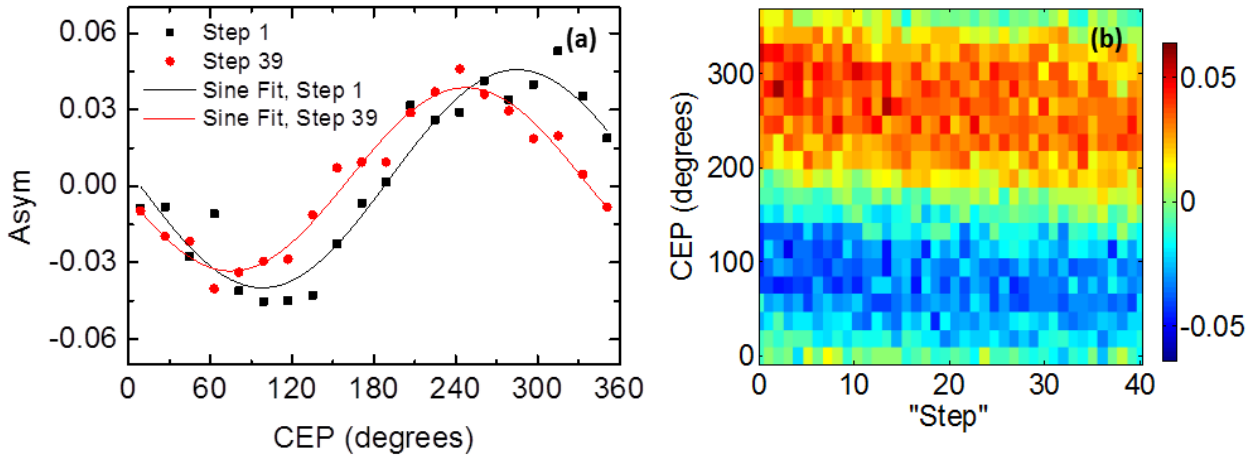

Figure C.7: Evolution of the phase offset over the course of an experiment with an acquisition time of several hours. (a) Asymmetry as a function of CEP for Ar^+ using 5 fs laser pulses for steps 1 and 39 and their sinusoidal fits. Note the approximately 30° shift between the two curves. (b) Asymmetry as a function of CEP for each time step, with a total of 40 steps. Note that the phase offset drifts slightly over the course of the several hours long experiment. The CEP was binned by 18°.

is less readily available for the LIMDI experiments. One approach is to split the laser beam into three arms, one for the phase meter, one for the LIMDI experiment, and one for a TOF apparatus measuring singly ionized argon from a cold target. We know that in the NSDI regime, for instance, that the Ar^+ can have asymmetry amplitudes on the order of 5 – 15%. The ability to measure Ar^+ with high statistics makes it a suitable choice for monitoring drifts in the CEP offset.

On a practical note, the Matlab code used to analyze the phase-tagged H_2^+ dissociation experiment is located at `J:\Phasemeter\PhaseTaggedAnalysis\` on the JRML network. The code, developed by Matthias Kübel, was modified for phase tagging the kinetic energy release for the dissociation events of an H_2^+ target. The main file "PhaseTagged.m" calculates the conversion from θ to ϕ from the reference PAP and applies it to the desired variable to be tagged. To plot the asymmetry map, the code titled "AsymMap.m" was used.